



Petrogenetic links between rare metal-bearing pegmatites and TTG gneisses in the West African Craton: The Mangodara district of SW Burkina Faso

Wilédio Marc-Emile Bonzi, Olivier Vanderhaeghe, Marieke van Lichtervelde, Urbain Wenmenga, Anne-Sylvie André-Mayer, Stefano Salvi, Marc Poujol

► To cite this version:

Wilédio Marc-Emile Bonzi, Olivier Vanderhaeghe, Marieke van Lichtervelde, Urbain Wenmenga, Anne-Sylvie André-Mayer, et al.. Petrogenetic links between rare metal-bearing pegmatites and TTG gneisses in the West African Craton: The Mangodara district of SW Burkina Faso. *Precambrian Research*, 2021, 364, pp.106359. 10.1016/j.precamres.2021.106359 . insu-03324812

HAL Id: insu-03324812

<https://insu.hal.science/insu-03324812>

Submitted on 6 Oct 2021

HAL is a multi-disciplinary open access archive for the deposit and dissemination of scientific research documents, whether they are published or not. The documents may come from teaching and research institutions in France or abroad, or from public or private research centers.

L'archive ouverte pluridisciplinaire **HAL**, est destinée au dépôt et à la diffusion de documents scientifiques de niveau recherche, publiés ou non, émanant des établissements d'enseignement et de recherche français ou étrangers, des laboratoires publics ou privés.

1 **Petrogenetic links between rare metal-bearing pegmatites and TTG gneisses in the West African**
2 **Craton: the Mangodara district of SW Burkina Faso**

3 Authors

4 *Wilédio Marc-Emile Bonzi^{1,2}, Olivier Vanderhaeghe², Marieke Van Lichtervelde², Urbain
5 Wenmenga¹, Anne-Sylvie André-Mayer³, Stefano Salvi², and Marc Poujol⁴

6

7 ¹ Département des Sciences de la Terre, Université Joseph Ki-Zerbo, 03 BP 7021 Ouagadougou,
8 Burkina Faso

9 ² Laboratoire Géosciences Environnement Toulouse, CNRS-IRD, Université Toulouse 3 Paul Sabatier,
10 14 Avenue Edouard-Belin, 31400 Toulouse, France

11 ³ Laboratoire GeoRessources, Université de Lorraine, CNRS, F-54000, Nancy, France

12 ⁴ Geosciences Rennes - UMR 6118, Université de Rennes, CNRS, F-35000, Rennes, France

13

14 *Corresponding author: bonzime@gmail.com

15

16 **Abstract**

17 We describe the geological context of rare metal-bearing pegmatites from the Mangodara district
18 (South-West Burkina Faso, Paleoproterozoic West African Craton) and discuss their petrogenesis and
19 links with the host rocks. The Mangodara district exposes a gneiss-granitoid complex structured in a
20 regional-scale dome, mantled by granodioritic gneiss enclosing rafts of amphibolite, micaschist and
21 paragneiss, and cored by tonalitic to trondhjemitic gneisses. These gneisses enclose granitoid plutons,
22 and four populations of rare metal-bearing pegmatites: titanite-allanite-, apatite-zircon-, garnet-
23 columbite (Li, Nb) and garnet-REE (Ti, Y, HREE)-bearing varieties.

24 Rafts of migmatitic amphibolite, micaschist and paragneiss are chemically equivalent to nearby
25 Birimian greenstone belts. An origin of the gneiss-granitoid complex by partial melting is suggested
26 by diffuse contacts of rafts with the gneisses as well as the presence of garnet-bearing or hornblende-
27 bearing leucosome in paragneiss and in amphibolites, respectively. Textural continuity between
28 pegmatites and granitic veins concordant to the foliation of the gneisses point to syntectonic
29 segregation of the pegmatite-forming magmas.

30 The compositions of gneisses and plutonic rocks spread between a Na-rich pole and a K-rich pole.
31 Granodioritic gneiss, hornblende-biotite granodiorite and potassic biotite granitoids define a K-rich
32 series attributed to relatively low-pressure high-degree partial melting of dominantly paragneiss,
33 which accounts for low to absent LILE and HFSE fractionation compared to the paragneiss. Tonalitic-
34 trondhjemite gneiss, a trondhjemite and a peraluminous two-mica tonalite belong to a Na-rich series
35 characterized by low K content and strong depletion in REE and HFSE, which might reflect
36 plagioclase clustering after partial melting at a relatively high pressure of amphibolite, and
37 fractionation of HFSE-REE-bearing minerals.

38 U-Pb dating of zircon from a titanite-allanite-bearing pegmatite at 2094.3 ± 8.8 Ma and of apatite from
39 tonalitic-trondhjemite gneiss, apatite-zircon-bearing pegmatite and granodioritic gneiss at 2094 ± 21
40 Ma, 2055 ± 20 Ma, and 2041 ± 33 Ma respectively, confirm that partial melting, melt segregation and
41 crystallization-cooling occurred during the Eburnean orogeny.

42 Based on these data, we propose that (i) titanite-allanite- and apatite-zircon-bearing pegmatites result
43 from syntectonic segregation of residual melt during crystallization of the tonalitic-trondhjemitic
44 gneiss, (ii) garnet-columbite-bearing pegmatites originate from syntectonic melt segregation from the
45 migmatitic paragneiss, and (iii) garnet-REE-bearing pegmatites derive from segregation of a residual
46 melt within the granodioritic gneiss.

47 **Keywords:** Rare metal-bearing pegmatite, TTG gneiss, Eburnean orogeny, West Africa Craton,
48 partial melting, melt segregation.

50 **1. Introduction**

51 This paper presents the geological context of the rare metal-bearing pegmatites exposed in the
52 Mangodara district (South west Burkina Faso, West African Craton, Fig. 1), in the Baoulé-Mossi
53 domain of the Eburnean orogenic belt (Baratoux et al., 2011 and references therein). Its goal is to
54 discuss the petrogenesis of these pegmatites and their potential links with their host rocks. The
55 formation of rare metal pegmatites requires a high degree of differentiation, which has classically been
56 related either to segregation of a silicate melt issued from low-degrees of partial melting of an
57 enriched source (Müller et al., 2017; Roda-Robles et al., 2007; Shaw et al., 2016) or from extreme
58 fractional crystallization of a fertile magma (Černý, 1991a, 1991b; Černý and Ercit, 2005; London,
59 2008; Martin and De Vito, 2005). In the Paleoproterozoic portion of the West African Craton (Fig. 1)
60 known for its huge gold reserves (Masurel et al., 2021), rare metal-bearing pegmatites mineralized in
61 spodumene and columbite-tantalite ($Ta > Nb$) are reported at Akim-Oda, Egyaa and Winneba in
62 Ghana (Adams, 2013; Anum et al., 2015; Chalokwu et al., 1997; Nude et al., 2011), at Issia in Ivory
63 Coast (Allou, 2005) and Saraya in eastern Senegal (Goujou et al., 2010; Ndiaye et al., 1997). These
64 pegmatites form dykes intruding peraluminous granitic plutons and metasedimentary units, and are
65 interpreted to derive from the differentiation of these sedimentary-derived granitic bodies. The
66 Mangodara district (Fig. 2) potentially represents a deeper section of the Birimian crust, with
67 pegmatites hosted in a gneiss-granitoid complex that includes large rafts of migmatitic amphibolites
68 and paragneiss, all structured into a regional-scale dome. In such context, deciphering the relationships
69 of the pegmatites with their gneissic host rocks is essential in order to assess their petrogenesis. Early
70 investigators considered these gneiss-granitoid complexes to represent the Archean basement of
71 Paleoproterozoic Birimian greenstones, essentially based on their positioning at the lowest exposed
72 structural level (Arnould, 1961; Ducellier, 1963; Hottin and Ouedraogo, 1975; Tagini, 1971).
73 However, U-Pb geochronology on zircon from granitoid and gneisses from these complexes did not
74 yield any Archean age, but ranges from 2300 to 2050 Ma (Anum et al., 2015; Castaing et al., 2003; De
75 Kock et al., 2011; Doumbia et al., 1998; Gasquet et al., 2003; Grenholm et al., 2019a; Hirde et al.,
76 1996; Ilboudo et al., 2021; Parra-Avila et al., 2017; Petersson et al., 2016; Sakyi et al., 2014; Soumaila

77 et al., 2008; Tapsoba et al., 2013; Tshibubudze et al., 2015, 2013; Wane et al., 2018). These ages span
78 the entire Birimian cycle, from the Eoeburnean or Pre-Eburnean phase (2260–2150 Ma) to the
79 Eburnean orogeny (2150–2050 Ma), which is constrained by U-Pb in zircon from Birimian
80 metavolcanites and plutonic rocks intrusive in greenstone belts across the Baoule-Mossi domain
81 (Grenholm et al., 2019a; Lambert-Smith et al., 2016; Parra-Avila et al., 2017 and references therein).

82 The absence of Archean ages, together with the presence of Early Proterozoic ages up to 2300 Ma,
83 served to invoke a pre-Birimian crustal growth event, referred to as Burkinian or Dabakalian, forming
84 the Birimian volcanic and sedimentary basement, or at least the basement of its upper series (Lemoine,
85 1988; Lemoine et al., 1990; Vidal et al., 1996).

86 In this context, gneisses and granitoids exposed in the Eburnean orogenic belt have been interpreted as
87 syntectonic to late tectonic plutons, mainly based on their pervasive ductile fabric consistent with
88 structures observed in the surrounding greenstones (Gasquet et al., 2003; Hirdes et al., 1996; Vidal et
89 al., 2009). Moreover, gneiss-granitoids and Birimian greenstones share a similar Paleoproterozoic
90 juvenile isotopic signature, which was attributed to a common mantle source for these magmas
91 emplaced at different structural levels (Abouchami et al., 1990; Boher et al., 1992; Doumbia et al.,
92 1998; Gasquet et al., 2003; Pawlig et al., 2006; Sakyi et al., 2020; Tapsoba et al., 2013). However,
93 these structural features and the similarity in isotopic are equally consistent with an origin of gneiss
94 and granitoids by partial melting of the Birimian series (Doumbia et al., 1998).

95 In order to contribute to this debate, in this paper, we present new field observations, petrological-
96 microstructural and geochemical data from gneisses, plutonic rocks and swarms of rare metal-bearing
97 pegmatites of the Mangodara district. Based on these data, which highlight the significance of
98 metamorphic and magmatic units that compose the Mangodara district, we propose a petrogenetic
99 model relating the rare metal-bearing pegmatites to the gneiss-granitoids.

100

101 **2. Methodology**

102 Field work was conducted throughout the Mangodara district to document the mineralogy, texture, and
103 structure of each lithological facies and their mutual structural relationships. Regional directions of
104 lithofabrics were inferred from field measurement, from distribution and morphology of outcrops in
105 aerial photography (Google Earth), and from lineaments and other structures detected from
106 LANDSAT-8 and Sentinel-2 imagery. Shear zones were remotely identified by interpretation of
107 magnetic lineaments in aeromagnetic data (acquired during the SYSMIN project System for Mineral
108 production, 1998–1999, see Metelka et al., 2011), using the methodology proposed by Chardon et al.,
109 (2020).

110 Pegmatites and surrounding rocks of the Mangodara district were sampled for thin section preparation
111 and for whole-rock analysis. The latter were performed by the Service d'Analyses des Roches et des
112 Minéraux (SARM, Centre de Recherches Pétrographiques et Géochimiques de Nancy, France) using
113 inductively coupled plasma optical emission spectrometry (ICP-OES) with a Thermo Fischer
114 iCap6500 for major elements and inductively coupled plasma mass spectrometry (ICP-MS) with a
115 Thermo iCapQ for trace elements, and in Central Analytical facilities of University of Stellenbosch
116 (South Africa) using XRF spectrometry with a PANalytical Axios Wavelength Dispersive
117 spectrometer for major elements and using laser ablation inductively coupled plasma mass
118 spectrometry (LA-ICP-MS) with a Agilent 7700 for trace elements. Concentrations in major elements
119 of minerals were measured using a Cameca SXFive at Center Raimond Castaing (Toulouse, France).
120 Standards were albite (Na), wollastonite (Si, Ca), Al₂O₃ (Al), sanidine (K), MnTiO₃ (Mn, Ti), Fe₂O₃
121 (Fe), topaz (F), MgO (Mg), tugtupite (Cl), Cr₂O₃. Detection limits for major element oxides were
122 under 0.2 wt%. The structural formula of hornblende was calculated based on 23 oxygen atoms. Fe²⁺
123 and Fe³⁺ were estimated by charge balance, and the formula was normalized with the minimum ferric
124 amount allowing complete site occupancy, using the method of Schumacher (1997).

125 Pressure-temperature pseudosections were calculated for a paragneiss and an amphibolite samples
126 using Theriaik/Domino v 11/03/2020 (de Capitani and Brown, 1987; de Capitani and Petrakakis,
127 2010), with the internally consistent thermodynamic dataset of Holland and Powell (1998), in its

128 version 5.5 updated in November 2003. Bulk composition of the paragneiss and the amphibolite are
129 estimated respectively from the whole rock composition of the samples BMS114B and BMN109.
130 Calculations are done in the chemical system Na₂O-CaO-K₂O-FeO-MgO-Al₂O₃-SiO₂-H₂O-TiO₂-O
131 (NCKFMASHTO) for the paragneiss, and Na₂O-CaO-FeO-MgO-Al₂O₃-SiO₂-H₂O-TiO₂-O
132 (NCFMASHTO) for the amphibolite. Manganese content was ignored from calculation because of its
133 low concentration in the two samples (< 0.1 mol%), but this should not significantly affect the
134 equilibrium phase transitions. Hydrogen content is adjusted to reach a minimum of H₂O saturation at
135 solidus at 7 kbar. A supplementary tiny content of O is added to stoichiometric O content, to permit
136 stability of Fe³⁺-bearing phase. The used activity-composition models are biotite, garnet, ilmenite-
137 hematite, spinel and silicate melt (White et al., 2007), cordierite, staurolite and chlorite (Holland and
138 Powell, 1998), white mica (muscovite, Fe-celadonite), (Coggon and Holland, 2002), clinopyroxene
139 (Green et al., 2007), orthopyroxene (White et al., 2002), amphibole (Diener et al., 2007) and feldspars
140 (Baldwin et al., 2005; Holland and Powell, 2003). Andalusite, kyanite, sillimanite, quartz and H₂O are
141 treated as pure phases.

142 Zircon and apatite were dated by in situ laser ablation on polished thin section. Prior selection of
143 targets and imaging of minerals were carried out by back-scattered electron imaging with a scanning
144 electron microscope (SEM) Jeol JSM 6360LV (GET, Toulouse, France) and by cathodoluminescence
145 imaging with the TESCAN Vega 3 (GeoRessources, Nancy, France). Laser ablation was operated
146 using a quadripole Agilent 7700 coupled with an ESI NWR193UC excimer laser (Géosciences
147 Rennes, Rennes, France). U-Pb ages are calculated from isotopic data with the software Isoplot/Ex
148 v3.76 (Ludwig, 2003). Technical details of the analysis are supplied in appendix.

149

150 **3. Geological context of the Mangodara district within the West African Craton**

151 The West African Craton (WAC) consists of the Kenema-Man Archean nucleus surrounded along its
152 northern and eastern borders by the Baoule-Mossi domain composed of Paleoproterozoic terranes of
153 the Birimian series tectonically accreted during the multicyclic Eburnean orogeny (Baratoux et al.,

154 2011; Block et al., 2016b, 2016a; Feybesse et al., 2006; Kouamelan, 1996; Perrouty et al., 2012;
155 Tshibubudze and Hein, 2013; Vidal and Alric, 1994). The Baoule-Mossi domain corresponds to a
156 succession of greenstone belts of the Birimian series juxtaposed along strike-slip shear zones to
157 gneiss-granitoids coring large dome structures (Baratoux et al., 2011; Fabre et al., 1990; Metelka et al.,
158 2011; Milési, 1989; Vidal et al., 2009). It is a lateral equivalent to the Transamazonian belt in the
159 South America (Caen-Vachette, 1988; Chardon et al., 2020; Delor et al., 2003; Grenholm, 2019;
160 Grenholm et al., 2019a; Ledru et al., 1991; Tassinari and Macambira, 1999; Vanderhaeghe et al.,
161 1998)

162 The Mangodara district (SW Burkina Faso) is situated in the Sidéradougou gneiss-granitoid complex
163 (SGGC) of the Baoule-Mossi domain, between the Banfora greenstone belt to the west, and the
164 Houndé greenstone belt to the east delimited by the sinistral Ouango-Fitini shear zone (OFSZ) (Fig.
165 1). The Birimian in south-west Burkina Faso is composed of series of metamorphosed and deformed
166 subvertical interlayered tholeiitic to calc-alkaline basalts, andesites and rhyolites, alternating with
167 volcanic-sedimentary rocks and silicic sedimentary rocks. In this region, U-Pb dating on zircon from
168 rocks of the Birimian series indicate an early volcanic activity from 2220 Ma to 2160 Ma (Baratoux et
169 al., 2011; Giovenazzo et al., 2018; Hirades et al., 1996; Hirades and Davis, 1998; Lüdtke et al., 1998)
170 and later emplacement/deposition of volcanic-sedimentary series from 2165 to 2080 Ma (Castaing et
171 al., 2003; Grenholm et al., 2019b; Hirades et al., 1996; Lüdtke et al., 1998).

172 Aside from volcanic rocks of the Birimian series, plutonic rocks, with compositions ranging from
173 intermediate to felsic, are intrusive in the greenstone belts of Banfora, Houndé and Boromo. They also
174 constitute the gneiss-granitoids of the Sideradougou, Diebougou, and Koudougou-Tumu complexes
175 (Fig. 1). Ages of these plutons can be separated in four periods, with two peaks designated as
176 Magmatic Event 1 (ME1) and 2 (ME2), coeval with major deformation phases (Baratoux et al., 2011;
177 Grenholm et al., 2019a; Hirades et al., 1996; Parra-Avila et al., 2017). Pre-ME1 magmatism is
178 represented in SGGC by a poorly constrained U-Pb zircon age of 2243 ± 30 Ma in a hornblende and
179 biotite gneiss in the north of the SGGC (Giovenazzo et al., 2018) and of 2312 ± 17 Ma on an inherited
180 core from the Dabakala tonalite, south of the SGGC (Gasquet et al., 2003). The first magmatic peak

181 (ME1) is represented by layered tonalite, trondhjemite and granodiorite dated between 2160 and 2130
182 Ma. South of the studied area, ME1 plutons in Ivory Coast, correspond to “Comoé type” granodioritic
183 biotite gneiss dated by U-Pb on zircon at 2152 ± 3 Ma, and to the “Bavé type” granitoid intrusion
184 dated at $2137 +9/-7$ Ma (U-Pb dating with Thermal Ionization Mass Spectrometry by zircon
185 dissolution, Hirdes et al., 1996). The second magmatic peak (ME2) is characterized by granodiorite
186 and amphibole-biotite granite forming plutons emplaced between 2120 Ma and 2100 Ma. The ME2
187 period is also characterized by emplacement of volcanic rocks (basalt, andesite, dacite, rhyolite,
188 épiclastite) defined as the Bandamian cycle only described to the west of the OFSZ (Fig. 1) and dated
189 between 2120 and 2080 Ma (Gasquet et al., 2003; Grenholm et al., 2019b; Hirdes et al., 1996;
190 Mériaud et al., 2020). The post-ME2 magmatic period is represented by undeformed plutons of
191 potassic and biotite granites that crystallized between 2110 Ma and 2070 Ma (Baratoux et al., 2011;
192 Metelka et al., 2011; Parra-Avila et al., 2017, 2019).

193 Magmatic rocks of the ME1 and ME2 periods are characterized by a ductile fabric in continuity with
194 the one of the Birimian series and the gneiss-granitoids, which have been variously interpreted. Some
195 authors emphasize the impact of far-field forces derived from plate tectonics and either invoke the
196 succession of D1 and D2 deformation phases reflecting early tangential tectonics followed by strike-
197 slip dominated transpression (Baratoux et al., 2011; Metelka et al., 2011) or a progressive lateral flow
198 of a weak lithosphere (Chardon et al., 2020). Others highlight the role of buoyancy forces and propose
199 that the shallow-to moderately dipping foliation of the gneiss-granitoids records diapiric ascent of the
200 TTG massifs in the Birimian series (Lombo, 2009, 2010; Vidal et al., 2009).

201 The Birimian series is affected by sub-greenschist to amphibolite facies metamorphic grade (Doumbia
202 et al., 1998; Feybesse et al., 2006; Liégeois et al., 1991; Vidal and Alric, 1994). Metamorphic
203 isogrades depict a greenschist to amphibolite facies metamorphic gradient that defines a contact
204 aureole around granitoids plutons (Debat et al., 2003; Fontaine et al., 2017; Gueye et al., 2008; Pons et
205 al., 1995) and delineates regional-scale domes cored by gneiss-granitoids (Block et al., 2015, 2016b;
206 Vidal et al., 2009).

207

208 **4. Results**

209 **4.1. Geology of the Mangodara district**

210 **4.1.1. Regional structure**

211 The Mangodara district is characterized by a dome structure mantled by granodioritic gneiss that
212 contains a variety of rafts and enclaves of amphibolite, micaschist and paragneiss ranging in size from
213 the kilometer to the centimeter, and cored by tonalitic-trondhjemitic gneiss (Fig. 2). The contact
214 between the granodioritic and tonalitic-trondhjemitic gneiss is marked by a crescent-shaped layer of
215 two-mica tonalite along the southern boundary of the dome and by discontinuous lenses of
216 trondhjemite along its north-eastern margin (station BMN33, Fig. 2). To the east and south of the
217 dome, the granodioritic gneiss is intruded by monzogranitic to granitic plutons that we designate as
218 Ganso-Gountiedougou granitoids (GG-granitoids), and by hornblende granodiorite, respectively.
219 Amphibolite, micaschist and paragneiss rafts, as well as gneisses and granitoids contain pegmatites
220 that are concordant to discordant relative to the structure of their hosts.

221 The preferred orientation of the rafts is parallel to the main foliation of the granodioritic gneiss and of
222 the hornblende-biotite granodiorite. This foliation is marked by the preferred orientation of biotite,
223 hornblende and mica-rich enclaves, but also by alternations of layers with different proportions of
224 biotite, hornblende, quartz and feldspar. At the scale of the Mangodara district, foliation trajectories
225 are roughly concentric and delineate the dome structure. In the granodioritic gneiss, foliation planes
226 display a moderate to steep dips (between 20° and 60°) away from the core of the dome. Stretching
227 and mineral lineation in the granodioritic gneiss have been identified only in the north-east of the
228 district and are dominantly down dip. The foliation of the tonalitic-trondhjemitic core is typically
229 concordant to the contact with the granodioritic gneiss but this contact is slightly discordant relative to
230 the fabric of the mantling units. Within the tonalitic-trondhjemitic core, foliations planes also define
231 two second order domes.

232 Magnetic lineaments (Chardon et al., 2020; Metelka et al., 2011) suggest the presence of shear zones
233 flanking the northern and southern margins of the tonalitic-trondhjemite core of the Mangodara dome.
234 The asymmetric shape of the tonalitic-trondhjemite core of the dome is consistent with an apparent
235 anticlockwise rotation associated with a dextral sense of shear. These shear zones might connect to the
236 Ouango Fitini Shear Zone (OFSZ, Chardon et al., 2020), which is interpreted as a D2 structure
237 (Baratoux et al., 2011; Hirdes et al., 1996; Metelka et al., 2011). The northern shear zone has not been
238 identified in the field but the southern one is marked, near Massadeyirikoro, by a subvertical NE-SW
239 trending foliation in the paragneiss and in the hornblende-biotite granodiorite. A NW-SE-trending
240 shear zone, designated as the Gountiédougou shear zone, cross-cuts the Mangodara district along the
241 contact between the granodioritic gneiss and the GG-granitoids. This shear zone is marked by steep
242 mylonitic zones with thickness between 1 and 30 cm affecting the granodioritic gneiss and the eastern-
243 most pegmatites. These subvertical shear zones are connected with dispersed thin subhorizontal ones
244 and are associated with retrogression of biotite and hornblende in chlorite and epidote. Doleritic and
245 microgranitic dykes with sharp contacts cross-cut the different lithological units, and are attributed to
246 post-Eburnean events.

247

248 **4.1.2. Mantling units**

249 Granodioritic gneiss, which dominates the mantling units of the Mangodara dome, is characterized by
250 a composition and texture that is heterogeneous at the meter and centimeter scales but can be
251 considered homogeneous at the kilometer scale (Fig. 3c to d). The average facies of the granodioritic
252 gneiss consists of a groundmass of intermingled subhedral biotite, hornblende, plagioclase and rare K-
253 feldspar with convoluted intergranular patches of anhedral quartz (Fig. 4). Locally, quartz and/or
254 feldspar films are coating phenocrysts (Fig. 4b). A layering is locally marked by alternating
255 centimeter-thick granitic veins with plagioclase phenocrysts (Fig. 3b) and hornblende-biotite-rich
256 layers with microgranular texture (Fig. 3c) as well as by the preferred orientation of biotite and
257 hornblende. Plagioclase and hornblende phenocrysts are surrounded by subhedral biotite and
258 hornblende (Fig. 4a and 4b). Euhedral titanite and allanite are common, the latter being partially
10

259 retrogressed to epidote, and subhedral apatite. Epidote occurs as subhedral to anhedral magmatic
260 crystals cored by allanite, as inclusion in plagioclase and amphibole, or as secondary minerals within
261 the groundmass surrounding micas and hornblende. Zircon is present as micro-inclusions in biotite,
262 surrounded by black aureoles typical of radiation damage. Apatite forms subhedral to euhedral crystals
263 (size < 200 µm) within plagioclase, quartz, and biotite. Opaque minerals (size < 500 µm) are
264 associated with biotite and hornblende aggregates. Rare microgranular mesocratic enclaves, composed
265 of hornblende, biotite, plagioclase and quartz, form ovoid meter-scale bodies reaching 10 cm in
266 thickness, elongated in foliation planes of the granodioritic gneiss. East of the dome, near
267 Gountiedougou, the granodioritic gneiss grades into granite collected in dilatant sites accommodated
268 by heterogeneous deformation (Fig. 3d). In this area, the contact with the granodioritic gneiss is
269 marked by leucocratic veins concordant to the foliation, which are locally folded (Fig. 3e).

270 Amphibolite and micaschist rafts are characterized at the outcrop scale by a composite foliation
271 attributed to transposition of a primary magmatic-sedimentary layering into a schistosity (S_n)
272 associated with rootless isoclinal folds, boudins and shear bands (Fig. 5a and b). Amphibolites consist
273 of hornblendite and hornblende gabbro. Hornblendite is fine-grained with poikilitic hornblende and
274 plagioclase that contain lobate quartz. Yellowish sub-circular epidote locally occurs as an alteration
275 product of hornblende. Hornblendite hosts networks of 1 to 10 cm thick veins dominantly composed
276 of plagioclase with some hornblende. These veins can be either concordant or discordant to the
277 foliation and are locally isoclinally folded. Their margins are characterized by accumulation of
278 hornblende crystals (Fig. 5c), which suggests segregation of a melt from the plagioclase-hornblende
279 matrix. Elongated enclaves of amphibolite, dispersed in the granodioritic gneiss, grade into layers with
280 a gabbroic to monzogabbroic composition made of plagioclase and hornblende, locally megacrystic
281 (euherdral, up to centimeter sized, in a medium-grained matrix). Micaschists include mafic schists
282 hosting porphyroblastic hornblende, biotite schist, muscovite-biotite schist, and sericite-schist (Fig. 5b,
283 5d). Micaschists are intruded by centimeter-thick concordant granitic dykelets and contain quartz
284 veins.

285 Paragneiss rafts are common south of the Mangodara dome and the largest one is pinched between the
286 two-mica tonalite and the hornblende-biotite granodiorite. They are characterized by alternations of 20
287 to 30 cm thick quartz-feldspar-rich and mica-rich layers interpreted as former beds of graywacke and
288 pelite (Fig. 6a and b) transposed in a composite foliation. The metamorphic mineral assemblage of
289 coarser mica-rich layers includes sillimanite as well as staurolite and garnet porphyroblasts, which are
290 symptomatic of amphibolite facies metamorphism (Fig. 6a, c and d). In addition to the inherited
291 transposed sedimentary bedding, the presence of quartz-feldspar veins including some biotite with a
292 coarse-grain texture devoid of any solid-state fabric and with diffuse contacts are indicative of
293 segregation of partial melts (Fig. 6b). A first schistosity, designated as S_n , is delineated by the
294 preferred orientation of sillimanite and biotite (Fig. 6a, c and d). It is affected by crenulation folds
295 associated with an axial planar schistosity S_{n+1} marked by euhedral biotite associated with sillimanite
296 and white mica. In zones of weak transposition, staurolite and garnet porphyroblasts are wrapped into
297 the S_n schistosity but contain inclusions that point to synkinematic crystallization. In particular,
298 inclusions in staurolite delineate an internal schistosity in continuity with the S_n schistosity of the
299 matrix. This internal schistosity is crenulated with an axial planar S_{n+1} , which is not in continuity with
300 the S_{n+1} schistosity of the matrix. This is consistent with an anticlockwise rotation of staurolite
301 porphyroblasts after the development of S_{n+1} (Fig. 6d). Staurolite-sillimanite-garnet paragneiss grades
302 into migmatitic paragneiss with leucosome veins preferentially developed in metapelitic layers.
303 Migmatitic paragneiss with more than 20 % of leucosome displays a continuous network of
304 concordant and discordant veins. Migmatitic paragneiss grades into the granodioritic gneiss by
305 alternations of mesocratic layers hosting garnet-columbite pegmatites, next to mica-rich and
306 leucosome-bearing layers (Fig. 7a to d). Alternations of leucosome veins with mesosome layers define
307 a synmigmatitic foliation, which is parallel to the S_{n+1} schistosity delineated by a sillimanite-biotite-
308 chlorite-staurolite-garnet assemblage (Fig. 7e). Garnet occurs as inclusion-rich porphyroblasts but also
309 as crystals devoid of inclusions within or along the boundaries of leucosome veins, suggesting garnet
310 growth during incongruent melting (Fig. 7e and f). Concordant leucosome veins are locally in textural
311 continuity with pegmatite dykes with diffuse contacts marked by biotite selvages.

312

313 **4.1.3. Core units**

314 The tonalitic-trondhjemite gneiss, dominating the core of the Mangodara dome, is significantly more
315 leucocratic than the granodioritic gneiss. It is characterized by a hypidiomorphic texture with abundant
316 oligoclase (up to 60%), quartz, rare microcline, biotite, and up to centimetric euhedral magnetite (Fig.
317 8a, Fig. 9). Green hornblende is rare, and appears as anhedral crystals associated with biotite.
318 Accessory minerals are allanite-epidote, titanite, and apatite. Quartz forms intergranular patches that
319 are locally affected by undulatory extinction and recrystallization into equant neoblasts. A foliation is
320 depicted by the preferred orientation of euhedral biotite and hornblende, locally forming thin layers.

321 The foliated tonalitic gneiss typically displays a network of texturally continuous hornblende tonalite
322 veins and pegmatite veins, which are concordant to discordant to the foliation and localized in zones
323 of heterogeneous deformation such as shear zones (Fig. 8b, c and d). This tonalitic gneiss locally
324 forms rafts in a leucotonalite with a homogeneous composition and magmatic texture (Fig. 8c).
325 Hornblende tonalite veins contain mafic clots with hexagonal, diamond- or square-shaped sections,
326 composed of a poikilitic assemblage of hornblende and biotite enclosing lobate quartz, which are
327 interpreted as pseudomorphs after hornblende (Fig. 8e).

328 The tonalitic-trondhjemite gneiss also contains a few layers of granodioritic gneiss, of epidotized
329 migmatitic amphibolite with folded concordant leucosome layers (up to 5cm wide) alternating with
330 biotite-rich layers and pegmatite veins (Fig. 3f).

331

332 **4.1.4. Plutonic rocks**

333 Plutonic rocks of the Mangodara dome are usually in diffuse contact with the host gneisses and mostly
334 concordant to the regional structure, but they locally show sharper intrusive contacts. They are
335 characterized by a magmatic fabric with a preferred orientation of euhedral minerals, only locally
336 slightly overprinted by solid-state deformation.

337 GG-granitoids exposed in the eastern part of the Mangodara dome, in gradual contact with the
338 granodioritic gneiss, have a composition varying between monzogranite and biotite granite with
339 megacrystic K-feldspar, quartz, plagioclase, biotite and hornblende (Fig. 10a, b and c). Their
340 magmatic fabric is also delineated by disseminated biotite aggregates. GG-granitoids contain
341 decimeter to meter-scale angular enclaves of gabbro, diorite, granodiorite and monzogranite with
342 sharp boundaries. In contrast, some enclaves of gabbro are clustered and aligned in diffuse and
343 mingled contact with the host granitoid (Fig. 10b). Rafts of granodioritic gneiss are abundant in the
344 GG-granitoids east of Gountiedougou. In this part of the district, the youngest magmatic rock is a
345 biotite porphyritic granite, intrusive in other GG-granitoid, mostly composed of megacrystic
346 orthoclase, quartz, plagioclase, biotite and hornblende (Fig. 10c). Commonly, GG-granitoids contain
347 titanite forming euhedral lozenges of up to 1 cm in size, and epidote anhedral or granular crystals,
348 locally showing a concentric zonation. Other accessory minerals are zoned allanite, zircon, and
349 opaques.

350 The trondhjemite lens along the north-eastern margin of the core of the Mangodara dome is composed
351 of plagioclase, biotite, rare quartz and magnetite. The preferred orientation of biotite delineates a
352 foliation and a network of anastomosed ductile shear zones. The trondhjemite hosts thin quartz-felspar
353 veins concordant to the foliation.

354 The hornblende-biotite granodiorite, forming a pluton within the granodioritic gneiss to the south of
355 the Mangodara dome close to the contact with the tonalitic-trondhjemitic core, is typified by
356 abundance of mica-rich enclaves (Fig. 10d). It is composed of plagioclase, quartz, hornblende, biotite,
357 magnetite, and accessory apatite and allanite-epidote. Locally, plagioclase is megacrystic and
358 concentrically zoned, reaching 3 cm in size. The centimeter to decimeter-scale mica-rich enclaves (<
359 5% of the rock volume) are ovoid to elongated and composed of aggregates of biotite and rare
360 hornblende. Some enclaves of hornblende-biotite granodiorite found in garnet-columbite pegmatite
361 contain a network of texturally continuous concordant and discordant granitic veins that are folded
362 with the foliation.

363 The two-mica tonalite that delineates the contact between the mantling and core units of the
364 Mangodara dome, is composed of quartz, plagioclase, minor K-felspar, biotite and muscovite. Rare
365 subhedral to anhedral K-feldspar crystals are encompassed in a matrix dominated by quartz featuring
366 evidence of high-T recrystallization (subgrains with irregular interpenetrating boundaries). Accessory
367 minerals are euhedral apatite, allanite with epidote corona, and subhedral to anhedral epidote
368 associated with biotite, and magnetite. The texture of the two-mica tonalite is globally fine-grained
369 and hypidiomorphic but a magmatic fabric is locally delineated by the preferred orientation of
370 decimeter-scale enclaves of tonalitic-trondhjemite gneiss (Fig. 10e) and the preferred orientation of
371 biotite-rich layers. The two-mica tonalite contains also rare feldspar-tourmaline pegmatites that form
372 decimeter-scale pockets or meter-wide veins with diffuse contacts.

373

374 **4.1.5. Pegmatites**

375 The gneisses and granitoids of the Mangodara district comprise swarms of pegmatite dykes that are
376 subdivided into (i) titanite-allanite-bearing pegmatite, (ii) apatite-zircon-bearing pegmatites, (iii)
377 garnet-columbite-bearing pegmatites, and (iv) garnet-REE-bearing pegmatites.

378 Titanite-allanite pegmatites form a network of patches and veins both concordant and discordant to the
379 fabric of the tonalitic-trondhjemite gneiss (Fig. 11a). Concordant titanite-allanite pegmatitic veins are
380 coarse-grained and display diffuse and progressive contacts. They are in textural continuity with
381 discordant dykes that are regularly distributed in dilatant sites. Titanite-allanite pegmatites are mainly
382 composed of oligoclase, quartz, rare K-feldspar, biotite and magnetite, an assemblage identical to that
383 of the host gneiss. The modal content of biotite is < 5%, and this mica occurs as isolated flakes or
384 clusters. Accessory minerals include apatite, titanite, ilmenite, allanite, epidote, and zircon.

385 Apatite-zircon pegmatites are less common, with only four dykes identified so far. They are hosted in
386 the granodioritic gneiss where they form veins that are never thicker than 1 meter, discordant to the
387 foliation of the granodioritic gneiss but having a diffuse contact with it. Some of these veins are folded
388 in the granodioritic gneiss. Mineralogically, the apatite-zircon pegmatites are similar to the titanite-

389 allanite variety, but they lack titanite and contain higher amounts of apatite (up to 5 wt% in some
390 dikes) and zircon (widespread as inclusions in biotite).

391 Garnet-columbite pegmatites (Li, Nb enriched) are found in amphibolite, paragneiss, granodioritic
392 gneiss, hornblende-biotite granodiorite, and two-mica tonalite. They form a swarm of veins and dykes
393 with a width that can reach 300 m, and are mostly discordant to the fabric of their hosts. They display
394 an aplitic to graphic texture with local megacrystic alkali feldspars, plagioclase, biotite, muscovite,
395 spessartine-almandine garnet, cleavelandite, magnetite, and accessory apatite, tourmaline intergrown
396 with quartz, monazite, xenotime, zircon and columbite-tantalite. Some pegmatite veins are in textural
397 continuity with concordant leucosome veins of migmatitic paragneiss but others are transposed, folded
398 or boudinaged with cuspatate shapes into the foliation of the paragneiss and granodioritic gneiss (Fig.
399 6a, Fig. 11c, d and e). Some of these deformed pegmatites are zoned, with a margin marked by
400 polycrystalline feldspar crystals with a stockscheider texture and a core dominated by centimetric
401 quartz crystals (Fig. 11d). Garnet-columbite pegmatite dykes contain blocky meter-scale enclaves of
402 paragneiss, micaschist, and hornblende-biotite granodiorite. South of Massadeyirikoro, garnet-
403 columbite pegmatite dykes cross-cut apatite-zircon pegmatite dykes (Fig. 11b). At the grain scale, the
404 boundary between the two pegmatite types is rather irregular and follows the shape of the bordering
405 crystals (Fig. 12), suggesting that a part of the apatite-zircon pegmatite (quartz-plagioclase-biotite
406 assemblage) has been replaced by a subsequent pulse of magma, which crystallized into a quartz-
407 feldspar-muscovite-garnet assemblage.

408 Garnet-REE pegmatites (enriched in Ti, Y and heavy rare earth elements, the latter abbreviated as
409 HREE) are restricted to the eastern side of the Mangodara district (more than thirty dykes over a
410 surface of about 10 km²). They are hosted in granodioritic gneiss (Fig. 11f and g) and GG-granitoids.
411 They are metric to plurimetric in size with an average strike of N160° and a dip that ranges from
412 horizontal to subvertical. They are characterized by the predominance of biotite over muscovite,
413 presence of Ti-oxide (ilmenite-pyrophanite), epidote, rare tourmaline, REE-rich metamict accessory
414 minerals (similar in composition with euxenite or aeschynite) and absence of phosphate minerals.
415 Some dykes of garnet-REE pegmatites, which contain epidote, rare micas and rare garnet, are exposed

416 in textural continuity with granitic veins concordant to the foliation of the granodioritic gneiss (Fig.
417 3e, Fig. 11f).

418

419 **4.2. Metamorphism**

420 Metamorphic rocks of the Mangodara district display a variety of mineral paragenesis indicative of
421 pervasive greenschist facies metamorphism, as illustrated by rafts of sericite-muscovite-biotite schist
422 in the northeast of the district, to amphibolite facies metamorphism marked by hornblendite and
423 paragneiss in the central part of the district (Fig. 13). Northeast of the dome, amphibolite and
424 micaschist contain porphyroblastic hornblende, indicating pervasive amphibolite facies was reached
425 with $T > 450\text{--}500\text{ }^{\circ}\text{C}$ (Liou et al., 1974; Maruyama et al., 1983; Moody et al., 1983). Furthermore, the
426 presence of tonalitic leucosome veins in these rocks suggests partial melting of amphibolites, which
427 requires a temperature of about $750\text{ }^{\circ}\text{C}$ under fluid-absent condition (Rapp et al., 1991; Rushmer,
428 1991; Wolf and Wyllie, 1994; Wyllie and Wolf, 1993) or $650\text{ }^{\circ}\text{C}$ in hydrated conditions (Green et al.,
429 2016; Palin et al., 2016). Paragneiss rafts in the central and southern parts of the studied area are
430 characterized by a quartz-feldspar-biotite-sillimanite-garnet±staurolite±muscovite±chlorite mineral
431 assemblage (Fig. 6c and d) that is also symptomatic of widespread amphibolite facies metamorphism.
432 The structural-textural position of these minerals indicates a first mineral paragenesis marked by an
433 association of fibrolitic sillimanite with biotite (S_n fabric). Garnet and staurolite, which form
434 porphyroblasts superimposed on the sillimanite-biotite schistosity, are attributed to a second mineral
435 paragenesis (transition to S_{n+1}). In migmatitic paragneiss, garnet-bearing leucosome veins are
436 concordant to a foliation delineated by the preferred orientation of interlayered sillimanite-biotite-
437 chlorite enclosing garnet and staurolite porphyroblasts, suggesting that melt segregation occurred in
438 the presence of these minerals.

439 The calculated pseudosection of a garnet-staurolite bearing paragneiss (Fig. 14a) is consistent with
440 phase equilibria models of metapelites. Staurolite is stable for $T < 670\text{ }^{\circ}\text{C}$ (Pattison and Spear, 2018;
441 Tinkham et al., 2001), about 10 to 50 $^{\circ}\text{C}$ below the solidus. Under a pressure of 7 kbar, staurolite can

442 be expected to be stable with anatetic melt through the disequilibrium reaction garnet = staurolite.
443 That proposition is consistent with synkinematic crystallization of the two minerals, as observed in
444 thin section (Fig. 6c and d). Supersolidus staurolite is consistent with a temperature of about 675–700
445 °C (García-Casco et al., 2003). Garnet porphyroblasts suggest a pressure above 4.5 kbar in paragneiss,
446 and above 5 kbar in leucosomes (Patiño Douce, 1999; Spear et al., 1999). Subsolidus stability of
447 sillimanite requires a $T > 550$ °C (Bohlen et al., 1983; Holdaway and Mukhopadhyay, 1993; Pattison,
448 1992; Whitney, 2002), and a $P < 7$ kbar. The absence of stable cordierite in paragneiss points to a $P >$
449 5kbar. These observations constrain the metamorphic assemblage of the paragneiss to near-solidus
450 conditions: 650–680 °C, 6–7 kbar. It is noticeable that for a temperature exceeding the biotite-
451 breakdown reaction (> 790 °C), the modelled mineral composition of the partially molten paragneiss is
452 close to the one of the granodioritic gneiss (Fig. 14c).

453 The calculated pseudosection of the amphibolite (Fig. 14b) is in agreement with sub-solidus
454 composition dominated by hornblende and plagioclase, except that clinopyroxene, which should be
455 present in minor content, is unseen in the rock sample. The modelled solidus occurs at higher
456 temperature than in paragneiss (700–750 °C). Partial melting of the amphibolite promotes the
457 breakdown of hornblende and the crystallization of orthopyroxene, whereas plagioclase fraction
458 remains constant.

459 Magmatic epidote is present in granodioritic gneiss, tonalitic-trondhjemite gneiss, hornblende-biotite
460 granodiorite with mica-rich enclaves and in GG-granitoids. Experiments of epidote saturation in felsic
461 to intermediate magma show that crystallization of magmatic epidote requires a P higher than 5 kbar
462 in presence of water (Schmidt and Poli, 2004; Schmidt and Thompson, 1996). This value defines a
463 minimum pressure for crystallisation in the epidote-bearing granitoids of the Mangodara district.

464 Aluminium-in-hornblende is a calibrated barometer valid for intrusive rocks, assuming hornblende in
465 equilibrium with alkali feldspar, plagioclase, biotite, iron titanium oxide and titanite (Hammarstrom
466 and Zen, 1986). The major composition of hornblende from granodioritic gneiss, hornblende and
467 biotite granodiorite with mica-rich enclaves, and hornblende tonalite veins in tonalitic-trondhjemite
468 gneiss ranges from magnesio-hastingsite to ferro-pargasite. Depth of crystallization of hornblende is
18

469 estimated using the various published parameters (Hollister et al., 1987; Johnson and Rutherford,
470 1989; Mutch et al., 2016; Schmidt, 1992; Thomas and Ernst, 1990). Averages of calculated pressure of
471 granodioritic gneiss and hornblende-biotite granodiorite are equivalent and are between 4.4 kbar and
472 6.6 kbar (*Table 3*). Calculated pressure in hornblende tonalite vein is slightly lower, between 4.0 kbar
473 and 6.1 kbar and provide a constraint on the pressure of melt crystallization. The low diffusion rate of
474 Al in hornblende under submagmatic conditions reduces the possibility of resetting of the Al-in-
475 hornblende barometer by metamorphism. So, the pressure inferred from hornblende of the
476 granodioritic and tonalitic-trondhjemitic gneisses is interpreted to reflect their depth of crystallization.
477 The prevalence of biotite and hornblende in gneisses and granitoids, and the absence of orthopyroxene
478 imply that the dehydration reactions marking the transition to granulite facies did not occur. The
479 reported presence of kyanite in greenstones in NE of the Mangodara district (Ilboudo et al., 2017b),
480 and the occurrence of sillimanite, garnet and staurolite in paragneiss, reflect a moderate P and high T
481 metamorphic gradient, close of the solidus of paragneiss. The metamorphism recorded in the
482 amphibolite, micaschist and the paragneiss rafts corresponds to a sillimanite MP-HT metamorphic
483 facies. This is consistent with burial of the Birimian series along a geothermal gradient between 20
484 °C/km and 40 °C/km, which corresponds to the average thermal gradient identified in the greenstone
485 belts of the Baoule-Mossi domain (Ganne et al., 2014).

486

487 **4.3. Geochronology**

488 **4.3.1. U-Pb dating on zircon**

489 Zircon dating was completed *in situ* on the sample BMN28 of titanite-allanite type pegmatite. Zircon
490 occurs in the pegmatite as subhedral to euhedral crystals with rectangular to prismatic shape, inferior
491 to 400 µm in length, dominantly hosted in biotite. Cathodoluminescence imaging of zircon reveals
492 large cores and a rim marked by oscillatory zoning (Fig. 15a). Irregular patches blurring the oscillatory
493 textures are attributed to metamictization, which may explain the discordant analyses.

494 All analyses (Table 1) scatter along a Concordia with an upper intercept at 2078 ± 37 Ma, and lower
495 intercept close to present day at 32 ± 27 Ma (Fig. 15b). Most of the concordant analyses are located in
496 zircon cores, but discordant data are located in both cores and rims (Fig. 15c). Zircon age was
497 calculated selecting concordant data and propagating decay constant errors, with uncertainties of 2σ
498 multiplied by the square root of the mean square weighted deviation (MSWD) at 95 % of confidence
499 level. The obtained age is 2094.3 ± 8.8 Ma (MSWD = 1.6). In absence of a significant disparity
500 between cores and rim, this age is considered to date the crystallization of the titanite-allanite
501 pegmatite.

502

503 **4.3.2. U-Pb dating on apatite**

504 U-Pb dating was completed on apatite from the granodioritic gneiss (BMN20B), the tonalitic-
505 trondhjemitic gneiss (BMN11), and the apatite-zircon pegmatite (BMN20).

506 Apatite in gneisses and apatite-zircon pegmatites occurs as subhedral to euhedral crystals hosted in
507 plagioclase, quartz, biotite and magnetite. Internal zoning of apatite crystals is unseen with SEM, but
508 is visible with cathodoluminescence imaging. Oscillatory to zoned cores are surrounded by
509 homogeneous rims (Fig. 16a, b and c). Average size of analyzed crystals is 200 μm in granodioritic
510 gneiss, 300 μm in tonalitic-trondhjemitic gneiss and 1 mm in apatite-zircon type pegmatite.

511 Obtained data (Table 2) were plotted on the Tera-Wasserburg diagram (Tera and Wasserburg, 1972)
512 and ages were calculated by determination of the Concordia intercept with 95 % of level confidence.
513 Apatite yields average ages of 2041 ± 33 Ma (MSWD = 3.1) for the granodioritic gneiss, 2094 ± 21
514 Ma (MSWD = 1.6) for the tonalitic-trondhjemitic gneiss, and 2055 ± 20 Ma (MSWD = 4.9) for
515 apatite-zircon type pegmatite.

516

517 **4.4. Whole-rock geochemistry**

518 Geochemical data of representative samples of the different lithological facies exposed in the
519 Mangodara district are reported in Table 4. They are subdivided in (i) amphibolite and micaschist, (ii)
520 paragneiss, (iii) gneisses and plutonic rocks comprising granodioritic gneiss, microgranular mesocratic
521 enclave in granodioritic gneiss, tonalitic-trondhjemite gneiss, trondhjemite, hornblende-biotite
522 granodiorite, two-mica tonalite, biotite porphyritic granite (GG-granitoid), biotite monzogranite (GG-
523 granitoid) and monzogabbro.

524

525 **4.4.1. Amphibolites and micaschists**

526 Samples of amphibolite and micaschist are characterized by a low K content (0.25–0.49 wt% K_2O), a
527 relative depletion in large-ion lithophile elements (LILE) like Cs, Rb and Ba, and a minor
528 fractionation of light rare earth elements (LREE) vs HREE ($La_N/Yb_N = 4.6\text{--}8.1$). Enrichment in LREE
529 relative to HREE, and negative Nb and Ti anomalies are characteristic of tholeiitic to calc-alkaline
530 basalts and andesites such as the ones exposed in the Houndé and Banfora greenstone belts (Fig. 17a)
531 (Baratoux et al., 2011; Ilboudo et al., 2020), but also in many areas of the Baoule-Mossi domain
532 (Béziat et al., 2000; Ilboudo et al., 2017a; Lompo, 2009; Lüdtke et al., 1998; Pouclet et al., 1996).
533 Amphibolite has low Si ($52.3 \text{ wt\%} < SiO_2 < 54.1 \text{ wt\%}$), high Ca ($9.63 \text{ wt\%} < CaO < 10.15 \text{ wt\%}$) and
534 high ferromagnesian content ($Fe_2O_3 = 9.15\text{--}11.11 \text{ wt\%}$, $Mg\# = 0.55\text{--}0.57$, $Fe_2O_3+MgO+MnO+TiO_2 =$
535 $11.6\text{--}19.5 \text{ wt\%}$). Transition metals are elevated in amphibolite, particularly in the sample BMN109,
536 pointing to a primitive mantellic source (Sun and McDonough, 1989) (high Cr: 87–1129 ppm, Ni: 24–
537 313 ppm and Co: 27–44 ppm). Micaschist is distinguished from the amphibolite by higher Si content
538 ($SiO_2 \sim 61.68 \text{ wt\%}$), lower CaO ($\sim 6.92 \text{ wt\%}$), lower Fe ($Fe_2O_3 \sim 8.11 \text{ wt\%}$) and lower MgO (~ 2.41
539 wt%, $Mg\# = 0.37$), which suggest that its protolith corresponds either to a more felsic magmatic rock
540 or a more mature sediment.

541

542 **4.4.2. Paragneiss**

543 The paragneiss has a metapelitic composition, with $\text{SiO}_2 \sim 61.66\%$, $\text{Al}_2\text{O}_3 \sim 17.95 \text{ wt\%}$, $\text{K}_2\text{O} \sim 2.94 \text{ wt\%}$,
544 and $\text{Na}_2\text{O} \sim 2.08 \text{ wt\%}$. It is rich in Fe and Mg and shares with amphibolite and micaschist a relatively
545 high content in transition metals, such as Cr (217 ppm), V (139 ppm), Ni (71 ppm), and a low Th/Sc
546 ratio (0.17). Its chondrite-normalized REE pattern has a slight negative slope, with no Eu anomaly,
547 and a flat trend in the HREE (Fig. 17a), like the amphibolite and the micaschist.

548 Nonetheless, the paragneiss is poor in Fe-Mg compared to the amphibolite and the micaschist ($\text{Fe}_2\text{O}_3 =$
549 7.85 wt%, Mg# = 0.42, $\text{Fe}_2\text{O}_3 + \text{MgO} + \text{MnO} + \text{TiO}_2 = 11.51 \text{ wt\%}$). It is also enriched in LILE (Ba = 608
550 ppm, Rb = 114 ppm, Cs = 5 ppm) compared to the average continental crust (Rudnick and Gao, 2003),
551 but also to the granodioritic gneiss and K-rich granitoids of the Mangodara district.

552

553 **4.4.3. Granodioritic-tonalitic-trondhjemitic gneisses and plutonic rocks**

554 In the Nesbitt and Young diagram (Fig. 18a, Nesbitt and Young, 1982, 1984), gneisses and granitoids
555 of the Mangodara district plot just below the feldspar join, which can be attributed to the presence of
556 ferromagnesian minerals and indicates that these rocks were not significantly affected by
557 metasomatism or chemical weathering.

558 Gneiss and granitoids correspond to calc-alkalic granitoids with metaluminous composition (Fig. 18b),
559 like most Eburnean granitoids (Castaing et al., 2003; Ilboudo et al., 2020). The granodioritic gneiss,
560 the hornblende-biotite granodiorite with mica-rich enclaves and the GG-granitoids have chemical
561 affinities typical of a calc-alkaline K-rich series, whereas the tonalitic-trondhjemitic gneiss, the
562 trondhjemite, and the two-mica tonalite have the chemical affinity of a Na-rich series (Fig. 18c). Their
563 modal composition in the Quartz, Alkali feldspar, Plagioclase (QAP) diagram widely correspond to
564 granodiorite or tonalite, but the trondhjemite lies in domain of diorite (Fig. 18d). Except for the
565 trondhjemite and the monzogabbro ($\text{SiO}_2 < 52 \text{ wt\%}$, Fig. 18c and e), the gneisses and other granitoids
566 match some of the geochemical criteria of TTG *sensu stricto*: high SiO_2 (62–72 wt%, Fig. 18e),
567 significant Na_2O (3.85–5.85 wt%), absent Eu and Sr anomalies, LREE >> HREE (high La/Yb, Fig.

568 18f), negative Nb-Ta-Ti anomalies (Martin and Moyen, 2002). Moreover, they match subcategories of
569 middle- to high pressure TTG features (Moyen, 2011), namely, moderate to high Sr/Y ratio (26–215,
570 Fig. 18f), high Sr (473–788), low Ce/Sr (< 0.18). Characteristics of the high pressure TTG typically
571 correspond to the ones of tonalitic-trondhjemite gneiss and of the two-mica tonalite (Fig. 18f).

572 Granodioritic gneiss and tonalitic-trondhjemite gneiss have low Mg#, between 0.38 and 0.52, which
573 are lower than the values for the amphibolite (0.55–0.57) but encompass the one for the paragneiss
574 (0.42). Chondrite-normalized REE patterns of both gneiss types have negative slopes like those shown
575 by plutonic rocks (Fig. 17b). The primitive mantle-normalized pattern of the gneisses (Fig. 17d)
576 unveils a higher enrichment in LILE (Cs, Rb, Ba) than in high field-strength elements (HFSE; Hf, Zr,
577 Y, HREE), which is characteristic of the paragneiss, of granitoids in the Mangodara district and also of
578 the bulk continental crust (Rudnick and Gao, 2003). Negative Nb, Ta and Ti anomalies of the
579 granodioritic gneiss are similar to those of the amphibolite, micaschist and paragneiss (Fig. 17c and d).

580 The granodioritic gneiss and microgranular enclave are characterized by high K content (2.74–3.33
581 wt% K₂O), whereas the tonalitic-trondhjemite gneiss has a low K content (0.81–1.2 wt% K₂O) but is
582 richer in Na (4.95–5.85 wt% Na₂O). The high Na content in tonalitic-trondhjemite gneiss is consistent
583 with the predominance of oligoclase in this rock. The tonalitic-trondhjemite gneiss presents a higher
584 fractionation of LREE vs HREE (La_N/Yb_N = 20–39) than the granodioritic orthogneiss (La_N/Yb_N =
585 16–25) and is depleted in REE. The tonalitic-trondhjemite gneiss is also depleted in transition metals
586 (40–85 ppm Cr, 24–61 ppm Cu, 5–40 ppm Ni, 3–10 ppm Co). These depletions might be induced by
587 fractional crystallization leading to segregation of early crystallizing mafic minerals.

588 The hornblende-biotite granodiorite, the GG-granitoids and the trondhjemite are mostly metaluminous,
589 whereas the two-mica tonalite is weakly peraluminous (Fig. 18b). They are depleted in HFSE and lie
590 in the domain of unfractionated M-type, I-type and S-type granites according to the criteria of Whalen
591 et al. (1987) used for discrimination of A-type. This indicates that they are poorly differentiated
592 magma, and do not match the signature of anorogenic granitoids. Plutonic rocks are subdivided into

593 K-rich and Na-rich series, which can be extended to the gneisses (K-rich granodioritic gneiss, and Na-
594 rich tonalitic-trondhjemitic gneiss).

595 The K-rich series, comprising the hornblende-biotite granodiorite with mica-rich enclaves and the GG-
596 granitoids, is defined by a high K content (2.78–3.56 wt% K_2O , Fig. 18c), low Na content (3.65–4.29
597 wt% Na_2O) and intermediate Mg# (0.33–0.42). They are also characterized by high content in Sr
598 (473–788 ppm), and Ba (606–1071 ppm). The monzogabbro corresponds to the K-poor mafic end-
599 member of this series (2.28 wt% K_2O , $SiO_2 = 51.86$ wt%, Mg# = 0.49) and displays a slightly higher
600 content in Na (4.30 wt% Na_2O), relatively high P content (0.45 wt% P_2O_5), weak fractionation of
601 LREE vs HREE ($La_N/Yb_N \sim 9$), and higher HREE content. K-rich granitoids lay in the high-K calc-
602 alkaline domain in the SiO_2 vs K_2O diagram (Fig. 18c).

603 The Na-rich series, composed of the trondhjemite and the two-mica tonalite, is defined by low K, high
604 Na contents (1.39–1.60 wt% K_2O , 5.46–7.12 wt% Na_2O), and by intermediate Mg# (0.37–0.44). Their
605 high Na content is correlated with the abundance of oligoclase. The trondhjemite is singularized by a
606 low silica content ($SiO_2 \sim 59.23$ wt%), which sets it in the compositional domain of medium calc-
607 alkaline series. Na-rich granitoids are globally depleted in REE relative to the K-rich granitoids. The
608 two-mica tonalite presents the highest LREE/HREE fractionation among the plutonic rocks and is
609 strongly depleted in Nb and Ta, like the tonalitic-trondhjemitic gneiss.

610

611 **4.4.4. Pegmatites**

612 An intrinsic characteristic of pegmatites is to feature variable and commonly coarse grain size and
613 heterogeneous textures. Therefore, despite our efforts during sampling, the major-element composition
614 obtained from whole-rock data should be taken with caution. Nevertheless, some general trends can be
615 identified. In particular, the ratios of elements (e.g. K/Rb, Nb/Ta) that have similar geochemical
616 behaviors can be considered to be relatively independent of the major mineral mode and be used as
617 proxy of the degree of magmatic differentiation with respect to a primitive composition (Ballouard et
618 al., 2016; Bau, 1996; Černý et al., 1985; Shaw, 1968; Taylor, 1965). For instance, pegmatites at

619 Mangodara have lower K/Rb and Ca/Cs ratios compared to granitoids (Table 4, Fig. 18g), except for
620 titanite-allanite pegmatite, which is characterized by high K/Rb (989) and Ca/Cs (~68900) ratios
621 (Table 4). Also compared to granites, pegmatites are manifestly characterized by low Zr/Hf and Nb/Ta
622 ratios (Nb/Ta < 7, Zr/Hf < 34, Table 4, Fig. 18h).

623 Titanite-allanite pegmatite has a high Na content (5.17 wt%), whereas P is below the detection limit,
624 although apatite is present in the sampled dyke. Again, this may be due to sampling-induced bias. It is
625 also characterized by lower contents in Cs, Rb, Nb, Ta, and HREE than the other pegmatite types (see
626 Table 4, Fig. 17f), and, specific to this variety, a markedly positive Eu anomaly.

627 Apatite-zircon pegmatite is also Na-rich (6.32 w%) and has high REE contents (83 ppm), consistent
628 with the abundance of apatite in this sample (Fig. 17e). Its chondrite-normalized REE spider diagram
629 shows a relative depletion in LREE which increase slightly from La to Sm, and a negative Eu
630 anomaly. Another difference with the other varieties is its enrichment in LILE and HFSE (Nb, Ta, Zr,
631 Hf) (Fig. 17f).

632 The garnet-columbite pegmatite has high K and low Ca contents ($K_2O \sim 5.46$ wt%; $CaO < 0.47$ wt%),
633 consistent with the abundance of K-feldspar and the albitic composition of plagioclase. This pegmatite
634 is rich in LILE (Fig. 17e) and possesses the lowest values in K/Rb (180) and Ca/Cs (899) of all
635 pegmatites. Its chondrite-normalized REE pattern show a depletion in HREE, and a strong negative Eu
636 anomaly.

637 Finally, the garnet-REE pegmatite is Na-rich ($Na_2O \sim 6.35$ wt%) with low K_2O (0.52 wt%). It is
638 significantly enriched in HREE, as indicated by the positive slope in chondrite-normalized HREE
639 pattern. It has a lower content in LILE than the other pegmatites (particularly in Ba), but is richer in U
640 and Th.

641

642 **5. Discussion**

643 **5.1. Protoliths of amphibolite, micaschist and paragneiss**

644 Amphibolite and micaschist rafts are very heterogeneous in mineralogy (variably rich in muscovite,
645 sericite, biotite or hornblende), likely reflecting the heterogeneity of their protoliths. The REE pattern
646 and negative Nb, Ta and Ti anomalies of amphibolite and micaschist samples show similarities with
647 Birimian calc-alkaline basalt and andesite (Fig. 17b), suggesting that they may represent metamorphic
648 equivalents of these rocks. This interpretation is consistent with the greenschist facies metamorphic
649 gradient observed in alternating sequences of mafic-felsic volcanic rocks (basalts, andesite, dacite and
650 rhyolite) with metapelites-metagreywackes of the Banfora greenstone belt. Indeed, Birimian series
651 evolves to amphibolite facies with the transformation of basalt to amphibolite and occurrence of
652 kyanite+staurolite+garnet in metarhyolites (Ilboudo et al., 2017b) near the border of the SGGC, to the
653 north-west of the Mangodara district (Fig. 19).

654 The structure and geochemical composition of the paragneiss is typical of a detrital sedimentary
655 protolith made of alternations of pelites and greywackes, which are also sedimentary rocks occurring
656 in Birimian greenstone belts (Asiedu et al., 2004; McFarlane et al., 2011; Roddaz et al., 2007). The
657 low Th/Sc ratio (0.17) and high Fe-Mg and transition metal (Cr, V, Ni) contents of the paragneiss,
658 together with REE pattern being identical with those of amphibolite and micaschist are consistent with
659 a predominant mafic source for their sedimentary protolith, likely derived from erosion of nearby
660 greenstone belts.

661

662 **5.2. Nature and protoliths of the granodioritic and tonalitic-trondhjemitic gneisses**

663 **5.2.1. Diatexite model vs plutonic model**

664 The various gneisses and associated plutonic rocks exposed at the lowest structural level of the
665 Baoulé-Mossi domain, loosely designated as gneiss-granitoid complexes, had been first considered to
666 represent the Archean basement of the Birimian series (Arnould, 1961; Ducellier, 1963; Hottin and
667 Ouedraogo, 1975; Tagini, 1971). This proposition was later discarded when U-Pb geochronology on

668 zircon showed Paleoproterozoic values and no hint of Archean ages (Gasquet et al., 2003; Grenholm
669 et al., 2019a; Parra-Avila et al., 2017; Wane et al., 2018). In the Mangodara district, granodioritic and
670 tonalitic gneisses contain enclaves and rafts of amphibolite, micaschist and paragneiss, attributed to
671 the Birimian series. These occurrences confirm the absence of basement rocks in the Mangodara
672 district, even at the lowest exposed structural level.

673 Pursuing this line of reasoning, several authors proposed that the gneiss-granitoid complexes
674 correspond to plutonic rocks that intruded the greenstone belts during the Eburnean orogeny (Gasquet
675 et al., 2003; Vidal et al., 2009) based on the presence/absence of layering and the predominance of a
676 magmatic texture or ductile fabric, further distinguished in syntectonic and late-tectonic intrusions
677 (Gasquet et al., 2003; Hirdes et al., 1996). On the other hand, Gasquet et al. (2003) used the similarity
678 in isotopic signatures (ϵ_{Nd} , and $^{87}\text{Sr}/^{86}\text{Sr}$) of these granitoid-gneisses with the ones of the Birimian
679 series (basalt and granite) to infer a common source for all these magmatic rocks.

680 In the Mangodara district, our structural analysis shows that the granodioritic and tonalitic gneisses
681 occupy a distinct structural position. The granodioritic gneiss is mantling a dome cored by tonalitic
682 gneiss (Fig. 19). If one considers the plutonic model, this relative position would imply that the
683 granodioritic gneiss formed a regional scale laccolith overlying a pluton of tonalitic-trondhjemitic
684 gneiss. Alternatively, this distribution could result from crustal-scale melt/crystal segregation within a
685 partially molten orogenic root (Vanderhaeghe, 2009), whereby these gneisses could correspond to
686 diatexites. In other words, they would represent former partially molten rocks characterized by a
687 heterogeneous groundmass of granitic composition enclosing enclaves of gneisses and schists (Brown,
688 1973; Brown et al., 1995; Burg and Vanderhaeghe, 1993; Cavalcante et al., 2016; Martini et al., 2019;
689 Mehnert, 1968; Saha-Fouotsa et al., 2019; Sawyer, 1991; Schwindinger and Weinberg, 2017;
690 Vanderhaeghe, 2009, 2001; Vanderhaeghe et al., 1999; Weinberg et al., 2013). The observation of a
691 magmatic fabric overprinted by ductile deformation under sub-magmatic to solid state conditions,
692 indicating a temperature of about 650 °C (Drury and Urai, 1990; Gapais and Barbarin, 1986; Hirth and
693 Tullis, 1992; Law, 2014; Passchier and Trouw, 2005), is in line with a syntectonic emplacement of
694 plutons but also with deformation of partially molten rocks in the course of their crystallization.

695 Additional evidences in favor of a diatexite include the presence of numerous rafts and enclaves of
696 migmatitic amphibolite, micaschist and paragneiss showing diffuse contacts with the granodioritic
697 gneiss host, as well as occurrence of leucosome veins in textural continuity with its groundmass. This
698 also means that metamorphic conditions reached higher supra solidus temperatures (up to 850 °C, Fig.
699 14a) than the ones indicated by metamorphic assemblages of paragneiss (650–680 °C), to achieve the
700 voluminous melt production (~30 %) needed to constitute diatexites (Brown, 1994; Diener et al., 2014;
701 Schwindinger et al., 2019; Vielzeuf and Holloway, 1988; White et al., 2003). The heterogeneous
702 microstructure/textue of this groundmass, and in particular quartz and/or feldspar pockets coating
703 phenocrysts (Fig. 4b, Fig. 9), is typical of crystallization of an interstitial melt (Hasalová et al., 2015;
704 Holness et al., 2011; Sawyer, 2010; Schulmann et al., 2009; Závada et al., 2018). The formation of
705 such diatexites implies accumulation of melt in the partial-melting zone, which signifies an inefficient
706 migration of the newly-formed melt away from the source (Sawyer, 1991; Vanderhaeghe, 2009). In
707 this case, the inherited metamorphic structure is susceptible to be blurred or even erased during flow
708 of this mixture of crystals and melt (Burg and Vanderhaeghe, 1993; Schulmann et al., 2009; Závada et
709 al., 2018).

710 In the neighboring district of Téhini (south continuity of the Mangodara district) a biotite granodioritic
711 gneiss locally migmatitic, designated as “Comoé type gneiss” (Hirdes et al., 1996), is dated at $2152 \pm$
712 2 Ma by U-Pb method in zircon, and 2100 ± 3 Ma by U-Pb method in titanite. The latter was
713 interpreted as a resetting by regional metamorphism, on the basis of low Th/U in titanite (~0.2). In
714 agreement with the diatexite model of the granodioritic gneiss, the zircon age concomitant with the
715 ME1 might record changes in the chemical composition of the melt during the diatexite genesis
716 (Kelsey et al., 2008; Kelsey and Powell, 2011; Yakymchuk and Brown, 2014) instead of magmatic
717 crystallization.

718 The magmatic texture of the tonalitic-trondhjemitic gneiss homogeneous at a regional scale, might
719 either reflect a plutonic origin or a zone of accumulation-aggregation of magmatic and residual
720 minerals within the partially molten zone. The discordance between the tonalitic-trondhjemitic gneiss
721 relative to the foliation of the granodioritic gneiss, though, is in favor of an intrusive contact. As a
28

722 plagioclase-rich mush, the emplacement of the tonalitic-trondhjemite cannot be achieved by melt
723 alimentation through channels, but instead by ascent of the buoyant plagioclase-rich mush in the
724 mantling gneiss, provoking deflection of the structure of the granodioritic gneiss. The formation of the
725 dome is attributed to the development of a gravitational instability that predominated over the regional
726 NE-SW deformation pattern. Crystallization of the titanite-allanite pegmatite dated at 2094.3 ± 8.8 Ma
727 by U-Pb on zircon, implies that the tonalitic-trondhjemite gneiss crystallization occurred
728 approximately at this time, which corresponds to the end of ME2 defined by Baratoux et al. (2011).
729 The Mangodara dome formed also during this period during progressive D1-D2 deformation described
730 by Chardon et al. (2020), by local deflection induced by the ascent of the plagioclase-rich mush.

731 The occurrence in tonalitic-trondhjemite gneiss of tonalitic veins hosting poikilitic hornblende-biotite
732 implies that its segregation occurred in the presence of H₂O, which favors a melting reaction with
733 formation of hydrous peritectic phases (Berger et al., 2008; Sawyer, 2010; Tafur and Diener, 2020;
734 Weinberg, 1999; Weinberg and Hasalová, 2015). In the context of the Mangodara district, H₂O-
735 saturation more likely represents late saturation induced by cooling of the tonalitic-trondhjemite
736 gneiss (Annen and Burgisser, 2020; Clemens and Stevens, 2015; Clemens and Watkins, 2001), rather
737 than dehydrating anatectic reactions (Sawyer, 2010) or dewatering of the lower crust caused by a flux
738 of mantle-derived CO₂-rich fluids (Cuney and Barbey, 2014; Touret and Hartel, 1990; Touret and
739 Huizenga, 2011; Touret and Nijland, 2013).

740 The pressure of 7 kbar inferred from the thermodynamic modelling of the migmatitic paragneiss is
741 interpreted to record the depth of the onset of partial melting, whereas the pressure of 4 to 6 kbar
742 recorded by the granodioritic and tonalitic gneisses is considered to correspond to the depth of
743 crystallization. The difference of 1 to 3 kbar between partial melting and crystallization is consistent
744 with regional exhumation of about 3 to 9 km between these two processes as well as with upward
745 motion of the tonalitic gneiss relative to the granodioritic gneiss during this period.

746 Ages of ca. 2094 Ma obtained in rocks from the core of the dome appear to be older than the ages of
747 2055 and 2041 Ma obtained in the mantling units. The similarity in U-Pb zircon and apatite ages
748 obtained in the core of the dome is consistent with rapid cooling following crystallization of the
29

749 tonalitic gneiss and enclosing pegmatites. However, younging of apatite U-Pb ages upsection is
750 difficult to reconcile with a simple scenario of crustal cooling after exhumation, which would yield the
751 opposite younging trend, namely downsection. This discrepancy might be tentatively attributed to the
752 difference in the size of the apatite grain (Cherniak et al., 1991; Dodson, 1973) that are significantly
753 larger in samples from the core of the dome (~200 µm) compared to the ones from the mantle of the
754 dome (~300 µm). However, such reasoning, if correct in theory, cannot be demonstrated with the
755 geochronological data as all ages are overlapping within error margins.

756

757 **5.2.2. Geochemical constraints on the protolith of the gneisses**

758 *Paragneiss as sources of the granodioritic gneiss*

759 Generation of a K-rich melt is expected in case of partial melting reactions involving dehydration of
760 K-bearing minerals such as micas (Gardien et al., 1995; Le Breton and Thompson, 1988; Montel and
761 Vielzeuf, 1997; Patiño Douce and Beard, 1995; Rapp and Watson, 1995; Thompson, 1982; Vielzeuf
762 and Holloway, 1988; Vielzeuf and Montel, 1994; Wyllie and Wolf, 1993). In the studied area, the
763 most mica-rich lithology corresponds to the paragneiss, which is thus a good candidate to generate a
764 K-rich melt. Alternatively, a K-rich-melt might reflect the presence of residual plagioclase in the
765 partially molten rock, which increases the K₂O/Na₂O ratio in the anatetic melt comparatively to the
766 source (Laurent et al., 2014). This implies a fractionation of K₂O/Na₂O ratio by residual plagioclase
767 (stable for almost P < 15 kbar) with low degree of partial melting to prevent entrainment of
768 plagioclase. The latter hypothesis is unsuited with the high degree of partial melting suggested by the
769 field observations reported in the previous section.

770 Further exploring the scenario of an origin of the K-rich series by partial melting of paragneiss, it
771 appears that the granodioritic gneiss shows a slight depletion in LILE (Rb, Cs, see Fig. 17b) compared
772 to its alleged protolith. Reaching such a composition requires the contribution of a LILE-poor source,
773 such as the amphibolite and micaschist, to dilute LILE concentration in the granodioritic anatetic
774 melt. On the other hand, the absence of Nb and Ta fractionation between the granodioritic gneiss and

775 the amphibolite, micaschist and paragneiss, suggests that partial melting occurred at a pressure inferior
776 to the stability domain of rutile (< 10–15 kbar, Diener et al., 2007; Foley et al., 2002; Green et al.,
777 2016; Moyen and Stevens, 2006). The slight enrichment in LREE of the granodioritic gneiss relative
778 to the amphibolite, micaschist and paragneiss, signs for an incompatible behavior of LREE that could
779 be highly soluble during partial melting. Further, the depletion in HREE and Y, implies a fractionation
780 by REE-bearing minerals such as garnet or amphibole, which is also consistent with the low Fe, Mg,
781 and Ti content of the granodioritic gneiss compared to amphibolite, micaschist and paragneiss. This
782 proposition is further supported by the presence of peritectic garnet in the migmatitic paragneiss (Fig.
783 7d, e and f), and of hornblende-bearing leucosomes in the amphibolite (Fig. 5c). Altogether, the weak
784 fractionation of REE, Nb, Ta, and the typical high Cr, Ba and Sr content (e.g., 134–227 Cr ppm in
785 granodioritic gneiss, 32–189 ppm in K-rich plutonic rocks) suggests that the granodioritic gneiss
786 resulted from high degree partial melting of a mixed source that would include amphibolite (1129 ppm
787 Cr), micaschist and paragneiss (217 ppm Cr), whose resisters and/or restites are observed as rafts in
788 the granodioritic diatexite. Peritectic hornblende and garnet fractionated ferromagnesian elements,
789 HREE and Y.

790

791 *Amphibolites as sources of the tonalitic-trondhjemitic gneiss*

792 In general, tonalitic and trondhjemitic magmas are considered to be generated by partial melting of an
793 hydrated mafic source under pressures higher than 10 kbar, required to destabilize plagioclase
794 (Atherton and Petford, 1993; Barker, 1979; Barker and Arth, 1976; Drummond et al., 1996; Moyen et
795 al., 2009; Patiño Douce and Beard, 1995; Peacock et al., 1994; Petford and Atherton, 1996; Rapp et
796 al., 1991; Rapp and Watson, 1995; Rushmer, 1991; Skjerlie and Patiño Douce, 2002; Winther and
797 Newton, 1991; Wyllie and Wolf, 1993). The tonalitic-trondhjemitic gneiss is characterized by
798 relatively low content in Mg (0.38–0.46 Mg#) and transition metals (Cr, Cu, Ni) that allow to refute an
799 origin by direct partial melting of a mantle source or a mantle contamination. Alternatively, the
800 tonalitic-trondhjemitic assemblage could be generated by partial melting of Birimian amphibolites and

801 mafic schists. The lack of negative Eu anomaly in the gneiss implies that fractional crystallization of
802 plagioclase in equilibrium with a melt is not involved in its genesis. Laurent et al. (2020) proposed that
803 trondhjemitic magmas could be formed by plagioclase accumulation and amphibole fractionation from
804 a tonalitic-granodioritic parental melt (Fig. 18c). However, in Mangodara, the structural position of the
805 tonalitic-trondhjemitic gneiss under the granodioritic gneiss is not consistent with this such a scenario,
806 as a fractionated magma tends to segregate toward the upper part of the partially molten zone or to
807 migrate out of the partially molten zone to intrude the upper crust (Hildreth, 2004; Jackson et al.,
808 2018, 2003; Vanderhaeghe, 2009). A compliant model assimilates the tonalitic-trondhjemitic gneiss to
809 a tonalitic melt coming from a deeper zone of partial melting affecting a predominantly mafic protolith
810 (such as Birimian amphibolites) (Ilboudo et al., 2021), which evolves into a mush composed of
811 clustered residual plagioclase. Partial melting of amphibolite produces a residue dominated in
812 composition by plagioclase and pyroxene (Fig. 14b and d). The absence in tonalitic-trondhjemitic
813 gneiss of products of dehydration melting reactions in the source (e.g. garnet, pyroxene) as well as the
814 scarcity of rafts in textural continuity with the gneiss is consistent with a migration of the tonalitic-
815 trondhjemitic magma away from its source, leaving at least part of its residual solid at a lower
816 structural level.

817 When compared to the amphibolite and micaschist, the tonalite-trondhjemitic gneiss is enriched in
818 LILE (K, Cs, Rb), and W, but depleted in HFSE such as Nb, Ta, Ti, Y and HREE. Two possible
819 processes can explain these depletions:

820 (1) Some elements are fractionated by residual minerals in restites of the partially melted amphibolites
821 and schists, or by early magmatic minerals during the rise of the parental melt. Specifically, this
822 implies the segregation of Nb, Ta, Ti and HREE by rutile at $P > 15$ kbar (Drummond et al., 1996;
823 Foley et al., 2002; Hoffmann et al., 2011; Moyen and Stevens, 2006), Y and HREE by garnet at $P > 10$
824 kbar (Drummond et al., 1996; Hoffmann et al., 2011; Moyen and Stevens, 2006), LREE by early
825 magmatic allanite, titanite and phosphates (Brooks et al., 1981; Green and Pearson, 1987, 1986;
826 Hermann, 2002; Solgadi et al., 2007; Tiepolo et al., 2002). Moreover, amphibole extraction in the

827 parental melt can enhance depletion in REE and increase of the La/Yb and Sr/Y ratios in the tonalite-
828 trondhjemite (Liou and Guo, 2019; Reichardt and Weinberg, 2012).

829 (2) Following the model of Laurent et al. (2020), incompatible LILE and HFSE are entrained in the
830 residual liquid during crystallization of the parental melt of the tonalitic-trondhjemitic gneiss. The
831 liquid migrates upward and emplaces at an upper level of the crust to form granitic plutons or silicic
832 volcanic rocks (Laurent et al., 2020).

833 Whether it results from high pressure melting of amphibolites, or fractional crystallization of a
834 parental tonalitic melt, the source of the tonalitic-trondhjemitic gneiss is located in structural levels
835 below the granodioritic gneiss (Fig. 19), which is in agreement with the pressure-related classification
836 of TTG proposed by Moyen, (2011). As mafic composition of the source is more likely to result in
837 tonalitic magmas, the protolith should be dominated by Birimian amphibolites over metasediments
838 (Fig. 20). Partial melting predominantly of a mafic component is consistent with the affinity of the
839 tonalitic magma with the plagioclase-rich Na-rich series. According to this scenario, REE and HFSE
840 fractionation in the tonalitic-trondhjemitic gneiss would be achieved by clustering of residual minerals
841 or fractional crystallization.

842

843 **5.3. Petrogenesis of the K-rich and Na-rich magmatic series**

844 *K-rich plutonic rocks*

845 The monzogabbro, hornblende-biotite granodiorite and GG granitoids, which display a mineralogy
846 and geochemical signature similar to those of the granodioritic gneiss, are interpreted to represent
847 differentiated terms of the K-rich magmatic series. Their structural position in diffused but locally
848 cross-cutting contact with the granodioritic gneiss further suggests that they correspond to magmas
849 that segregated *in-situ* during deformation (Fig. 19 and Fig. 20).

850 The hornblende-biotite granodiorite is edged by shear zones that probably controlled melt migration
851 (Archanjo et al., 1999; de Saint Blanquat et al., 2011, 1998; Gleizes et al., 1997; Weinberg et al.,

852 2004), and permit melt accumulation in a lower part of the granodioritic gneiss (Fig. 19). Megacrystic
853 plagioclase in this granodiorite are witnesses of an extended magmatic growth as in a magmatic
854 chamber.

855 In the eastern part of the district, the contact of GG-granitoids with granodioritic gneiss is marked by
856 rhythmic layering that might correspond to melt percolation within the fabric of the granodioritic
857 gneiss (Barbey, 2009; Clemens and Stevens, 2016; Vanderhaeghe, 2009; Weinberg, 1999). In the
858 neighboring Téhini District, the “Bavé type” biotite granodiorite (2137 +9/-7 Ma by U-Pb method on
859 zircon) has been interpreted as the product of partial melting of the “Comoé type” granodioritic gneiss
860 (Hirdes et al., 1996). From our point of view, this granodiorite might be the product of melt
861 accumulation within the granodioritic diatexite, which crystallized at the end of the ME1.

862 The monzogabbro could result from accumulation of hornblende separated from a granodioritic
863 assemblage. A similar scenario has been proposed for hornblendite in Xuanmenzi-Gualanyu region
864 (Neoarchean, North China Craton), resulting in decreased Sr/Y and La/Yb ratios (Liou and Guo,
865 2019).

866

867 *Na-rich plutonic rocks*

868 The plagioclase-rich trondhjemite, which has geochemical features similar to the tonalitic-
869 trondhjemitic gneiss (K-poor, low HFSE and REE), could have resulted from accumulation of
870 plagioclase floating at the roof of the tonalitic-trondhjemitic gneiss. The peraluminous composition of
871 the two-mica tonalite can be attained by fractionation of biotite and hornblende in the plagioclase-rich
872 melt (Chappell et al., 2012). Moreover, the composition of the tonalitic-trondhjemitic gneiss, which is
873 intermediate between the trondhjemite and the two-mica tonalite is consistent with this proposition
874 (Fig. 18d and e). Its position occupying the roof of tonalitic-trondhjemitic gneiss in perfect
875 concordance with its southern margin, corroborates an origin as a melt extracted from the tonalitic-
876 trondhjemitic gneiss (Fig. 19). The lower proportion of plagioclase in this melt stands with a relative

877 increase of K, stabilizing micas instead of amphibole, whereas the depleted REE and HFSE signatures
878 are inherited from the tonalitic-trondhjemite gneiss (Fig. 20).

879

880 **5.4. Petrogenesis of the rare metal-bearing pegmatites**

881 Textural continuity of titanite-allanite pegmatites with veins concordant to the foliation of the
882 tonalitic-trondhjemite gneiss, suggests that the pegmatite-forming magma segregated from the
883 tonalitic-trondhjemite mush itself. Sharp contacts of discordant pegmatite veins observed in other
884 places indicate that the pegmatite-forming magma migrated when the tonalitic-trondhjemite gneiss
885 cooled below the ductile-to-fragile transition, which also fulfills the undercooling conditions needed
886 for nucleation of pegmatitic crystals (London, 1989, 2009, 2014). Accordingly, titanite-allanite
887 pegmatites are interpreted as the late residual melt enriched in volatile elements segregated during
888 crystallization of the tonalitic magma (Fig. 19). Its higher K/Rb and Ca/Cs ratios, and lower contents
889 in Nb, Ta and REE than other pegmatites show that the titanite-allanite is the least differentiated of the
890 Mangodara pegmatite types.

891 Apatite-zircon pegmatites are lithologically discriminated from the titanite-allanite type only by their
892 occurrence in granodioritic gneiss and absence of allanite and epidote. Therefore, the two types could
893 be cogenetic and derived from a single source, or alternatively, the apatite-zircon type could represent
894 the residual melt after crystallization of the titanite-allanite pegmatites. An origin by fractional
895 crystallization is further suggested by the relative LILE and REE enrichment in apatite-zircon
896 pegmatites compared to the titanite-allanite type, which reflects a differentiation trend. However, Eu
897 was segregated preferentially to other REE in titanite-allanite pegmatite, as indicated by its positive
898 anomaly. This behavior is probably enhanced by the presence of Eu-bearing minerals in the titanite-
899 allanite pegmatite (allanite, apatite), resulting subsequently in the relative depletion of Eu apatite-
900 zircon pegmatite.

901 Textural continuity of garnet-columbite pegmatites (Li, Nb enriched) with concordant and discordant
902 leucosome veins of the migmatitic paragneiss is consistent with segregation of the pegmatite-forming

903 magma from the partially molten paragneiss. Their transposition into the foliation of the paragneiss
904 indicates that this segregation is coeval with deformation. The high differentiation degree of garnet-
905 columbite pegmatites compared to other plutonic rocks in the Mangodara district is proposed to
906 correspond to the segregation of an anatetic melt seeping from partially molten paragneiss (Fig. 19).

907 The textural continuity of garnet-REE pegmatite (Ti, Y, HREE enriched) with concordant leucosome
908 veins of the granodioritic gneiss points to an origin by melt segregation during crystallization of the
909 partially molten granodioritic gneiss (Fig. 19). Its higher content in U, Th and REE compared to other
910 pegmatites suggest a different degree of differentiation marked by HFSE enrichment, which is mostly
911 achieved in peralkaline to metaluminous differentiated melt (Černý et al., 2005; Černý and Ercit,
912 2005; Linnen and Cuney, 2005).

913 Uranium-lead age of apatite record the closure of U-Pb isotopic system, which occurs at 450-600 °C
914 for grain size < 1 mm but varies with the grain size and cooling rate (Cherniak et al., 1991; Dodson,
915 1973). Uncertainties on apatite ages of gneisses and apatite-zircon pegmatite span large period which
916 cover the ME2 and ends at 2000 Ma. These data involve a regional cooling occurring after 2100 Ma.
917 This reinforces the idea that a temperature was maintained above 500 °C during at least 50 Ma, which
918 fits a long-lasting tectono-thermal event (Guergouz et al., 2018; Turlin et al., 2018; Vanderhaeghe et
919 al., 2019; Vauchez et al., 2019) encompassing MP-HT metamorphism, diatexite formation, melt
920 accumulation and late segregation of pegmatite-forming melt.

921 In short, the continuous network of granitic veins and pegmatites discordant relative to
922 the foliation of their host gneisses and their magmatic texture plead for a pegmatite formation by
923 syntectonic melt segregation (Brown, 2005, 1994; Burg and Vanderhaeghe, 1993; Sawyer, 2001,
924 1999; Vanderhaeghe et al., 1999; Vanderhaeghe, 2001; Weinberg, 2006; Wickham, 1987), (Fig. 19
925 and Fig. 20). The segregated pegmatite-forming low-viscosity melt is transposed into the flattening
926 plane (Brown et al., 1995; Stevenson, 1989; Vanderhaeghe et al., 1999) but also in low-pressure sites
927 induced by ductile deformation (Brown et al., 1995; Robin, 1979; Stevenson, 1989; Van der Molen,
928 1985; Van der Molen and Paterson, 1979; Vanderhaeghe et al., 1999). After crystallization, the

929 pegmatites become more competent than the host gneisses and are folded and boudinaged with cuspate
930 interfaces without losing their internal texture (Fig. 11e) (Alsop et al., 2021; Bons et al., 2004; Butler
931 and Torvela, 2018; Druguet, 2019).

932

933 **6. Conclusions**

934 Field observations, combined with structural, petrological and geochemical data from rare metal-
935 bearing pegmatites of the Mangodara district indicate that they derived from their gneiss-granitoid
936 hosts, with an input from the rafts of amphibolite, schist and paragneiss enclosed in the latter. Titanite-
937 allanite-bearing and apatite-zircon-bearing pegmatites are in textural continuity with leucosome veins,
938 themselves concordant with the foliation of the granodioritic and tonalitic gneisses. These pegmatites
939 are interpreted as originating from syntectonic melt segregation from a partially molten rock or
940 crystalline mush. On the other hand, the garnet-columbite-bearing and garnet-REE-bearing pegmatites
941 are inferred to derive, respectively, from partial melting of paragneiss and segregation of melt within
942 the granodioritic gneiss.

943 PT conditions of partial melting are constrained by thermodynamic modelling of the migmatitic
944 paragneiss, yielding 650-700 °C for 7 kbar, and of the migmatitic amphibolite with a temperature over
945 750 °C. In this context of MP-HT metamorphism, generation of the granodioritic gneiss by further
946 partial melting of the Birimian series, required a temperature higher than 850 °C to reach the biotite-
947 out isograd and a melt fraction of about 30 % associated with the metatexite/diatexite transition. The
948 low degree of fractionation of HFSE and REE between paragneiss relative to granodioritic gneiss
949 supports such a high degree of partial melting without migration of magma out of the zone of partial
950 melting. A dominant proportion of paragneiss is required in the protolith of the granodioritic gneiss to
951 account for its high-K content, but its weak depletion in LILE is best explained by a minor
952 contribution from the amphibolite and micaschist.

953 The formation of the Na-rich and K-rich magmatic series of the Mangodara district is attributed to
954 partial melting at different pressure (7 to 10 kbar) and in various proportions of amphibolite and

955 paragneiss of the Birimian series followed by melt segregation and/or clustering/accumulation of
956 residual/magmatic crystals. Depletion of REE and HFSE in members of the Na-rich series are
957 explained by plagioclase and amphibole fractionation from a granodioritic/tonalitic parental magma or
958 by clustering of residual plagioclase from an anatetic melt, with separation from a garnet-pyroxene-
959 allanite-titanite-bearing residue.

960 Crystallization of titanite-allanite pegmatite is constrained at 2094.3 ± 8.8 Ma by U-Pb on zircon,
961 whereas cooling below ca. 500 °C is documented by apatite cooling ages of 2094 ± 21 Ma for the
962 granodioritic gneiss and 2055 ± 20 Ma for an apatite-zircon pegmatite.

963 These data favor a segregation model for rare metal-bearing pegmatites of the Mangodara district. This
964 took place within the partially molten root of the Eburnean orogenic crust during formation, between
965 transcurrent shear zones, of a crustal-scale dome cored by a plagioclase-dominated crystal mush and
966 mantled by a heterogeneous diatexite of granodioritic composition.

967

968 **Acknowledgements**

969 This work is developed from a collaboration between the University of Toulouse 3 Paul Sabatier
970 (France) and the University Joseph Ki-Zerbo (Ouagadougou, Burkina Faso). This study benefited from
971 funds provided by the West African Exploration Initiative project (WAXI; AMIRA P934B) and was
972 supported by the French Institut de Recherche pour le Développement (IRD) and the French Embassy
973 in Burkina Faso. We are grateful to the Bureau des Mines et de la Géologie du Burkina (BUMIGEB)
974 for logistic support, field work assistance, and providing data and other information on the study
975 region. We also thank the GeOHeLiS analytical platform (University of Rennes 1) for the LA-ICP-MS
976 analyses on zircon and apatite. Anonymous reviewers provided much appreciated insights that
977 improved the final manuscript.

978

979 **References**

- 980 Abouchami, W., Boher, M., Michard, A., Albarede, F., 1990. A major 2.1 Ga event of mafic
981 magmatism in west Africa: An Early stage of crustal accretion. *J. Geophys. Res. Solid Earth*
982 95, 17605–17629. <https://doi.org/10.1029/JB095iB11p17605>
- 983 Adams, S., 2013. Rare metals mineralization of Winneba-Mankoadze pegmatites, South Western
984 Ghana.
- 985 Allou, A.B., 2005. Facteurs, paramètres, dynamique de distribution et genèse des dépôts de columbo-
986 tantalite d'Issia, centre-ouest de la Côte d'Ivoire. Université du Québec à Chicoutimi.
- 987 Alsop, G.I., Strachan, R.A., Holdsworth, R.E., Burns, I.M., 2021. Geometry of folded and boudinaged
988 pegmatite veins emplaced within a strike-slip shear zone: A case study from the Caledonian
989 orogen, northern Scotland. *J. Struct. Geol.* 142, 104233.
990 <https://doi.org/10.1016/j.jsg.2020.104233>
- 991 Annen, C., Burgisser, A., 2020. Modeling water exsolution from a growing and solidifying felsic
992 magma body. *Lithos* 105799. <https://doi.org/10.1016/j.lithos.2020.105799>
- 993 Anum, S., Sakyi, P.A., Su, B.-X., Nude, P.M., Nyame, F., Asiedu, D., Kwayisi, D., 2015.
994 Geochemistry and geochronology of granitoids in the Kibi-Asamankese area of the Kibi-
995 Winneba volcanic belt, southern Ghana. *J. Afr. Earth Sci.* 102, 166–179.
996 <https://doi.org/10.1016/j.jafrearsci.2014.11.007>
- 997 Archanjo, C.J., da Silva, E.R., Caby, R., 1999. Magnetic fabric and pluton emplacement in a
998 transpressive shear zone system: the Itaporanga porphyritic granitic pluton (northeast Brazil).
999 *Tectonophysics* 312, 331–345. [https://doi.org/10.1016/S0040-1951\(99\)00176-6](https://doi.org/10.1016/S0040-1951(99)00176-6)
- 1000 Arnould, M., 1961. Étude géologique des migmatites et des granites précambriens du nord-est de la
1001 Côte d'Ivoire et de la Haute-Volta méridionale. Ht.-Volta Méridionale BRGM Mém. N 3.
- 1002 Asiedu, D.K., Dampare, S.B., Sakyi, P.A., Banoeng-Yakubo, B., Osae, S., Nyarko, B.J.B., Manu, J.,
1003 2004. Geochemistry of Paleoproterozoic metasedimentary rocks from the Birim
1004 diamondiferous field, southern Ghana: Implications for provenance and crustal evolution at
1005 the Archean-Proterozoic boundary. *Geochem. J.* 38, 215–228.
1006 <https://doi.org/10.2343/geochemj.38.215>
- 1007 Atherton, M.P., Petford, N., 1993. Generation of sodium-rich magmas from newly underplated
1008 basaltic crust. *Nature* 362, 144.
- 1009 Baldwin, J., Powell, R., Brown, M., Moraes, R., Fuck, R., 2005. Modelling of mineral equilibria in
1010 ultrahigh-temperature metamorphic rocks from the Anápolis–Itauçu Complex, central Brazil.
1011 *J. Metamorph. Geol.* 23, 511–531.
- 1012 Ballouard, C., Poujol, M., Boulvais, P., Branquet, Y., Tartèse, R., Vigneresse, J.-L., 2016. Nb-Ta
1013 fractionation in peraluminous granites: A marker of the magmatic-hydrothermal transition.
1014 *Geology* 44, 231–234.
- 1015 Baratoux, L., Metelka, V., Naba, S., Jessell, M.W., Grégoire, M., Ganne, J., 2011. Juvenile
1016 Paleoproterozoic crust evolution during the Eburnean orogeny (~ 2.2–2.0 Ga), western
1017 Burkina Faso. *Precambrian Res.* 191, 18–45.
- 1018 Barbey, P., 2009. Layering and schlieren in granitoids: A record of interactions between magma
1019 emplacement, crystallization and deformation in growing plutons (The André Dumont
1020 medallist lecture). *Geol. Belg.*
- 1021 Barker, F., 1979. Chapter 1 - Trondhjemite: Definition, Environment and Hypotheses of Origin, in:
1022 Barker, F. (Ed.), *Developments in Petrology, Trondhjemites, Dacites, and Related Rocks*.
1023 Elsevier, pp. 1–12. <https://doi.org/10.1016/B978-0-444-41765-7.50006-X>
- 1024 Barker, F., Arth, J.G., 1976. Generation of trondhjemitic-tonalitic liquids and Archean bimodal
1025 trondhjemite-basalt suites. *Geology* 4, 596–600.
- 1026 Bau, M., 1996. Controls on the fractionation of isovalent trace elements in magmatic and aqueous
1027 systems: evidence from Y/Ho, Zr/Hf, and lanthanide tetrad effect. *Contrib. Mineral. Petrol.*
1028 123, 323–333. <https://doi.org/10.1007/s004100050159>
- 1029 Berger, A., Burri, T., Alt-Epping, P., Engi, M., 2008. Tectonically controlled fluid flow and water-
1030 assisted melting in the middle crust: an example from the Central Alps. *Lithos* 102, 598–615.

- 1031 Béziat, D., Bourges, F., Debat, P., Lombo, M., Martin, F., Tollon, F., 2000. A Paleoproterozoic
1032 ultramafic-mafic assemblage and associated volcanic rocks of the Boromo greenstone belt:
1033 fractionates originating from island-arc volcanic activity in the West African craton.
1034 Precambrian Res. 101, 25–47.
- 1035 Block, S., Baratoux, L., Zeh, A., Laurent, O., Bruguier, O., Jessell, M.W., Ailleres, L., Sagna, R.,
1036 Parra-Avila, L.A., Bosch, D., 2016a. Paleoproterozoic juvenile crust formation and
1037 stabilisation in the south-eastern West African Craton (Ghana); New insights from U-Pb-Hf
1038 zircon data and geochemistry. Precambrian Res. 287, 1–30.
- 1039 Block, S., Ganne, J., Baratoux, L., Zeh, A., Parra-Avila, L., Jessell, M.W., Ailleres, L., Siebenaller, L.,
1040 2015. Petrological and geochronological constraints on lower crust exhumation during
1041 Paleoproterozoic (Eburnean) orogeny, NW Ghana, West African Craton. J. Metamorph. Geol.
1042 33, 463–494.
- 1043 Block, S., Jessell, M.W., Aillères, L., Baratoux, L., Bruguier, O., Zeh, A., Bosch, D., Caby, R.,
1044 Mensah, E., 2016b. Lower crust exhumation during Paleoproterozoic (Eburnean) orogeny,
1045 NW Ghana, West African Craton: Interplay of coeval contractional deformation and
1046 extensional gravitational collapse. Precambrian Res. 274, 82–109.
- 1047 Boher, M., Abouchami, W., Michard, A., Albarede, F., Arndt, N.T., 1992. Crustal growth in West
1048 Africa at 2.1 Ga. J. Geophys. Res. Solid Earth 97, 345–369.
1049 <https://doi.org/10.1029/91JB01640>
- 1050 Bohlen, S.R., Wall, V.J., Boettcher, A.L., 1983. Experimental investigations and geological
1051 applications of equilibria in the system FeO-TiO₂-Al₂O₃-SiO₂-H₂O. Am. Mineral. 68, 1049–
1052 1058.
- 1053 Bons, P.D., Druguet, E., Hamann, I., Carreras, J., Passchier, C.W., 2004. Apparent boudinage in
1054 dykes. J. Struct. Geol. 26, 625–636. <https://doi.org/10.1016/j.jsg.2003.11.009>
- 1055 Brooks, C., Henderson, P., Rønsbo, J., 1981. Rare-earth partition between allanite and glass in the
1056 obsidian of Sandy Braes, Northern Ireland. Mineral. Mag. 44, 157–160.
- 1057 Brown, M., 2005. The mechanism of melt extraction from lower continental crust of orogens. Trans R.
1058 Soc Edinb. Earth Sci 95, 35–48.
- 1059 Brown, M., 1994. The generation, segregation, ascent and emplacement of granite magma: the
1060 migmatite-to-crustally-derived granite connection in thickened orogens. Earth-Sci. Rev. 36,
1061 83–130.
- 1062 Brown, M., 1973. The definition of metatexis, diatexis and migmatite. Proc. Geol. Assoc. 84, 371-IN2.
1063 [https://doi.org/10.1016/S0016-7878\(73\)80021-5](https://doi.org/10.1016/S0016-7878(73)80021-5)
- 1064 Brown, M., Averkin, Y.A., McLellan, E.L., Sawyer, E.W., 1995. Melt segregation in migmatites. J.
1065 Geophys. Res. Solid Earth 100, 15655–15679.
- 1066 Burg, J.-P., Vanderhaeghe, O., 1993. Structures and way-up criteria in migmatites, with application to
1067 the Velay dome (French Massif Central). J. Struct. Geol. 15, 1293–1301.
1068 [https://doi.org/10.1016/0191-8141\(93\)90103-H](https://doi.org/10.1016/0191-8141(93)90103-H)
- 1069 Butler, R.W.H., Torvela, T., 2018. The competition between rates of deformation and solidification in
1070 syn-kinematic granitic intrusions: Resolving the pegmatite paradox. J. Struct. Geol. 117, 1–13.
1071 <https://doi.org/10.1016/j.jsg.2018.08.013>
- 1072 Caen-Vachette, M., 1988. Le craton ouest-africain et le bouclier guyanais: un seul craton au
1073 Protérozoïque inférieur? J. Afr. Earth Sci. Middle East 7, 479–488.
- 1074 Castaing, C., Billa, M., Milési, J., Thiéblemont, D., Le Metour, J., Egal, E., Donzeau, M., Guerrot, C.,
1075 Cocherie, A., Chevremont, P., 2003. Notice explicative de la carte géologique et minière du
1076 Burkina Faso à 1/1 000 000. BRGM BUMIGEB 147.
- 1077 Cavalcante, G.C.G., Viegas, G., Archanjo, C.J., da Silva, M.E., 2016. The influence of partial melting
1078 and melt migration on the rheology of the continental crust. J. Geodyn., Fluids in crustal
1079 deformation : fluid flow, fluid-rock interactions, rheology, melting and resources 101, 186–
1080 199. <https://doi.org/10.1016/j.jog.2016.06.002>
- 1081 Černý, P., 1991a. Rare-element Granitic Pegmatites. Part I: Anatomy and Internal Evolution of
1082 Pegmatitic Deposits. Geosci. Can. 49–67.
- 1083 Černý, P., 1991b. Rare-element Granitic Pegmatites. Part II: Regional to Global Environments and
1084 Petrogenesis. Geosci. Can.

- 1085 Černý, P., Blevin, P.L., Cuney, M., London, D., 2005. Granite-related ore deposits.
1086 Černý, P., Ercit, T.S., 2005. The classification of granitic pegmatites revisited. *Can. Mineral.* 43,
1087 2005–2026.
1088 Černý, P., Meintzer, R.E., Anderson, A.J., 1985. Extreme fractionation in rare-element granitic
1089 pegmatites; selected examples of data and mechanisms. *Can. Mineral.* 23, 381–421.
1090 Chalokwu, C.I., Ghazi, M.A., Foord, E.E., 1997. Geochemical characteristics and K-Ar ages of rare-
1091 metal bearing pegmatites from the Birimian of southeastern Ghana. *J. Afr. Earth Sci.* 24, 1–9.
1092 [https://doi.org/10.1016/S0899-5362\(97\)00022-5](https://doi.org/10.1016/S0899-5362(97)00022-5)
1093 Chappell, B.W., Bryant, C.J., Wyborn, D., 2012. Peraluminous I-type granites. *Lithos*, Seventh Hutton
1094 Symposium on Granites and Related Rocks 153, 142–153.
1095 <https://doi.org/10.1016/j.lithos.2012.07.008>
1096 Chardon, D., Bamba, O., Traoré, K., 2020. Eburnean deformation pattern of Burkina Faso and the
1097 tectonic significance of shear zones in the West African craton. *BSGF - Earth Sci. Bull.* 191,
1098 2. <https://doi.org/10.1051/bsgf/2020001>
1099 Cherniak, D.J., Lanford, W.A., Ryerson, F., 1991. Lead diffusion in apatite and zircon using ion
1100 implantation and Rutherford backscattering techniques. *Geochim. Cosmochim. Acta* 55,
1101 1663–1673.
1102 Clemens, J.D., Stevens, G., 2016. Melt segregation and magma interactions during crustal melting:
1103 Breaking out of the matrix. *Earth-Sci. Rev.* 160, 333–349.
1104 <https://doi.org/10.1016/j.earscirev.2016.07.012>
1105 Clemens, J.D., Stevens, G., 2015. Comment on ‘Water-fluxed melting of the continental crust: A
1106 review’ by R.F. Weinberg and P. Hasalová. *Lithos* 234–235, 100–101.
1107 <https://doi.org/10.1016/j.lithos.2015.06.032>
1108 Clemens, J.D., Watkins, J.M., 2001. The fluid regime of high-temperature metamorphism during
1109 granitoid magma genesis. *Contrib. Mineral. Petrol.* 140, 600–606.
1110 Coggon, R., Holland, T., 2002. Mixing properties of phengitic micas and revised garnet-phengite
1111 thermobarometers. *J. Metamorph. Geol.* 20, 683–696.
1112 Cox, K.G., Bell, J.D., Pankhurst, R.J., 1979. *The Interpretation of Igneous Rocks*. Springer
1113 Netherlands, Dordrecht. <https://doi.org/10.1007/978-94-017-3373-1>
1114 Cuney, M., Barbey, P., 2014. Uranium, rare metals, and granulite-facies metamorphism. *Geosci.*
1115 *Front.*, SPECIAL ISSUE: The role of fluids in the lower crust and upper mantle: A tribute to
1116 Jacques Touret 5, 729–745. <https://doi.org/10.1016/j.gsf.2014.03.011>
1117 de Capitani, C., Brown, T.H., 1987. The computation of chemical equilibrium in complex systems
1118 containing non-ideal solutions. *Geochim. Cosmochim. Acta* 51, 2639–2652.
1119 de Capitani, C., Petrakakis, K., 2010. The computation of equilibrium assemblage diagrams with
1120 Theriax/Domino software. *Am. Mineral.* 95, 1006–1016.
1121 De Kock, G., Armstrong, R., Siegfried, H., Thomas, E., 2011. Geochronology of the Birim
1122 Supergroup of the West African craton in the Wa-Bolé region of west-central Ghana:
1123 Implications for the stratigraphic framework. *J. Afr. Earth Sci.* 59, 1–40.
1124 de Saint Blanquat, M., Horsman, E., Habert, G., Morgan, S., Vanderhaeghe, O., Law, R., Tikoff, B.,
1125 2011. Multiscale magmatic cyclicity, duration of pluton construction, and the paradoxical
1126 relationship between tectonism and plutonism in continental arcs. *Tectonophysics* 500, 20–33.
1127 de Saint Blanquat, M., Tikoff, B., Teyssier, C., Vigneresse, J.L., 1998. Transpressional kinematics and
1128 magmatic arcs. *Geol. Soc. Lond. Spec. Publ.* 135, 327–340.
1129 <https://doi.org/10.1144/GSL.SP.1998.135.01.21>
1130 Debat, P., Nikiéma, S., Mercier, A., Lombo, M., Béziat, D., Bourges, F., Roddaz, M., Salvi, S.,
1131 Tollen, F., Wenmenga, U., 2003. A new metamorphic constraint for the Eburnean orogeny
1132 from Paleoproterozoic formations of the Man shield (Aribinda and Tampelga countries,
1133 Burkina Faso). *Precambrian Res.* 123, 47–65. [https://doi.org/10.1016/S0301-9268\(03\)00046-9](https://doi.org/10.1016/S0301-9268(03)00046-9)
1134 Delor, C., Egal, E., Lafon, J.-M., Cocherie, A., Guerrot, C., Rossi, P., Truffert, C., Théveniaut, H.,
1135 Phillips, D., Avelar, V.G., 2003. Transamazonian crustal growth and reworking as revealed by
1136 the 1:500,000-scale geological map of French Guiana (2nd edition). *Géologie Fr.* 5–57.

- 1137 Diener, J.F.A., Powell, R., White, R.W., Holland, T.J.B., 2007. A new thermodynamic model for
1138 clino- and orthoamphiboles in the system Na₂O–CaO–FeO–MgO–Al₂O₃–SiO₂–H₂O–O. *J.*
1139 *Metamorph. Geol.* 25, 631–656. <https://doi.org/10.1111/j.1525-1314.2007.00720.x>
- 1140 Diener, J.F.A., White, R.W., Hudson, T.J.M., 2014. Melt production, redistribution and accumulation
1141 in mid-crustal source rocks, with implications for crustal-scale melt transfer. *Lithos* 200–201,
1142 212–225. <https://doi.org/10.1016/j.lithos.2014.04.021>
- 1143 Dodson, M.H., 1973. Closure temperature in cooling geochronological and petrological systems.
1144 *Contrib. Mineral. Petrol.* 40, 259–274.
- 1145 Doumbia, S., Pouclet, A., Kouamelan, A., Peucat, J., Vidal, M., Delor, C., 1998. Petrogenesis of
1146 juvenile-type Birimian (Paleoproterozoic) granitoids in Central Côte-d'Ivoire, West Africa:
1147 geochemistry and geochronology. *Precambrian Res.* 87, 33–63.
- 1148 Druguet, E., 2019. Deciphering the presence of axial-planar veins in tectonites. *Geosci. Front.* 10,
1149 2101–2115. <https://doi.org/10.1016/j.gsf.2019.02.005>
- 1150 Drummond, M.S., Defant, M.J., Kepezhinskas, P.K., 1996. Petrogenesis of slab-derived trondhjemite–
1151 tonalite–dacite/adakite magmas. *Earth Environ. Sci. Trans. R. Soc. Edinb.* 87, 205–215.
1152 <https://doi.org/10.1017/S0263593300006611>
- 1153 Drury, M.R., Urai, J.L., 1990. Deformation-related recrystallization processes. *Tectonophysics* 172,
1154 235–253. [https://doi.org/10.1016/0040-1951\(90\)90033-5](https://doi.org/10.1016/0040-1951(90)90033-5)
- 1155 Ducellier, J., 1963. Contribution à l'étude des formations cristallines et métamorphiques du Centre et
1156 du Nord de la Haute-Volta. Editions Technip.
- 1157 Fabre, R., Ledru, P., Milési, J.-P., 1990. Le Protérozoïque inférieur (Birimien) du centre de la Côte-
1158 d'Ivoire: évolution tectonique et corrélations. *Comptes Rendus Académie Sci. Sér. 2*
1159 Mécanique Phys. Chim. Sci. Univers Sci. Terre
- 1160 Feybesse, J.-L., Billa, M., Guerrot, C., Duguey, E., Lescuyer, J.-L., Milési, J.-P., Bouchot, V., 2006.
1161 The paleoproterozoic Ghanaian province: Geodynamic model and ore controls, including
1162 regional stress modeling. *Precambrian Res.* 149, 149–196.
- 1163 Foley, S., Tiepolo, M., Vannucci, R., 2002. Growth of early continental crust controlled by melting of
1164 amphibolite in subduction zones. *Nature* 417, 837–840. <https://doi.org/10.1038/nature00799>
- 1165 Fontaine, A., Eglinger, A., Ada, K., André-Mayer, A.-S., Reisberg, L., Siebenaller, L., Le Mignot, E.,
1166 Ganne, J., Poujol, M., 2017. Geology of the world-class Kiaka polyphase gold deposit, West
1167 African Craton, Burkina Faso. *J. Afr. Earth Sci.* 126, 96–122.
- 1168 Ganne, J., Gerbault, M., Block, S., 2014. Thermo-mechanical modeling of lower crust exhumation—
1169 Constraints from the metamorphic record of the Palaeoproterozoic Eburnean orogeny, West
1170 African Craton. *Precambrian Res.* 243, 88–109.
1171 <https://doi.org/10.1016/j.precamres.2013.12.016>
- 1172 Gapais, D., Barbarin, B., 1986. Quartz fabric transition in a cooling syntectonic granite (Hermitage
1173 Massif, France). *Tectonophysics* 125, 357–370. [https://doi.org/10.1016/0040-1951\(86\)90171-X](https://doi.org/10.1016/0040-1951(86)90171-X)
- 1175 García-Casco, A., Haissen, F., Castro, A., El-Hmidi, H., TORRES-ROLDÁN, R.L., Millán, G., 2003.
1176 Synthesis of staurolite in melting experiments of a natural metapelite: consequences for the
1177 phase relations in low-temperature pelitic migmatites. *J. Petrol.* 44, 1727–1757.
- 1178 Gardien, V., Thompson, A.B., Grujic, D., Ulmer, P., 1995. Experimental melting of biotite +
1179 plagioclase + quartz ± muscovite assemblages and implications for crustal melting. *J.*
1180 *Geophys. Res. Solid Earth* 100, 15581–15591. <https://doi.org/10.1029/95JB00916>
- 1181 Gasquet, D., Barbey, P., Adou, M., Paquette, J.L., 2003. Structure, Sr–Nd isotope geochemistry and
1182 zircon U–Pb geochronology of the granitoids of the Dabakala area (Côte d'Ivoire): evidence
1183 for a 2.3 Ga crustal growth event in the Palaeoproterozoic of West Africa? *Precambrian Res.*
1184 127, 329–354. [https://doi.org/10.1016/S0301-9268\(03\)00209-2](https://doi.org/10.1016/S0301-9268(03)00209-2)
- 1185 Giovenazzo, D., Ouedraogo, C., Séjourné, S., Hein, K.A.A., Jébrak, M., Malo, M., Harnois, L.,
1186 Ouedraogo, A., Ouedraogo, P.I., Sountra, Y., Kambou, A., Coulibaly, G.K., Nassa, O., Nassa,
1187 N., Djiguemde, S., Hema, K.A.A., Bagoro, F., 2018. Notice explicative de la carte géologique
1188 1/200 000, Feuille NC-30-XIV, Banfora-Kong, Effigis Géo-Solutions. ed.

- 1189 Gleizes, G., Leblanc, D., Bouchez, J.L., 1997. Variscan granites of the Pyrenees revisited: their role as
1190 syntectonic markers of the orogen. *Terra Nova* 9, 38–41. <https://doi.org/10.1046/j.1365-3121.1997.d01-9.x>
- 1191 Goujou, J., Buscail, F., Théveniaut, H., Dioh, E., Delor, C., Blein, O., Diallo, D., Ndiaye, P., Le
1192 Métour, J., Fullgraf, T., 2010. Notice explicative de la carte géologique à 1/200 000 du
1193 Sénégal, feuille Kossanto-Dalafi Est, 2010, Ministère des Mines, de l'Industrie, de l'Agro-
1194 Industrie et des PME. Dir. Mines Géologie Dakar.
- 1195 Green, E., Holland, T., Powell, R., 2007. An order-disorder model for omphacitic pyroxenes in the
1196 system jadeite-diopside-hedenbergite-acmite, with applications to eclogitic rocks. *Am. Mineral.* 92, 1181–1189. <https://doi.org/10.2138/am.2007.2401>
- 1197 Green, E.C.R., White, R.W., Diener, J.F.A., Powell, R., Holland, T.J.B., Palin, R.M., 2016. Activity–
1198 composition relations for the calculation of partial melting equilibria in metabasic rocks. *J. Metamorph. Geol.* 34, 845–869. <https://doi.org/10.1111/jmg.12211>
- 1199 Green, T., Pearson, N., 1987. An experimental study of Nb and Ta partitioning between Ti-rich
1200 minerals and silicate liquids at high pressure and temperature. *Geochim. Cosmochim. Acta* 51,
1201 55–62.
- 1202 Green, T., Pearson, N., 1986. Rare-earth element partitioning between sphene and coexisting silicate
1203 liquid at high pressure and temperature. *Chem. Geol.* 55, 105–119.
- 1204 Grenholm, M., 2019. The global tectonic context of the ca. 2.27–1.96 Ga Birimian Orogen—Insights
1205 from comparative studies, with implications for supercontinent cycles. *Earth-Sci. Rev.*
- 1206 Grenholm, M., Jessell, M.W., Thébaud, N., 2019a. A geodynamic model for the Paleoproterozoic (ca.
1207 2.27–1.96 Ga) Birimian Orogen of the southern West African Craton—Insights into an
1208 evolving accretionary-collisional orogenic system. *Earth-Sci. Rev.*
- 1209 Grenholm, M., Jessell, M.W., Thébaud, N., 2019b. Paleoproterozoic volcano-sedimentary series in the
1210 ca. 2.27–1.96 Ga Birimian Orogen of the southeastern West African Craton. *Precambrian Res.*
- 1211 Guergouz, C., Martin, L., Vanderhaeghe, O., Thébaud, N., Fiorentini, M., 2018. Zircon and monazite
1212 petrochronologic record of prolonged amphibolite to granulite facies metamorphism in the
1213 Ivrea-Verbano and Strona-Ceneri Zones, NW Italy. *Lithos* 308–309, 1–18.
1214 <https://doi.org/10.1016/j.lithos.2018.02.014>
- 1215 Gueye, M., Ngom, P.M., Diène, M., Thiam, Y., Siegesmund, S., Wemmer, K., Pawlig, S., 2008.
1216 Intrusive rocks and tectono-metamorphic evolution of the Mako Paleoproterozoic belt
1217 (Eastern Senegal, West Africa). *J. Afr. Earth Sci., Investigations of ore deposits within the*
1218 *West African Craton and surrounding areas* 50, 88–110.
1219 <https://doi.org/10.1016/j.jafrearsci.2007.09.013>
- 1220 Hammarstrom, J.M., Zen, E.-A., 1986. Aluminum in hornblende: An empirical igneous geobarometer.
1221 *Am. Mineral.* 71, 1297–1313.
- 1222 Hasalová, P., Schulmann, K., Tabaud, A.S., Oliot, E., 2015. Microstructural evidences for
1223 mineralogical inheritance in partially molten rocks: example from the Vosges Mts. *Bull. Société Géologique Fr.* 186, 131–143. <https://doi.org/10.2113/gssgbull.186.2-3.131>
- 1224 Hermann, J., 2002. Allanite: thorium and light rare earth element carrier in subducted crust. *Chem. Geol.* 192, 289–306. [https://doi.org/10.1016/S0009-2541\(02\)00222-X](https://doi.org/10.1016/S0009-2541(02)00222-X)
- 1225 Hildreth, W., 2004. Volcanological perspectives on Long Valley, Mammoth Mountain, and Mono
1226 Craters: several contiguous but discrete systems. *J. Volcanol. Geotherm. Res.* 136, 169–198.
1227 <https://doi.org/10.1016/j.jvolgeores.2004.05.019>
- 1228 Hirdes, W., Davis, D.W., 1998. First U-Pb zircon age of extrusive volcanism in the Birimian
1229 Supergroup of Ghana/West Africa. *J. Afr. Earth Sci.* 27, 291–294.
1230 [https://doi.org/10.1016/S0899-5362\(98\)00062-1](https://doi.org/10.1016/S0899-5362(98)00062-1)
- 1231 Hirdes, W., Davis, D.W., Lüdtke, G., Konan, G., 1996. Two generations of Birimian
1232 (Paleoproterozoic) volcanic belts in northeastern Côte d'Ivoire (West Africa): consequences
1233 for the 'Birimian controversy.' *Precambrian Res.* 80, 173–191. [https://doi.org/10.1016/S0301-9268\(96\)00011-3](https://doi.org/10.1016/S0301-9268(96)00011-3)
- 1234 Hirth, G., Tullis, J., 1992. Dislocation creep regimes in quartz aggregates. *J. Struct. Geol.* 14, 145–
1235 159.
- 1236
- 1237
- 1238
- 1239
- 1240
- 1241

- 1242 Hoffmann, J.E., Münker, C., Næraa, T., Rosing, M.T., Herwartz, D., Garbe-Schönberg, D.,
1243 Svahnberg, H., 2011. Mechanisms of Archean crust formation inferred from high-precision
1244 HFSE systematics in TTGs. *Geochim. Cosmochim. Acta* 75, 4157–4178.
- 1245 Holdaway, M.J., Mukhopadhyay, B., 1993. A reevaluation of the stability relations of andalusite:
1246 Thermochemical data and phase diagram for the aluminum silicates. *Am. Mineral.* 78, 298–
1247 315.
- 1248 Holland, T., Powell, R., 2003. Activity–composition relations for phases in petrological calculations:
1249 an asymmetric multicomponent formulation. *Contrib. Mineral. Petrol.* 145, 492–501.
- 1250 Holland, T., Powell, R., 1998. An internally consistent thermodynamic data set for phases of
1251 petrological interest. *J. Metamorph. Geol.* 16, 309–343.
- 1252 Hollister, L.S., Grissom, G.C., Peters, E.K., Stowell, H.H., Sisson, V.B., 1987. Confirmation of the
1253 empirical correlation of Al in hornblende with pressure of solidification of calc-alkaline
1254 plutons. *Am. Mineral.* 72, 231–239.
- 1255 Holness, M.B., Stripp, G., Humphreys, M.C.S., Veksler, I.V., Nielsen, T.F.D., Tegner, C., 2011.
1256 Silicate Liquid Immiscibility within the Crystal Mush: Late-stage Magmatic Microstructures
1257 in the Skaergaard Intrusion, East Greenland. *J. Petrol.* 52, 175–222.
1258 <https://doi.org/10.1093/petrology/egq077>
- 1259 Hottin, G., Ouedraogo, O., 1975. Notice explicative de la carte géologique à 1: 1 000 000 de la
1260 république de Haute-Volta. BRGM.
- 1261 Ilboudo, H., Lombo, M., Wenmenga, U., Napon, S., Naba, S., Ngom, P.M., 2017a. Evidence of a
1262 Volcanogenic Massive Sulfide (ZnPbCuAg) district within the Tiébélé Birimian
1263 (Paleoproterozoic) Greenstone Belts, Southern Burkina Faso (West–Africa). *J. Afr. Earth Sci.*
1264 129, 792–813.
- 1265 Ilboudo, H., Sawadogo, S., Kagambega, N., Remmal, T., 2021. Petrology, geochemistry, and source of
1266 the emplacement model of the Paleoproterozoic Tiébélé Granite Pluton, Burkina Faso (West–
1267 Africa): contribution to mineral exploration. *Int. J. Earth Sci.* <https://doi.org/10.1007/s00531-021-02039-3>
- 1268 Ilboudo, H., Sawadogo, S., Zongo, G.H., Naba, S., Wenmenga, U., Lombo, M., 2020. Geochemistry
1269 and geodynamic constraint of volcanic and plutonic magmatism within the Banfora Belt
1270 (Burkina-Faso, West-Africa): contribution to Mineral Exploration. *Geol. Soc. Lond. Spec.*
1271 Publ. 502.
- 1272 Ilboudo, H., Wenmenga, U., Sawadogo, S., Remmal, T., 2017b. Mise en évidence d'un assemblage à
1273 disthène - staurotide - grenat dans le secteur de Mangodara, ceinture de Banfora, Burkina
1274 Faso, Afrique de l'Ouest : implication dans la genèse des gîtes minéraux polymétalliques. *Afr.*
1275 *Sci.* 13, 220–231.
- 1276 Jackson, M.D., Blundy, J., Sparks, R.S.J., 2018. Chemical differentiation, cold storage and
1277 remobilization of magma in the Earth's crust. *Nature* 564, 405–409.
1278 <https://doi.org/10.1038/s41586-018-0746-2>
- 1279 Jackson, M.D., Cheadle, M.J., Atherton, M.P., 2003. Quantitative modeling of granitic melt generation
1280 and segregation in the continental crust. *J. Geophys. Res. Solid Earth* 108.
1281 <https://doi.org/10.1029/2001JB001050>
- 1282 Johnson, M.C., Rutherford, M.J., 1989. Experimental calibration of the aluminum-in-hornblende
1283 geobarometer with application to Long Valley caldera (California) volcanic rocks. *Geology*
1284 17, 837–841. [https://doi.org/10.1130/0091-7613\(1989\)017<0837:ECOTAI>2.3.CO;2](https://doi.org/10.1130/0091-7613(1989)017<0837:ECOTAI>2.3.CO;2)
- 1285 Kelsey, D.E., Clark, C., Hand, M., 2008. Thermobarometric modelling of zircon and monazite growth
1286 in melt-bearing systems: examples using model metapelitic and metapsammitic granulites. *J.*
1287 *Metamorph. Geol.* 26, 199–212. <https://doi.org/10.1111/j.1525-1314.2007.00757.x>
- 1288 Kelsey, D.E., Powell, R., 2011. Progress in linking accessory mineral growth and breakdown to major
1289 mineral evolution in metamorphic rocks: a thermodynamic approach in the Na₂O-CaO-K₂O-
1290 FeO-MgO-Al₂O₃-SiO₂-H₂O-TiO₂-ZrO₂ system. *J. Metamorph. Geol.* 29, 151–166.
1291 <https://doi.org/10.1111/j.1525-1314.2010.00910.x>
- 1292 Kouamelan, A.N., 1996. Géochronologie et Géochimie des Formations Archéennes et Protérozoïques
1293 de la Dorsale de Man en Côte d'Ivoire. Implications pour la Transition Archéen-Protérozoïque.
- 1294

- 1295 Lambert-Smith, J.S., Lawrence, D.M., Müller, W., Treloar, P.J., 2016. Palaeotectonic setting of the
1296 south-eastern Kédougou-Kéniéba Inlier, West Africa: new insights from igneous trace element
1297 geochemistry and U-Pb zircon ages. *Precambrian Res.* 274, 110–135.
- 1298 Laurent, O., Björnsen, J., Wotzlaw, J.-F., Bretscher, S., Pimenta Silva, M., Moyen, J.-F., Ulmer, P.,
1299 Bachmann, O., 2020. Earth's earliest granitoids are crystal-rich magma reservoirs tapped by
1300 silicic eruptions. *Nat. Geosci.* 13, 163–169. <https://doi.org/10.1038/s41561-019-0520-6>
- 1301 Laurent, O., Martin, H., Moyen, J.-F., Doucelance, R., 2014. The diversity and evolution of late-
1302 Archean granitoids: Evidence for the onset of “modern-style” plate tectonics between 3.0 and
1303 2.5 Ga. *Lithos* 205, 208–235.
- 1304 Law, R.D., 2014. Deformation thermometry based on quartz c-axis fabrics and recrystallization
1305 microstructures: A review. *J. Struct. Geol.* 66, 129–161.
- 1306 Le Breton, N., Thompson, A.B., 1988. Fluid-absent (dehydration) melting of biotite in metapelites in
1307 the early stages of crustal anatexis. *Contrib. Mineral. Petrol.* 99, 226–237.
- 1308 Ledru, P., Pons, J., Milési, J.-P., Feybesse, J.-L., Johan, V., 1991. Transcurrent tectonics and
1309 polycyclic evolution in the Lower Proterozoic of Senegal-Mali. *Precambrian Res.* 50, 337–
1310 354.
- 1311 Lemoine, S., 1988. Evolution géologique de la région de Dabakala (NE de la Côte-d'Ivoire) au
1312 Protérozoïque. Possibilités d'extension au reste de la Côte-d'Ivoire et au Burkina Faso:
1313 similitudes et différences; les linéaments de Greenville-Ferkessédougou et Grand Cess-
1314 Niakaramandougou. Thèse ès Sciences, Univ. Cl.-Ferrand, France.
- 1315 Lemoine, S., Tempier, P., Bassot, J., Caen-Vachette, M., Viallette, Y., Toure, S., Wenmenga, U., 1990.
1316 The Burkinian orogenic cycle, precursor of the Eburnian orogeny in West Africa. *Geol. J.* 25,
1317 171–188.
- 1318 Liégeois, J.P., Claessens, W., Camara, D., Klerkx, J., 1991. Short-lived Eburnian orogeny in southern
1319 Mali. Geology, tectonics, U-Pb and Rb-Sr geochronology. *Precambrian Res.* 50, 111–136.
1320 [https://doi.org/10.1016/0301-9268\(91\)90050-K](https://doi.org/10.1016/0301-9268(91)90050-K)
- 1321 Linnen, R., Cuney, M., 2005. Granite-related rare-element deposits and experimental constraints on
1322 Ta-Nb-W-Sn-Zr-Hf mineralization, in Linnen RL and Samson IM, eds., rare-element
1323 geochemistry and mineral deposits.
- 1324 Liou, J., Kuniyoshi, S., Ito, K., 1974. Experimental studies of the phase relations between greenschist
1325 and amphibolite in a basaltic system. *Am. J. Sci.* 274, 613–632.
- 1326 Liou, P., Guo, J., 2019. Generation of Archaean TTG Gneisses Through Amphibole-Dominated
1327 Fractionation. *J. Geophys. Res. Solid Earth* 124, 3605–3619.
1328 <https://doi.org/10.1029/2018JB017024>
- 1329 Lompo, M., 2010. Paleoproterozoic structural evolution of the Man-Leo Shield (West Africa). Key
1330 structures for vertical to transcurrent tectonics. *J. Afr. Earth Sci.* 58, 19–36.
- 1331 Lompo, M., 2009. Geodynamic evolution of the 2.25-2.0 Ga Palaeoproterozoic magmatic rocks in the
1332 Man-Leo Shield of the West African Craton. A model of subsidence of an oceanic plateau.
1333 *Geol. Soc. Lond. Spec. Publ.* 323, 231–254.
- 1334 London, D., 2014. A petrologic assessment of internal zonation in granitic pegmatites. *Lithos* 184–
1335 187, 74–104. <https://doi.org/10.1016/j.lithos.2013.10.025>
- 1336 London, D., 2009. The origin of primary textures in granitic pegmatites. *Can. Mineral.* 47, 697–724.
- 1337 London, D., 2008. Pegmatites. *Can Miner.* 10, 347.
- 1338 London, D., 1989. Lithophile rare element concentration in silicic rocks: The alkaline trend in granitic
1339 systems. *Geol. Mineral. Assoc. Can. Program Abstr.* 14, A21.
- 1340 Lüdtke, G., Hirdes, W., Konan, G., Koné, Y., Yao, C., Diarra, S., Zamblé, Z., 1998. Géologie de la
1341 région Haute Comoé Nord—feuilles Kong (4b et 4d) et Téhini-Bouna (3a à 3d). *Dir. Géologie*
1342 *Abidj. Bull.* 178.
- 1343 Ludwig, K., 2003. User's manual for Isoplot/EX, version 3.00. Geochronological Toolkit Microsoft
1344 Excel 4, 71.
- 1345 Martin, H., Moyen, J.-F., 2002. Secular changes in tonalite-trondhjemite-granodiorite composition as
1346 markers of the progressive cooling of Earth. *Geology* 30, 319–322.
1347 [https://doi.org/10.1130/0091-7613\(2002\)030<0319:SCITTG>2.0.CO;2](https://doi.org/10.1130/0091-7613(2002)030<0319:SCITTG>2.0.CO;2)

- 1348 Martin, R.F., De Vito, C., 2005. The patterns of enrichment in felsic pegmatites ultimately depend on
1349 tectonic setting. *Can. Mineral.* 43, 2027–2048. <https://doi.org/10.2113/gscanmin.43.6.2027>
- 1350 Martini, A., Bitencourt, M. de F., Weinberg, R.F., De Toni, G.B., Lauro, V.S.N., 2019. From
1351 migmatite to magma - crustal melting and generation of granite in the Camboriú Complex,
1352 south Brazil. *Lithos* 340–341, 270–286. <https://doi.org/10.1016/j.lithos.2019.05.017>
- 1353 Maruyama, S., Suzuki, K., Liou, J.G., 1983. Greenschist–amphibolite transition equilibria at low
1354 pressures. *J. Petrol.* 24, 583–604.
- 1355 Masurel, Q., Eglinger, A., Thébaud, N., Allibone, A., André-Mayer, A.-S., McFarlane, H., Miller, J.,
1356 Jessell, M., Aillères, L., Vanderhaeghe, O., Salvi, S., Baratoux, L., Perrouty, S., Begg, G.,
1357 Fougerouse, D., Hayman, P., Wane, O., Tshibubudze, A., Parra-Avila, L., Kouamélan, A.,
1358 Ampsonah, P.O., 2021. Paleoproterozoic gold events in the southern West African Craton:
1359 review and synopsis. *Miner. Deposita*. <https://doi.org/10.1007/s00126-021-01052-5>
- 1360 McDonough, W.F., Sun, S.-S., 1995. The composition of the Earth. *Chem. Geol.* 120, 223–253.
- 1361 McFarlane, C.R.M., Mavrogenes, J., Lentz, D., King, K., Allibone, A., Holcombe, R., 2011. Geology
1362 and Intrusion-Related Affinity of the Morila Gold Mine, Southeast Mali. *Econ. Geol.* 106,
1363 727–750. <https://doi.org/10.2113/econgeo.106.5.727>
- 1364 Mehnert, K.R., 1968. Migmatites and the origin of granitic rocks. *Megascopic Struct. Migmatite* 7–42.
- 1365 Mériaud, N., Thébaud, N., Masurel, Q., Hayman, P., Jessell, M.W., Kemp, A., Evans, N.J., Fisher,
1366 C.M., Scott, P.M., 2020. Lithostratigraphic evolution of the Bandamian Volcanic Cycle in
1367 central Côte d'Ivoire: Insights into the late Eburnean magmatic resurgence and its geodynamic
1368 implications. *Precambrian Res.* 105847. <https://doi.org/10.1016/j.precamres.2020.105847>
- 1369 Metelka, V., Baratoux, L., Naba, S., Jessell, M.W., 2011. A geophysically constrained litho-structural
1370 analysis of the Eburnean greenstone belts and associated granitoid domains, Burkina Faso,
1371 West Africa. *Precambrian Res.* 190, 48–69. <https://doi.org/10.1016/j.precamres.2011.08.002>
- 1372 Milési, J., 1989. West African gold deposits in their Lower Proterozoic lithostructural setting. *Chron.
1373 Rech. Minière* 3–98.
- 1374 Milési, J.-P., Feybesse, J.-L., Pinna, P., Deschamps, Y., Kampunzu, H., Muhongo, S., Lescuyer, J.-L.,
1375 Le Goff, E., Delor, C., Billa, M., 2004. Geological map of Africa 1: 10,000,000, SIGAfrique
1376 project. Presented at the 20th Conference of African Geology, BRGM, Orléans, France, pp. 2–
1377 7.
- 1378 Montel, J.-M., Vielzeuf, D., 1997. Partial melting of metagreywackes, Part II. Compositions of
1379 minerals and melts. *Contrib. Mineral. Petrol.* 128, 176–196.
- 1380 Moody, J.B., Meyer, D., Jenkins, J.E., 1983. Experimental characterization of the
1381 greenschist/amphibolite boundary in mafic systems. *Am. J. Sci.* 283, 48–92.
1382 <https://doi.org/10.2475/ajs.283.1.48>
- 1383 Moyen, J.-F., 2011. The composite Archaean grey gneisses: Petrological significance, and evidence
1384 for a non-unique tectonic setting for Archaean crustal growth. *Lithos*, Secular variations in
1385 magmatism and tectonic implications 123, 21–36. <https://doi.org/10.1016/j.lithos.2010.09.015>
- 1386 Moyen, J.-F., Champion, D., Smithies, R., 2009. The geochemistry of Archaean plagioclase-rich
1387 granites as a marker of source enrichment and depth of melting. *Earth Environ. Sci. Trans. R.
1388 Soc. Edinb.* 100, 35–50.
- 1389 Moyen, J.-F., Stevens, G., 2006. Experimental constraints on TTG petrogenesis: implications for
1390 Archean geodynamics. *Geophys. Monogr.-Am. Geophys. Union* 164, 149.
- 1391 Müller, A., Romer, R.L., Pedersen, R.-B., 2017. The Sveconorwegian pegmatite province—thousands
1392 of pegmatites without parental granites. *Can. Mineral.* 55, 283–315.
- 1393 Mutch, E.J.F., Blundy, J.D., Tattitch, B.C., Cooper, F.J., Brooker, R.A., 2016. An experimental study
1394 of amphibole stability in low-pressure granitic magmas and a revised Al-in-hornblende
1395 geobarometer. *Contrib. Mineral. Petrol.* 171. <https://doi.org/10.1007/s00410-016-1298-9>
- 1396 Ndiaye, P.M., Dia, A., Vialette, Y., Diallo, D., Ngom, P., Sylla, M., Wade, S., Dioh, E., 1997.
1397 Données pétrographiques, géochimiques et géochronologiques nouvelles sur les granitoïdes du
1398 Paléoprotérozoïque du Supergroupe de Dialé-Daléma (Sen; égal Oriental): Implications
1399 pétrogénétiques et géodynamiques. *J. Afr. Earth Sci.* 25, 193–208.

- 1400 Nesbitt, H.W., Young, G.M., 1984. Prediction of some weathering trends of plutonic and volcanic
1401 rocks based on thermodynamic and kinetic considerations. *Geochim. Cosmochim. Acta* 48,
1402 1523–1534.
- 1403 Nesbitt, H.W., Young, G.M., 1982. Early Proterozoic climates and plate motions inferred from major
1404 element chemistry of lutites. *Nature* 299, 715–717.
- 1405 Nude, P., Hanson, J., Dampare, S., Akiti, T., OsAE, S., Nyarko, E., Zkaria, N., Enti-Brown, S., 2011.
1406 Geochemistry of Pegmatites associated with the cape coast granite complex in the Egyaa and
1407 Akim Oda areas of southern Ghana. *Ghana J. Sci.* 51, 89–100.
- 1408 Palin, R.M., White, R.W., Green, E.C.R., 2016. Partial melting of metabasic rocks and the generation
1409 of tonalitic–trondhjemite–granodioritic (TTG) crust in the Archaean: Constraints from phase
1410 equilibrium modelling. *Precambrian Res.* 287, 73–90.
1411 <https://doi.org/10.1016/j.precamres.2016.11.001>
- 1412 Parra-Avila, L.A., Baratoux, L., Eglinger, A., Fiorentini, M.L., Block, S., 2019. The Eburnean
1413 magmatic evolution across the Baoulé-Mossi domain: Geodynamic implications for the West
1414 African Craton. *Precambrian Res.* 332, 105392.
1415 <https://doi.org/10.1016/j.precamres.2019.105392>
- 1416 Parra-Avila, L.A., Kemp, A.I.S., Fiorentini, M.L., Belousova, E.A., Baratoux, L., Block, S., Jessell,
1417 M.W., Bruguier, O., Begg, G.C., Miller, J., Davis, J., McCuaig, T.C., 2017. The
1418 geochronological evolution of the Paleoproterozoic Baoulé-Mossi domain of the Southern
1419 West African Craton. *Precambrian Res.* 300, 1–27.
1420 <https://doi.org/10.1016/j.precamres.2017.07.036>
- 1421 Passchier, C.W., Trouw, R., 2005. Deformation mechanisms. *Microtectonics* 25–66.
- 1422 Patiño Douce, A.E., 1999. What do experiments tell us about the relative contributions of crust and
1423 mantle to the origin of granitic magmas? *Geol. Soc. Lond. Spec. Publ.* 168, 55–75.
1424 <https://doi.org/10.1144/GSL.SP.1999.168.01.05>
- 1425 Patiño Douce, A.E., Beard, J.S., 1995. Dehydration-melting of Biotite Gneiss and Quartz Amphibolite
1426 from 3 to 15 kbar. *J. Petrol.* 36, 707–738. <https://doi.org/10.1093/petrology/36.3.707>
- 1427 Pattison, D.R., Spear, F.S., 2018. Kinetic control of staurolite–Al₂SiO₅ mineral assemblages:
1428 Implications for Barrovian and Buchan metamorphism. *J. Metamorph. Geol.* 36, 667–690.
- 1429 Pattison, D.R.M., 1992. Stability of Andalusite and Sillimanite and the Al₂SiO₅ Triple Point:
1430 Constraints from the Ballachulish Aureole, Scotland. *J. Geol.* 100, 423–446.
1431 <https://doi.org/10.1086/629596>
- 1432 Pawlig, S., Gueye, M., Klischies, R., Schwarz, S., Wemmer, K., Siegesmund, S., 2006. Geochemical
1433 and Sr-Nd isotopic data on the Birimian of the Kedougou-Kenieba inlier (Eastern Senegal):
1434 Implications on the Palaeoproterozoic evolution of the West African craton. *South Afr. J.*
1435 *Geol.* 109, 411–427.
- 1436 Peacock, S.M., Rushmer, T., Thompson, A.B., 1994. Partial melting of subducting oceanic crust. *Earth*
1437 *Planet. Sci. Lett.* 121, 227–244. [https://doi.org/10.1016/0012-821X\(94\)90042-6](https://doi.org/10.1016/0012-821X(94)90042-6)
- 1438 Peccerillo, A., Taylor, S., 1976. Geochemistry of Eocene calc-alkaline volcanic rocks from the
1439 Kastamonu area, northern Turkey. *Contrib. Mineral. Petrol.* 58, 63–81.
- 1440 Perrouyt, S., Aillères, L., Jessell, M.W., Baratoux, L., Bourassa, Y., Crawford, B., 2012. Revised
1441 Eburnean geodynamic evolution of the gold-rich southern Ashanti Belt, Ghana, with new field
1442 and geophysical evidence of pre-Tarkwaian deformations. *Precambrian Res.* 204, 12–39.
- 1443 Petersson, A., Scherstén, A., Kemp, A., Bara, K., Per, K., Solomon, A., 2016. Zircon U-Pb-Hf
1444 evidence for subduction related crustal growth and reworking of Archaean crust within the
1445 Palaeoproterozoic Birimian terrane, West African Craton, SE Ghana. *Precambrian Res.* 275,
1446 286–309. <http://dx.doi.org/10.1016/j.precamres.2016.01.006>
- 1447 Petford, N., Atherton, M., 1996. Na-rich partial melts from newly underplated basaltic crust: the
1448 Cordillera Blanca Batholith, Peru. *J. Petrol.* 37, 1491–1521.
- 1449 Pons, J., Barbey, P., Dupuis, D., Léger, J., 1995. Mechanisms of pluton emplacement and structural
1450 evolution of a 2.1 Ga juvenile continental crust: the Birimian of southwestern Niger.
1451 *Precambrian Res.* 70, 281–301.

- 1452 Pouclet, A., Vidal, M., Delor, C., Simeon, Y., Alric, G., 1996. Le volcanisme birimien du nord-est de
 1453 la Côte-d'Ivoire, mise en évidence de deux phases volcano-tectoniques distinctes dans
 1454 l'évolution géodynamique du Paléoprotérozoïque. *Bull. Société Géologique Fr.* 167, 529–541.
- 1455 Rapp, R.P., Watson, E.B., 1995. Dehydration melting of metabasalt at 8–32 kbar: implications for
 1456 continental growth and crust-mantle recycling. *J. Petrol.* 36, 891–931.
- 1457 Rapp, R.P., Watson, E.B., Miller, C.F., 1991. Partial melting of amphibolite/eclogite and the origin of
 1458 Archean trondhjemites and tonalites. *Precambrian Res.* 51, 1–25.
- 1459 Reichardt, H., Weinberg, R.F., 2012. Hornblende Chemistry in Meta- and Diatexesites and its Retention
 1460 in the Source of Leucogranites: an Example from the Karakoram Shear Zone, NW India. *J.
 1461 Petrol.* 53, 1287–1318. <https://doi.org/10.1093/petrology/egs017>
- 1462 Robin, P.-Y.F., 1979. Theory of metamorphic segregation and related processes. *Geochim.
 1463 Cosmochim. Acta* 43, 1587–1600. [https://doi.org/10.1016/0016-7037\(79\)90179-0](https://doi.org/10.1016/0016-7037(79)90179-0)
- 1464 Roda-Robles, E., Vieira, R., Lima, A., Pesquera, A., Noronha, F., Fontan, F., 2007. The Fregeneda–
 1465 Almendra pegmatitic field (Spain & Portugal): mineral assemblages and regional zonation.
 1466 Presented at the Granitic Pegmatites: The State of the Art–International Symposium, Porto,
 1467 Portugal, submitted.
- 1468 Roddaz, M., Debat, P., Nikiéma, S., 2007. Geochemistry of Upper Birimian sediments (major and
 1469 trace elements and Nd–Sr isotopes) and implications for weathering and tectonic setting of the
 1470 Late Paleoproterozoic crust. *Precambrian Res.* 159, 197–211.
 1471 <https://doi.org/10.1016/j.precamres.2007.06.008>
- 1472 Rudnick, R.L., Gao, S., 2003. Composition of the continental crust. *Treatise Geochem.* 3, 659.
- 1473 Rushmer, T., 1991. Partial melting of two amphibolites: contrasting experimental results under fluid-
 1474 absent conditions. *Contrib. Mineral. Petrol.* 107, 41–59.
- 1475 Saha-Fouotsa, A.N., Vanderhaeghe, O., Barbey, P., Eglinger, A., Tchameni, R., Zeh, A., Tchunte,
 1476 P.F., Nomo, E.N., 2019. The geologic record of the exhumed root of the Central African
 1477 Orogenic Belt in the central Cameroon domain (Mbé – Sassa-Mbersi region). *J. Afr. Earth Sci.*
 1478 151, 286–314. <https://doi.org/10.1016/j.jafrearsci.2018.12.008>
- 1479 Sakyi, P.A., Addae, R.A., Su, B.-X., Dampare, S.B., Abitty, E., Su, B.-C., Liu, B., Asiedu, D.K., 2020.
 1480 Petrology and geochemistry of TTG and K-rich Paleoproterozoic Birimian granitoids of the
 1481 West African Craton (Ghana): Petrogenesis and tectonic implications. *Precambrian Res.* 336,
 1482 105492. <https://doi.org/10.1016/j.precamres.2019.105492>
- 1483 Sakyi, P.A., Su, B.-X., Anum, S., Kwayisi, D., Dampare, S.B., Anani, C.Y., Nude, P.M., 2014. New
 1484 zircon U–Pb ages for erratic emplacement of 2213–2130 Ma Paleoproterozoic calc-alkaline I-
 1485 type granitoid rocks in the Lawra Volcanic Belt of Northwestern Ghana, West Africa.
 1486 *Precambrian Res.* 254, 149–168. <https://doi.org/10.1016/j.precamres.2014.08.009>
- 1487 Sawyer, E.W., 2010. Migmatites formed by water-fluxed partial melting of a leucogranodiorite
 1488 protolith: microstructures in the residual rocks and source of the fluid. *Lithos* 116, 273–286.
- 1489 Sawyer, E.W., 2001. Melt segregation in the continental crust: distribution and movement of melt in
 1490 anatetic rocks. *J. Metamorph. Geol.* 19, 291–309. [https://doi.org/10.1046/j.0263-4929.2000.00312.x](https://doi.org/10.1046/j.0263-

 1491 4929.2000.00312.x)
- 1492 Sawyer, E.W., 1999. Criteria for the recognition of partial melting. *Phys. Chem. Earth Part Solid Earth
 1493 Geod.* 24, 269–279.
- 1494 Sawyer, E.W., 1991. Disequilibrium Melting and the Rate of Melt–Residuum Separation During
 1495 Migmatization of Mafic Rocks from the Grenville Front, Quebec. *J. Petrol.* 32, 701–738.
 1496 <https://doi.org/10.1093/petrology/32.4.701>
- 1497 Schmidt, M.W., 1992. Amphibole composition in tonalite as a function of pressure: an experimental
 1498 calibration of the Al-in-hornblende barometer. *Contrib. Mineral. Petrol.* 110, 304–310.
 1499 <https://doi.org/10.1007/BF00310745>
- 1500 Schmidt, M.W., Poli, S., 2004. Magmatic epidote. *Rev. Mineral. Geochem.* 56, 399–430.
- 1501 Schmidt, M.W., Thompson, A.B., 1996. Epidote in calc-alkaline magmas; an experimental study of
 1502 stability, phase relationships, and the role of epidote in magmatic evolution. *Am. Mineral.* 81,
 1503 462–474.
- 1504 Schulmann, K., Edel, J.-B., Hasalová, P., Cosgrove, J., Ježek, J., Lexa, O., 2009. Influence of melt
 1505 induced mechanical anisotropy on the magnetic fabrics and rheology of deforming

- 1506 migmatites, Central Vosges, France. *J. Struct. Geol.* 31, 1223–1237.
1507 <https://doi.org/10.1016/j.jsg.2009.07.004>
- 1508 Schumacher, J., 1997. The estimation of the proportion of ferric iron in the electron-microprobe
1509 analysis of amphiboles. *Can Miner.* 35, 238–246.
- 1510 Schwindinger, M., Weinberg, R.F., 2017. A felsic MASH zone of crustal magmas — Feedback
1511 between granite magma intrusion and in situ crustal anatexis. *Lithos* 284–285, 109–121.
1512 <https://doi.org/10.1016/j.lithos.2017.03.030>
- 1513 Schwindinger, M., Weinberg, R.F., Clos, F., 2019. Wet or dry? The difficulty of identifying the
1514 presence of water during crustal melting. *J. Metamorph. Geol.* 37, 339–358.
- 1515 Shand, S.J., 1943. Eruptive rocks: their genesis, composition, and classification, with a chapter on
1516 meteorites. *J. Wiley & sons, Incorporated.*
- 1517 Shaw, D.M., 1968. A review of K-Rb fractionation trends by covariance analysis. *Geochim. Cosmochim. Acta* 32, 573–601. [https://doi.org/10.1016/0016-7037\(68\)90050-1](https://doi.org/10.1016/0016-7037(68)90050-1)
- 1518 Shaw, R.A., Goodenough, K.M., Roberts, N.M.W., Horstwood, M.S.A., Chillery, S.R., Gunn, A.G.,
1519 2016. Petrogenesis of rare-metal pegmatites in high-grade metamorphic terranes: A case study
1520 from the Lewisian Gneiss Complex of north-west Scotland. *Precambrian Res.* 281, 338–362.
1521 <https://doi.org/10.1016/j.precamres.2016.06.008>
- 1522 Skjerlie, K.P., Patiño Douce, A.E., 2002. The Fluid-absent Partial Melting of a Zoisite-bearing Quartz
1523 Eclogite from 1.0 to 3.2 GPa; Implications for Melting in Thickened Continental Crust and
1524 for Subduction-zone Processes. *J. Petrol.* 43, 291–314.
1525 <https://doi.org/10.1093/petrology/43.2.291>
- 1526 Solgadi, F., Moyen, J.-F., Vanderhaeghe, O., Sawyer, E.W., Reisberg, L., 2007. The role of crustal
1527 anatexis and mantle-derived magmas in the genesis of synorogenic Hercynian granites of the
1528 Livradois area, French Massif Central. *Can. Mineral.* 45, 581–606.
1529 <https://doi.org/10.2113/gscanmin.45.3.581>
- 1530 Soumaila, A., Henry, P., Garba, Z., Rossi, M., 2008. REE patterns, Nd-Sm and U-Pb ages of the
1531 metamorphic rocks of the Diagorou-Darbani greenstone belt (Liptako, SW Niger): implication
1532 for Birimian (Palaeoproterozoic) crustal genesis. *Geol. Soc. Lond. Spec. Publ.* 297, 19–32.
1533 <https://doi.org/10.1144/SP297.2>
- 1534 Spear, F.S., Kohn, M.J., Cheney, J.T., 1999. P-T paths from anatetic pelites. *Contrib. Mineral. Petrol.*
1535 134, 17–32. <https://doi.org/10.1007/s004100050466>
- 1536 Stevenson, D.J., 1989. Spontaneous small-scale melt segregation in partial melts undergoing
1537 deformation. *Geophys. Res. Lett.* 16, 1067–1070. <https://doi.org/10.1029/GL016i009p01067>
- 1538 Streckeisen, A., Le Maitre, R., 1979. A chemical approximation to the modal QAPF classification of
1539 igneous rocks.
- 1540 Sun, S.-S., McDonough, W.F., 1989. Chemical and isotopic systematics of oceanic basalts:
1541 implications for mantle composition and processes. *Geol. Soc. Lond. Spec. Publ.* 42, 313–345.
- 1542 Tafur, L.A., Diener, J.F.A., 2020. Mineral equilibrium constraints on the feasibility of diffusive H₂O-
1543 fluxed melting in the continental crust. *J. Metamorph. Geol.* 38, 719–742.
1544 <https://doi.org/10.1111/jmg.12536>
- 1545 Tagini, B., 1971. Esquisse structurale de la Côte d'Ivoire. Essai de géotectonique régionale. These
1546 Univ Lausanne Soc. Etat Pour Dev. Min. Cote Ivoire.
- 1547 Tapsoba, B., Lo, C.-H., Jahn, B.-M., Chung, S.-L., Wenmenga, U., Iizuka, Y., 2013. Chemical and Sr-
1548 Nd isotopic compositions and zircon U-Pb ages of the Birimian granitoids from NE Burkina
1549 Faso, West African Craton: Implications on the geodynamic setting and crustal evolution.
1550 *Precambrian Res.* 224, 364–396. <https://doi.org/10.1016/j.precamres.2012.09.013>
- 1551 Tassinari, C.C., Macambira, M.J., 1999. Geochronological provinces of the Amazonian Craton.
1552 *Episodes-Newsmag. Int. Union Geol. Sci.* 22, 174–182.
- 1553 Taylor, S., 1965. The application of trace element data to problems in petrology. *Phys. Chem. Earth* 6,
1554 133–213.
- 1555 Tera, F., Wasserburg, G.J., 1972. U-Th-Pb systematics in lunar highland samples from the Luna 20
1556 and Apollo 16 missions. *Earth Planet. Sci. Lett.* 17, 36–51. [https://doi.org/10.1016/0012-821X\(72\)90257-9](https://doi.org/10.1016/0012-821X(72)90257-9)

- 1559 Thomas, W., Ernst, W., 1990. The aluminium content of hornblende in calc-alkaline granitic rocks: A
 1560 mineralogic barometer calibrated experimentally to 12 kbars. *Fluid-Miner. Interact.* Tribute
 1561 HP Eugster 59–63.
- 1562 Thompson, A.B., 1982. Dehydration melting of pelitic rocks and the generation of H₂O-
 1563 undersaturated granitic liquids. *Am. J. Sci.* 282, 1567–1595.
- 1564 Tiepolo, M., Oberti, R., Vannucci, R., 2002. Trace-element incorporation in titanite: constraints from
 1565 experimentally determined solid/liquid partition coefficients. *Chem. Geol.* 191, 105–119.
- 1566 Tinkham, D.K., Zuluaga, C.A., Stowell, H.H., 2001. Metapelite phase equilibria modeling in
 1567 MnNCKFMASH: the effect of variable Al₂O₃ and MgO/(MgO+ FeO) on mineral stability.
 1568 *Geol. Mater. Res.* 3, 1–42.
- 1569 Touret, J.L.R., Hartel, T.H.D., 1990. Synmetamorphic Fluid Inclusions in Granulites, in: Vielzeuf, D.,
 1570 Vidal, Ph. (Eds.), *Granulites and Crustal Evolution*, NATO ASI Series. Springer Netherlands,
 1571 Dordrecht, pp. 397–417. https://doi.org/10.1007/978-94-009-2055-2_20
- 1572 Touret, J.L.R., Huizenga, J.-M., 2011. Fluids in granulites. *Geol. Soc. Am. Mem.* 207, 25–37.
- 1573 Touret, J.L.R., Nijland, T.G., 2013. Prograde, Peak and Retrograde Metamorphic Fluids and
 1574 Associated Metasomatism in Upper Amphibolite to Granulite Facies Transition Zones.
 1575 *Metasomatism Chem. Transform. Rock* 415–469. https://doi.org/10.1007/978-3-642-28394-9_11
- 1577 Tshibubudze, A., Hein, K.A.A., 2013. Structural setting of gold deposits in the Oudalan-Gorouol
 1578 volcano-sedimentary belt east of the Markoye Shear Zone, West African craton. *J. Afr. Earth
 1579 Sci.* 80, 31–47.
- 1580 Tshibubudze, A., Hein, K.A.A., McCuaig, T.C., 2015. The relative and absolute chronology of strato-
 1581 tectonic events in the Gorom-Gorom granitoid terrane and Oudalan-Gorouol belt, northeast
 1582 Burkina Faso. *J. Afr. Earth Sci.* 112, 382–418.
- 1583 Tshibubudze, A., Hein, K.A.A., Peters, L., Woolfe, A., McCuaig, T., 2013. Oldest U-Pb crystallisation
 1584 age for the West African Craton From the Oudalan-Gorouol Belt of Burkina Faso. *South Afr.
 1585 J. Geol.* 116, 169–181.
- 1586 Turlin, F., Deruy, C., Eglinger, A., Vanderhaeghe, O., André-Mayer, A.-S., Poujol, M., Moukhsil, A.,
 1587 Solgadi, F., 2018. A 70 Ma record of suprasolidus conditions in the large, hot, long-duration
 1588 Grenville Orogen. *Terra Nova* 30, 233–243.
- 1589 Van der Molen, I., 1985. Interlayer material transport during layer-normal shortening. Part II.
 1590 Boudinage, pinch-and-swell and migmatite at Søndre Strømfjord Airport, West Greenland.
 1591 *Tectonophysics* 115, 297–313. [https://doi.org/10.1016/0040-1951\(85\)90143-X](https://doi.org/10.1016/0040-1951(85)90143-X)
- 1592 Van der Molen, I., Paterson, M., 1979. Experimental deformation of partially-melted granite. *Contrib.
 1593 Mineral. Petrol.* 70, 299–318.
- 1594 Vanderhaeghe, O., 2009. Migmatites, granites and orogeny: Flow modes of partially-molten rocks and
 1595 magmas associated with melt/solid segregation in orogenic belts. *Tectonophysics, Hot orogens*
 1596 477, 119–134. <https://doi.org/10.1016/j.tecto.2009.06.021>
- 1597 Vanderhaeghe, O., 2001. Melt segregation, pervasive melt migration and magma mobility in the
 1598 continental crust: the structural record from pores to orogens. *Phys. Chem. Earth Part Solid
 1599 Earth Geod.* 26, 213–223.
- 1600 Vanderhaeghe, O., Guergouz, C., Fabre, C., Duchêne, S., Baratoux, D., 2019. Secular cooling and
 1601 crystallization of partially molten Archaean continental crust over 1 Ga. *Comptes Rendus
 1602 Geosci., New aspects of magma storage and transfer* 351, 562–573.
 1603 <https://doi.org/10.1016/j.crte.2019.07.002>
- 1604 Vanderhaeghe, O., Ledru, P., Thiéblemont, D., Egal, E., Cocherie, A., Tegyey, M., Milési, J.-P., 1998.
 1605 Contrasting mechanism of crustal growth: Geodynamic evolution of the Paleoproterozoic
 1606 granite-greenstone belts of French Guiana. *Precambrian Res.* 92, 165–193.
 1607 [https://doi.org/10.1016/S0301-9268\(98\)00074-6](https://doi.org/10.1016/S0301-9268(98)00074-6)
- 1608 Vanderhaeghe, O., Teyssier, C., Wysoczanski, R., 1999. Structural and geochronological constraints
 1609 on the role of partial melting during the formation of the Shuswap metamorphic core complex
 1610 at the latitude of the Thor-Odin dome, British Columbia. *Can. J. Earth Sci.* 36, 917–943.
- 1611 Vauchez, A., Hollanda, M.H.B.M., Monié, P., Mondou, M., Egydio-Silva, M., 2019. Slow cooling and
 1612 crystallization of the roots of the Neoproterozoic Araçuaí hot orogen (SE Brazil): Implications

- 1613 for rheology, strain distribution, and deformation analysis. *Tectonophysics* 766, 500–518.
1614 <https://doi.org/10.1016/j.tecto.2019.05.013>
- 1615 Vidal, M., Alric, G., 1994. The Palaeoproterozoic (Birimian) of Haute-Comoé in the West African
1616 craton, Ivory Coast: a transtensional back-arc basin. *Precambrian Res.* 65, 207–229.
- 1617 Vidal, M., Delor, C., Pouclet, A., Simeon, Y., Alric, G., 1996. Evolution géodynamique de l'Afrique
1618 de l'Ouest entre 2, 2 Ga et 2 Ga; le style "archéen" des ceintures vertes et des ensembles
1619 sédimentaires birimiens du nord-est de la Côte-d'Ivoire. *Bull. Société Géologique Fr.* 167,
1620 307–319.
- 1621 Vidal, M., Gumiaux, C., Cagnard, F., Pouclet, A., Ouattara, G., Pichon, M., 2009. Evolution of a
1622 Paleoproterozoic "weak type" orogeny in the West African Craton (Ivory Coast).
1623 *Tectonophysics* 477, 145–159.
- 1624 Vielzeuf, D., Holloway, J.R., 1988. Experimental determination of the fluid-absent melting relations in
1625 the pelitic system. *Contrib. Mineral. Petrol.* 98, 257–276.
- 1626 Vielzeuf, D., Montel, J.-M., 1994. Partial melting of metagreywackes. Part I. Fluid-absent experiments
1627 and phase relationships. *Contrib. Mineral. Petrol.* 117, 375–393.
1628 <https://doi.org/10.1007/BF00307272>
- 1629 Wane, O., Liégeois, J.-P., Thébaud, N., Miller, J., Metelka, V., Jessell, M.W., 2018. The onset of the
1630 Eburnean collision with the Kenema-Man craton evidenced by plutonic and
1631 volcanosedimentary rock record of the Masssigui region, southern Mali. *Precambrian Res.*
1632 305, 444–478. <https://doi.org/10.1016/j.precamres.2017.11.008>
- 1633 Weinberg, R.F., 2006. Melt segregation structures in granitic plutons. *Geology* 34, 305–308.
1634 <https://doi.org/10.1130/G22406.1>
- 1635 Weinberg, R.F., 1999. Mesoscale pervasive felsic magma migration: alternatives to dyking. *Lithos* 46,
1636 393–410.
- 1637 Weinberg, R.F., Hasalová, P., 2015. Water-fluxed melting of the continental crust: A review. *Lithos*
1638 212, 158–188.
- 1639 Weinberg, R.F., Hasalová, P., Ward, L., Fanning, C.M., 2013. Interaction between deformation and
1640 magma extraction in migmatites: Examples from Kangaroo Island, South Australia. *GSA Bull.*
1641 125, 1282–1300. <https://doi.org/10.1130/B30781.1>
- 1642 Weinberg, R.F., Sial, A.N., Mariano, G., 2004. Close spatial relationship between plutons and shear
1643 zones. *Geology* 32, 377–380. <https://doi.org/10.1130/G20290.1>
- 1644 Whalen, J.B., Currie, K.L., Chappell, B.W., 1987. A-type granites: geochemical characteristics,
1645 discrimination and petrogenesis. *Contrib. Mineral. Petrol.* 95, 407–419.
- 1646 White, R., Powell, R., Clarke, G., 2003. Prograde Metamorphic Assemblage Evolution during Partial
1647 Melting of Metasedimentary Rocks at Low Pressures: Migmatites from Mt Stafford, Central
1648 Australia. *J. Petrol.* 44, 1937–1960.
- 1649 White, R., Powell, R., Holland, T., 2007. Progress relating to calculation of partial melting equilibria
1650 for metapelites. *J. Metamorph. Geol.* 25, 511–527.
- 1651 White, R.W., Powell, R., Clarke, G.L., 2002. The interpretation of reaction textures in Fe-rich
1652 metapelitic granulites of the Musgrave Block, central Australia: constraints from mineral
1653 equilibria calculations in the system K₂O–FeO–MgO–Al₂O₃–SiO₂–H₂O–TiO₂–Fe₂O₃. *J.*
1654 *Metamorph. Geol.* 20, 41–55. <https://doi.org/10.1046/j.0263-4929.2001.00349.x>
- 1655 Whitney, D.L., 2002. Coexisting andalusite, kyanite, and sillimanite: Sequential formation of three
1656 Al₂SiO₅ polymorphs during progressive metamorphism near the triple point, Sivrihisar,
1657 Turkey. *Am. Mineral.* 87, 405–416. <https://doi.org/10.2138/am-2002-0404>
- 1658 Wickham, S.M., 1987. The segregation and emplacement of granitic magmas. *J. Geol. Soc.* 144, 281–
1659 297. <https://doi.org/10.1144/gsjgs.144.2.0281>
- 1660 Winther, K., Newton, R., 1991. Experimental melting of hydrous low-K tholeiite: evidence on the
1661 origin of Archaean cratons: *Geological Society of Denmark Bulletin*, v. 39.
- 1662 Wolf, M.B., Wyllie, P.J., 1994. Dehydration-melting of amphibolite at 10 kbar: the effects of
1663 temperature and time. *Contrib. Mineral. Petrol.* 115, 369–383.
- 1664 Wyllie, P.J., Wolf, M.B., 1993. Amphibolite dehydration-melting: sorting out the solidus. *Geol. Soc.*
1665 *Lond. Spec. Publ.* 76, 405–416.

1666 Yakymchuk, C., Brown, M., 2014. Behaviour of zircon and monazite during crustal melting. *J. Geol.*
1667 *Soc.* 171, 465–479. <https://doi.org/10.1144/jgs2013-115>
1668 Závada, P., Schulmann, K., Racek, M., Hasalová, P., Jeřábek, P., Weinberg, R.F., Štípská, P., Roberts,
1669 A., 2018. Role of strain localization and melt flow on exhumation of deeply subducted
1670 continental crust. *Lithosphere* 10, 217–238. <https://doi.org/10.1130/L666.1>
1671

1672 **Figures captions**

1673 (2 columns)

1674 *Fig. 1. Geological map of the West African Craton, modified after Milési et al. (2004), and Block et al.*
1675 *(2015). Abbreviations: SGGC = Sidéradoougou Gneiss-Granitoid Complex, Si = Sidéradoougou gneiss-*
1676 *granitoid complex. Ba = Banfora greenstone belt, Di = Diebougou gneiss-granitoid complex, Ho=*
1677 *Hounde greenstone belt, KT= Koudougou-Tumu gneiss-granitoid complex, OFSZ = Ouango-Fitini*
1678 *shear zone. The red rectangle indicates the studied zone.*

1679

1680 (2 columns)

1681 *Fig. 2. Lithostructural map of the Mangodara district; the south-east part of the map is reinterpreted*
1682 *from data of Hirdes et al. (1996). Lithofabrics are delineated from interpretation of fabrics measured*
1683 *on the field, aerial photographs (Google Earth) and remote sensing imagery (LANDSAT-8, Sentinel-*
1684 *2). Magnetic lineaments are extracted from aeromagnetic data (SYSMIN), and served for*
1685 *interpretation of shear zones, using the method proposed by (Chardon et al., 2020). Emplacement of*
1686 *named samples in this paper are indicated in the map. Markers used in chemical element diagrams*
1687 *are presented in the legend next to their related lithology. Supplementary U-Pb ages in the south-east*
1688 *part of the map are extracted from Hirdes et al. (1996).*

1689

1690 (2 columns)

1691 *Fig. 3. Field photographs of granodioritic gneiss and associated migmatites. (a) Banded layer in a*
1692 *granodioritic gneiss. (b) Granodioritic gneiss showing augen texture. (c) Gabbroic and microgranular*

1693 *enclaves in a granodioritic gneiss. (d) Layered granodioritic gneiss containing leucosomes connected*
1694 *to garnet-REE pegmatite dyke (station BB24, See also Fig. 11). (e) Ptygmatitic veins in a*
1695 *granodioritic gneiss (east of Gountiedougou). (f) Enclave of granodioritic gneiss in the tonalitic-*
1696 *trondhjemitic gneiss. Leucosomes and titanite-allanite pegmatite are visible (station BMN37).*

1697

1698 (2 columns)

1699 *Fig. 4. (a) Granolepidoblastic texture in the granodioritic gneiss (station BMN24). The foliation is*
1700 *marked by alignment of biotite laths. Eye-shaped plagioclase and hornblende are surrounded by*
1701 *biotite and mark the granoblastic texture. (b) Mafic hornblende-biotite-epidote assemblage, stretched*
1702 *in an S-C fabric. Recrystallized quartz is located in the margin of the ferromagnesian minerals, and*
1703 *distributed with preferential orientation along the C direction. Clastic plagioclase and recrystallized*
1704 *quartz suggest solid-state deformation, under high temperature. Abbreviations: Ap = apatite, Aln =*
1705 *allanite, Bt = biotite, Ep = epidote, Hbl = hornblende, Pg = plagioclase, Ttn = titanite.*

1706

1707 (2 columns)

1708 *Fig. 5. Field photographs and optical photomicrographs of amphibolite and schist. (a) Amphibolite*
1709 *(station BMN109). (b) Schists intercalated with hornblende-rich layers, intruded by a thin granitic sill*
1710 *(station 1688). (c) Optical photomicrograph of a hornblende-bearing leucocratic vein in amphibolite,*
1711 *with gradual accumulation of hornblende crystals in the margin. (d) Photomicrograph of a*
1712 *hornblende schist (station 1989, near 1984). The mineralogical assemblage consists of rods of*
1713 *hornblende porphyroblasts in a groundmass of quartz, plagioclase and biotite. Abbreviations: Bt =*
1714 *biotite, Hbl = hornblende.*

1715

1716 (2 columns)

1717 *Fig. 6. Field photographs of paragneiss. (a) Garnet and staurolite bearing paragneiss showing*
1718 *schistosity and crenulation, hosting a pseudo-boudin of a garnet-columbite pegmatite dyke, parallel to*
1719 *S_n schistosity and pinched in the S_{n+1} crenulation plan. (b) Paragneiss showing thin crenulated*
1720 *leucosomes and small pockets filled with quartz and feldspars. (c) and (d) Photomicrographs of a*
1721 *paragneiss (station BMS49). The axial crenulation S_{n+1} is printed in the internal texture of staurolite*
1722 *porphyroblasts. The garnet porphyroblast shown exhibits synkinematic helicitic texture in the core*
1723 *and homogeneous rims. Fibrous sillimanite is associated with biotite sheets. Abbreviations: Bt =*
1724 *biotite, Gr = garnet, Mu = muscovite, Qtz = quartz, Sil = sillimanite, St = staurolite.*

1725

1726 (2 columns)

1727 *Fig. 7. Field photographs of metatexitic paragneiss and granodioritic gneiss boarding the tonalitic-*
1728 *trondhjemitic gneiss. (a) Stromatic migmatitic paragneiss (near station BMS37). (b) Transition*
1729 *between a migmatitic paragneiss (melanocratic layers and leucosomes) and granodioritic gneiss,*
1730 *foliated granodiorite gneiss bearing garnet-columbite pegmatites pods (near BMS37). (c) Migmatitic*
1731 *paragneiss with melanocratic layers (richer in biotite, hosting leucosomes), grading to granodioritic*
1732 *gneiss, are deformed by a melt rich (quartz + feldspar) shear zone (station BMS140; compass for*
1733 *scale). (d) Garnet porphyroblasts in a migmatitic paragneiss, associated with patchy leucosomes*
1734 *(near BMS7B). (e) Synmigmatitic foliation in a migmatitic paragneiss. Quartz-feldspar-rich layers are*
1735 *leucosomes. Near-homogeneous garnet included or in contact in the leucosomes is interpreted as the*
1736 *peritectic product of a partial melting reaction. Staurolite crystals in mesosomes are wrapped by*
1737 *micas and quartz. (f) Migmatitic paragneiss, composed of quartz, feldspar, inclusion-rich*
1738 *porphyroblastic garnet surrounded by biotitic foliation, biotite and sillimanite. Abbreviations: Bt =*
1739 *biotite, Gr = garnet, Sil = sillimanite, St = staurolite.*

1740

1741 (2 columns)

1742 *Fig. 8. Field photographs of the tonalitic-trondhjemitic gneiss. (a) Biotite and magnetite leucotonalitic*
1743 *facies, crossed by a leucocratic vein containing mafic clots (hornblende, biotite and magnetite)*
1744 *(station BMN11). (b) Mesocratic enclave, hosting deformed leucocratic veins in textural continuity*
1745 *with the tonalitic mesostase. (c) Schollen-like texture in gneissic facies of the tonalitic-trondhjemitic*
1746 *gneiss. Mesocratic rafts are traversed by a hornblende tonalite vein (station BMS124). (d) Hornblende*
1747 *tonalite veins parallel to foliation are affected by folding. Transverse veins circulate next to axial plan*
1748 *of folds (station BMN11; compass in foreground for scale). (e) Mafic clots of poikilitic assemblage of*
1749 *biotite and hornblende, exposed as pseudomorphs of minerals with hexagonal basal section*
1750 *(hornblende); head of rock hammer for scale.*

1751

1752 (2 columns)

1753 *Fig. 9. Polarized photomicrographs of the tonalitic-trondhjemitic gneiss. a) The image is dominated*
1754 *by subhedral oligoclase showing diffuse contacts, suggestive of slow cooling, and connected by triple*
1755 *joints. Anhedral oligoclase shows well-developed polysynthetic twins. Recrystallized quartz corrodes*
1756 *plagioclase grain borders, which might correspond to liquid product from plagioclase consumption.*

1757 *(b) Batches of recrystallized quartz corrode the plagioclase grain in the center of the picture, whereas*
1758 *melt is trapped between plagioclase grains in the lower part. Abbreviations: Bt = biotite, Ep = epidote,*
1759 *Pg = plagioclase, Qtz = quartz.*

1760

1761 (2 columns)

1762 *Fig. 10. Field photographs of plutonic rocks from Mangodara district. (a) Layered GG-granitoid, with*
1763 *mesocratic layers and K-feldspar-rich leucocratic layers. (b) Disrupted blocks of gabbro in an*
1764 *intrusive pink granite (GG-granitoid). (c) Porphyritic biotite granite, with megacrysts of K-feldspar*
1765 *(GG-granitoid). (d) Hornblende-biotite granodiorite, bearing elongated mica-rich enclaves (station*
1766 *BMS23). (e) Two-mica granite enclosing rounded enclaves of tonalitic-trondhjemitic gneiss (station*
1767 *BMS9).*

1768

1769 (2 columns)

1770 *Fig. 11. Field photographs of pegmatite veins and their relationships with their host rocks. (a)*
1771 *Network of interconnected veins of titanite-allanite pegmatite in tonalitic-trondhjemitic gneiss. (b)*
1772 *Garnet-columbite pegmatite vein cross-cutting apatite-zircon pegmatite (station BMS99A). (c) Rotated*
1773 *and pinched pods of garnet-columbite pegmatite in a layered granodioritic gneiss (near station*
1774 *BMS37). (d) Folded and pinched garnet-columbite pegmatite vein, with well-developed quartz core.*
1775 *(e) Cuspate interfaces between the paragneiss and a garnet-columbite pegmatite dyke. (f) Garnet-REE*
1776 *pegmatite connected with leucosomes layers veins in a granodioritic gneiss (station BB24). (g)*
1777 *Garnet-REE pegmatite veins in porphyritic granodioritic gneiss, deformed by thin mylonites crossing*
1778 *dyke, or bordering the contact with the granodioritic gneiss (near station BB15).*

1779

1780 (2 columns)

1781 *Fig. 12. (a) and (b) Contact between apatite-zircon pegmatite (section with biotite) and garnet-*
1782 *columbite pegmatite (section rich in muscovite and hosting garnet). Abbreviations: Bt = biotite, Gr =*
1783 *garnet, Mu = muscovite.*

1784

1785 (1 columns)

1786 *Fig. 13. Metamorphic conditions prevailing in the Mangodara district. Volcanic belts greenschist*
1787 *facies paragenesis is taken from Ilboudo et al., (2017b). Legend as in Fig. 2. Abbreviations: Bt =*
1788 *biotite, Gr = garnet, Hbl = hornblende, Ky = kyanite, Mu = muscovite, Sil = sillimanite, St =*
1789 *staurolite.*

1790

1791 (2 columns)

1792 Fig. 14. (a) Calculated P-T pseudosection for sample BMS114B in the NCKFMASHTO system. The
1793 light blue field represents the subsolidus stability domain of aqueous fluid (H_2O). The dark blue field
1794 represents the suprasolidus field in presence of a silicate melt. Ilmenite was stable in all parts of the
1795 computed pseudosection. The dashed line indicates the representative mineral assemblages of
1796 paragneisses from Mangodara district, inferred from the mineralogy of sample BMS114B and
1797 mineralogical observations (e.g. Fig. 6). (b) Calculated P-T pseudosection for sample BMN109 in the
1798 NCFMASHTO system. Field are colored as indicated in (a). (c) and (d) Variation of mineral volume
1799 fractions between 500 °C and 700 °C at a pressure of 7 kbar, in paragneiss and amphibolite.
1800 Abbreviations: *bt* = biotite, *chl* = chlorite, *cord* = cordierite, *cpx* = clinopyroxene, *ilm* = ilmenite, *gr*
1801 = garnet, *hbl* = hornblende, *kfs* = K-feldspar, *ky* = kyanite, *liq* = silicate melt, *mu* = muscovite, *opx* =
1802 orthopyroxene, *pg* = plagioclase, *qtz* = quartz, *sil* = sillimanite, *st*, = staurolite.

1803

1804 (2 columns)

1805 Fig. 15. U-Pb chronological data obtained on zircons from the titanite-allanite type pegmatite
1806 BMN28. (a) Cathodoluminescence images of two zircon grains analyzed. Circles locate the analyzed
1807 spots, the red color designating discordant data, whereas yellow indicates concordant data. (b-c)
1808 Concordia and Discordia diagrams, respectively. The size of the ellipses represents an uncertainty of
1809 2 sigma. The ellipse color indicates the textural position of the analyses: blue for the core, orange for
1810 the rim.

1811

1812 (2 columns)

1813 Fig. 16. U-Pb chronological data obtained on apatite. Cathodoluminescence images of apatite in (a)
1814 granodioritic gneiss (BMN20B), (b) tonalitic-trondhjemite gneiss (BMN11) and (c) apatite-zircon
1815 type pegmatite (BMN20). Red circles indicate the emplacements of the analyzed spots. Tera-
1816 Wasserburg diagram plotting U-Pb isotopic data from apatite in (d) granodioritic gneiss (BMN20B),
1817 (e) tonalitic-trondhjemite gneiss (BMN11) and (f) apatite-zircon-type pegmatite (BMN20).

1818

1819 (2 columns)

1820 *Fig. 17. REE spider diagram of (a) amphibolite, micaschist, and paragneiss, (c) gneisses and*
1821 *granitoids and (e) pegmatites normalized to chondrite (McDonough and Sun, 1995). Multi-elements*
1822 *spider diagram of (b) amphibolite, micaschist and paragneiss, (d) gneisses and granitoids, and (f)*
1823 *pegmatites normalized to primitive mantle (Sun and McDonough, 1989). Filled patterns correspond to*
1824 *granodioritic gneiss (blue), tonalitic-trondhjemitic gneiss (pink) and calc-alkaline basalt (green) from*
1825 *the Houndé greenstone belt, and Tiébélé greenstone belt (Baratoux et al., 2011; Ilboudo et al., 2017a).*

1826

1827 (2 columns)

1828 *Fig. 18. Geochemical discriminant diagrams for gneisses and plutonic rocks. (a) Chemical index*
1829 *alteration ($CIA = Al_2O_3 / (Al_2O_3 + CaO^* + Na_2O + K_2O) * 100$, CaO^* corresponding to amount of Ca*
1830 *incorporated in silicates, considering the apatite component (Nesbitt and Young, 1982, 1984). (b)*
1831 *Shand index plot (Shand, 1943) showing most of the gneiss and granitoids in the metaluminous*
1832 *domain. (c) Diagram of SiO_2 vs K_2O (Peccerillo and Taylor, 1976) including domains corresponding*
1833 *to plagioclase and amphibole accumulation (in shades of gray, Laurent et al., 2020). (d) Quartz-*
1834 *alkali felspar-plagioclase (QAP) diagram for felsic gneisses and granitoids (Streckeisen and Le*
1835 *Maitre, 1979). Modal compositions are calculated in CIPW norm and validated by comparison with*
1836 *mineral compositions of corresponding samples. (e) Total alkali-silica diagram (SiO_2 vs $Na_2O + K_2O$,*
1837 *Cox et al., 1979). (f) Diagram plotting Sr/Y vs La/Yb also showing domains of high-, middle- and low-*
1838 *pressure TTG, according to Moyen, (2011). (g, h) Binary ratio plots depicting K/Rb versus Ca/Cs and*
1839 *Nb/Ta versus Zr/Hf for gneisses, granitoids and pegmatites, respectively.*

1840

1841 (2 columns)

1842 *Fig. 19. Cross-section representing the structural setting of the Mangodara dome, cored by tonalitic-*
1843 *trondhjemite gneiss and flanked by two shear zones. Plutonic rocks, from the left to the right,*
1844 *represent respectively the hornblende-biotite granodiorite, the two-mica tonalite and the GG-*
1845 *granitoids intruded by porphyritic biotite granite. The mantling granodioritic gneiss represent a*
1846 *diatectite including rafts of partially molten Birimian volcano-sedimentary amphibolite-schist and*
1847 *paragneiss. Plutonic rocks are formed by melt collected within the gneiss, and pegmatites are formed*
1848 *by melt segregation in the gneisses and the rafts of migmatitic paragneiss-amphibolite.*

1849

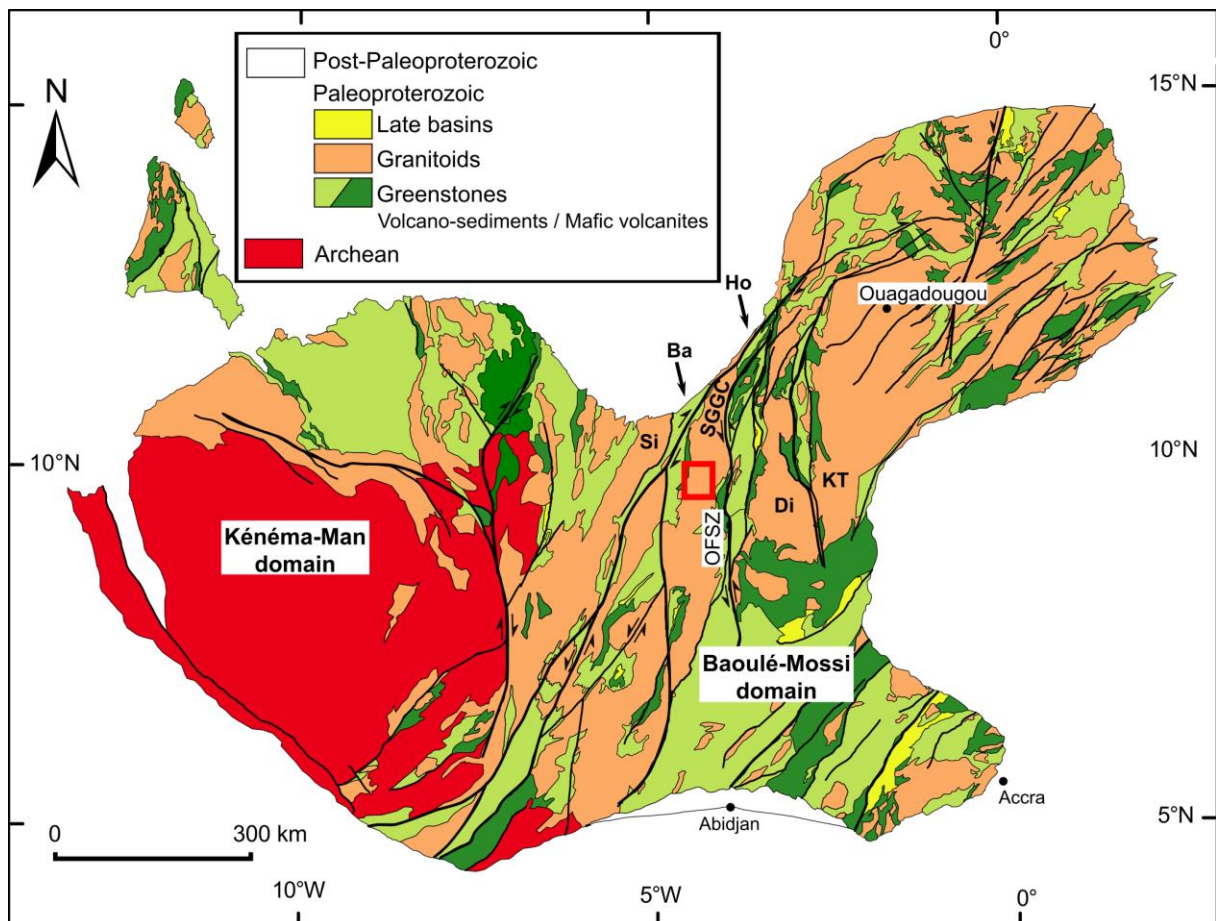
1850 (2 columns)

1851 *Fig. 20. Recapitulative interpretation of the petrogenetic relationships among amphibolites, schists,*
1852 *paragneiss, gneisses, plutonic rocks and pegmatites in the Mangodara district.*

1853

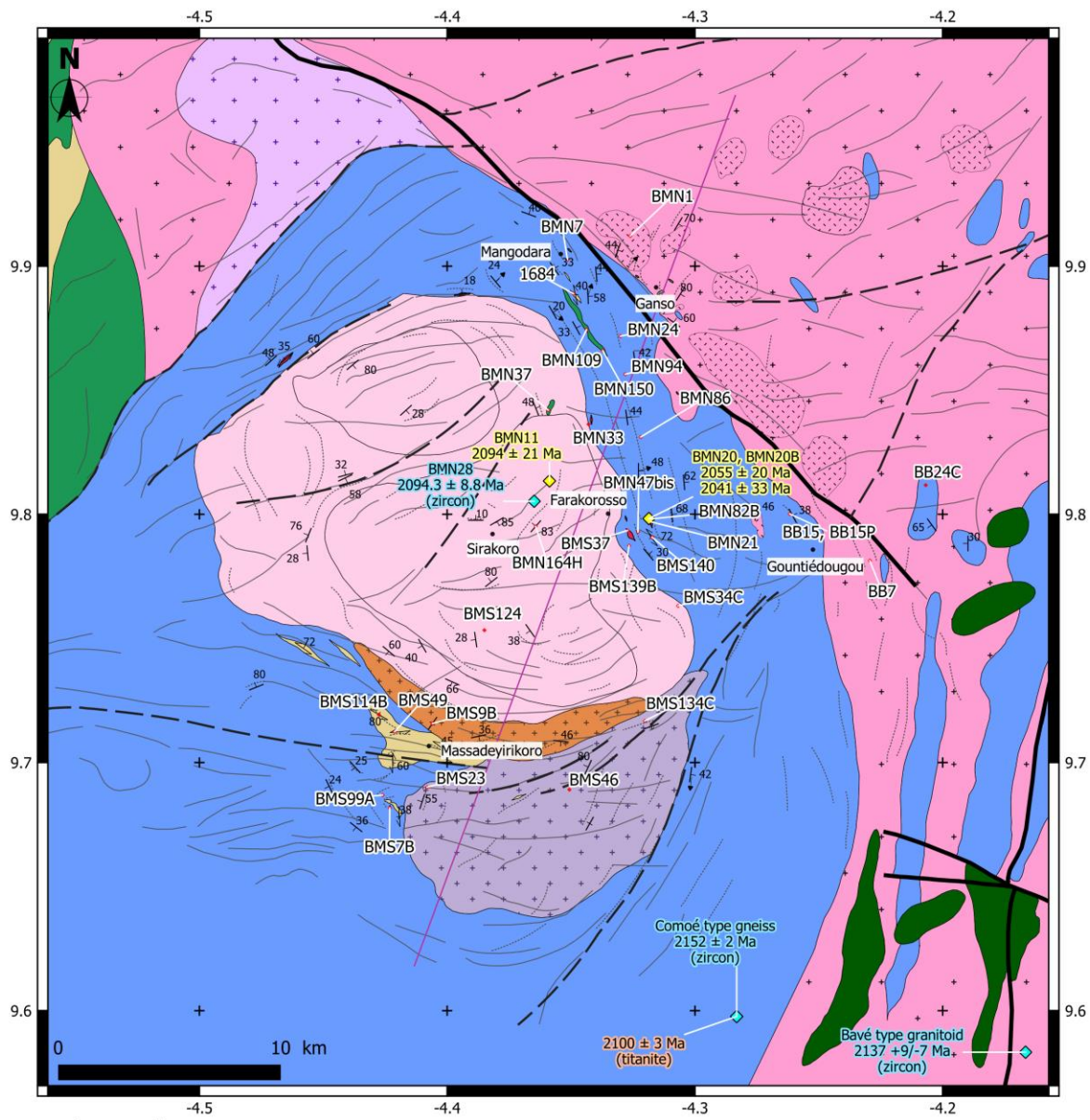
1854

1855 **Figures**



1856

1857



Legend

Plutonic rocks

- Mafic and ultramafic intrusion
- ✖ Porphyritic biotite monzogranite and granite
- ✖ Biotite granite and monzogranite
- ✖ Biotite and hornblende granodiorite
- ✚ Two-mica tonalite
- ✖ + Hornblende-biotite granodiorite with surmicaceous enclaves

Gneisses and migmatites

- + Tonalitic-trondhjemitic gneiss
- ✖ Granodioritic gneiss
- ✖ Metatexitic paragneiss

Meta-volcanic and meta-sedimentary units

- ▲ Metavolcano-sediments/Paragneiss
- ▲ Metabasalte-andesite/Amphibolite

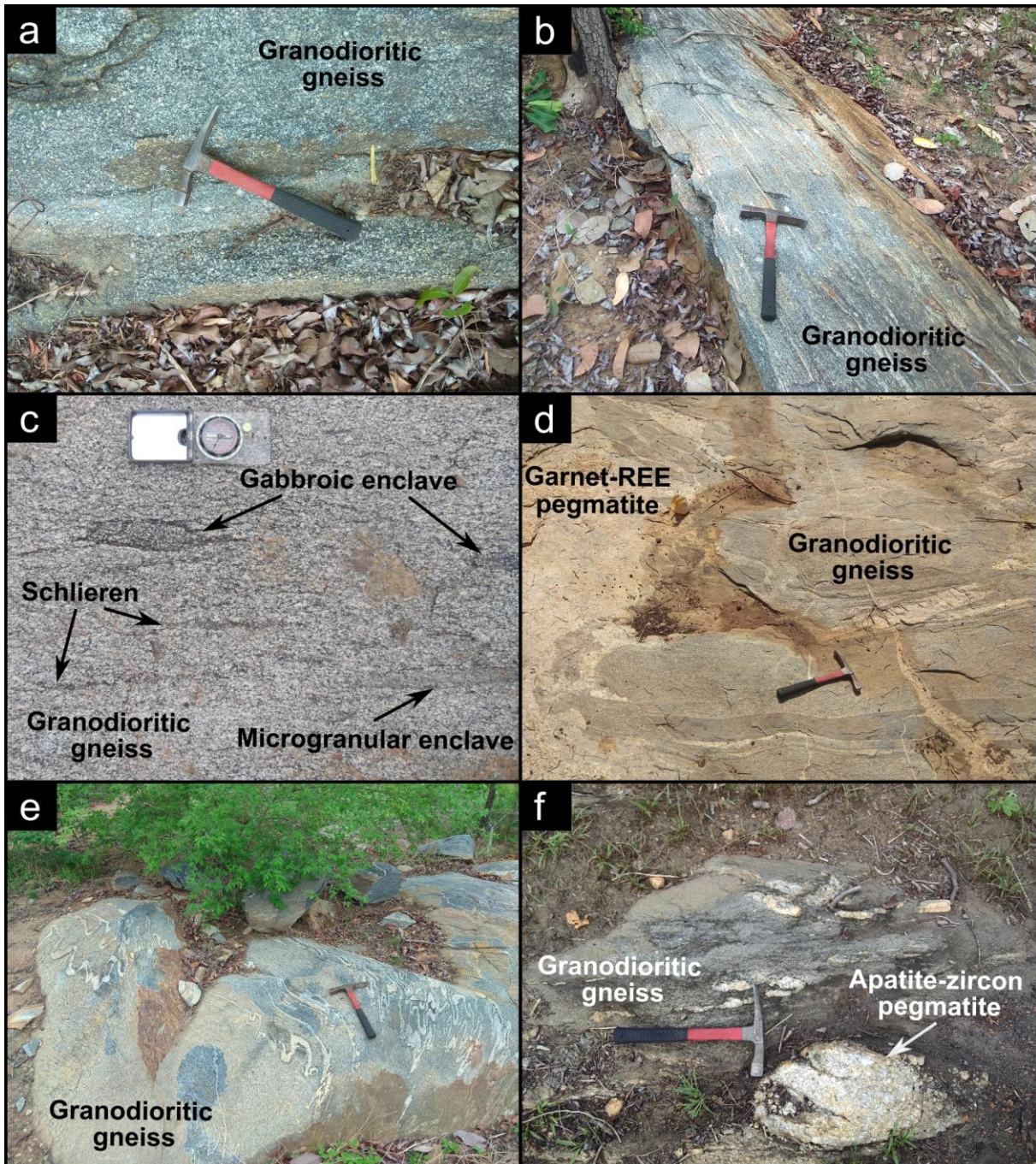
— Baseline of geological cross-section (later in this paper)

- Village location
- Sample location
- ◆ U-Pb age on zircon/titanite
- ◇ U-Pb age on apatite

Structure

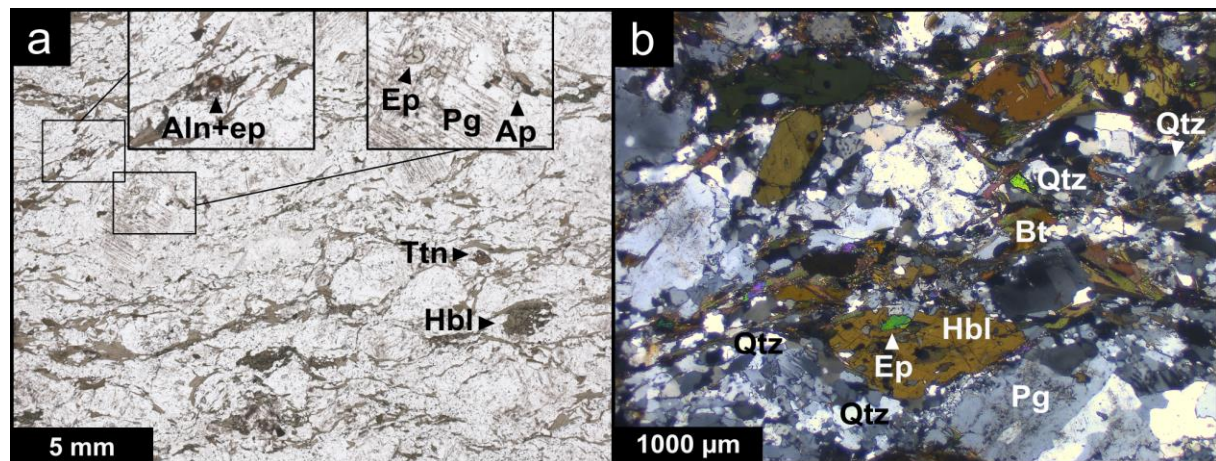
- Shear zone
- Interpreted shear zone
- Magnetic lineament
- Aerial lithofabric

- Foliation and lineation
- ↑ Vertical foliation
- Horizontal foliation
- ↔ Schistosity

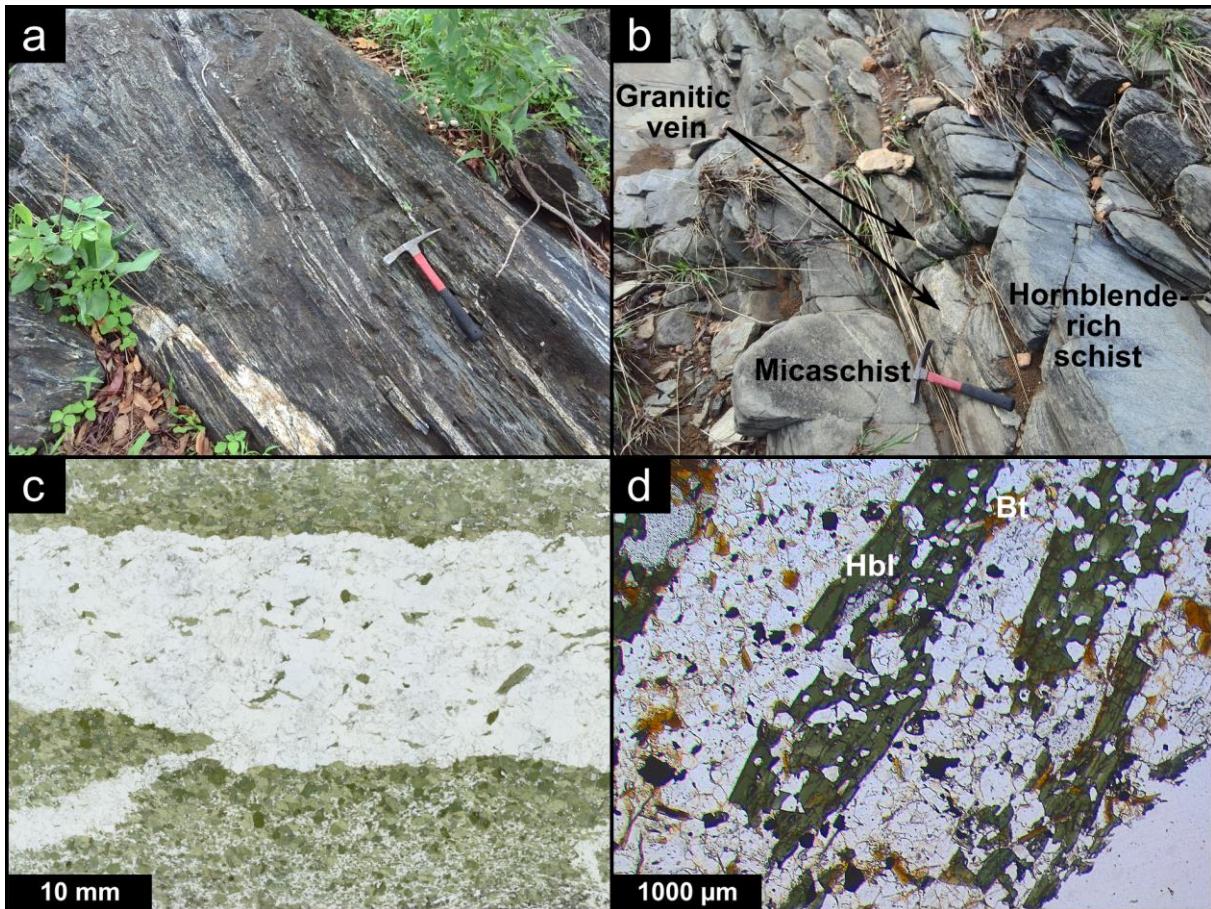


1859

1860

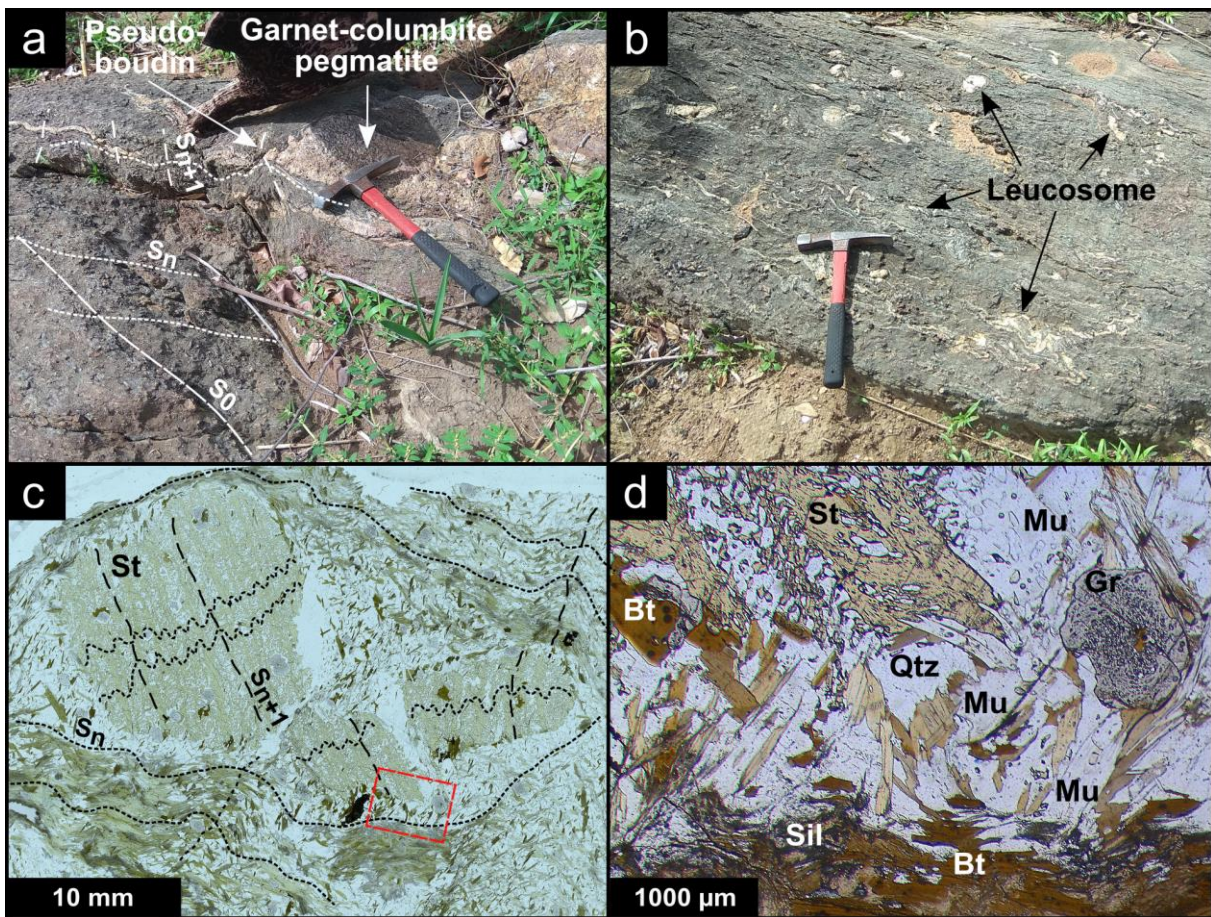


1862



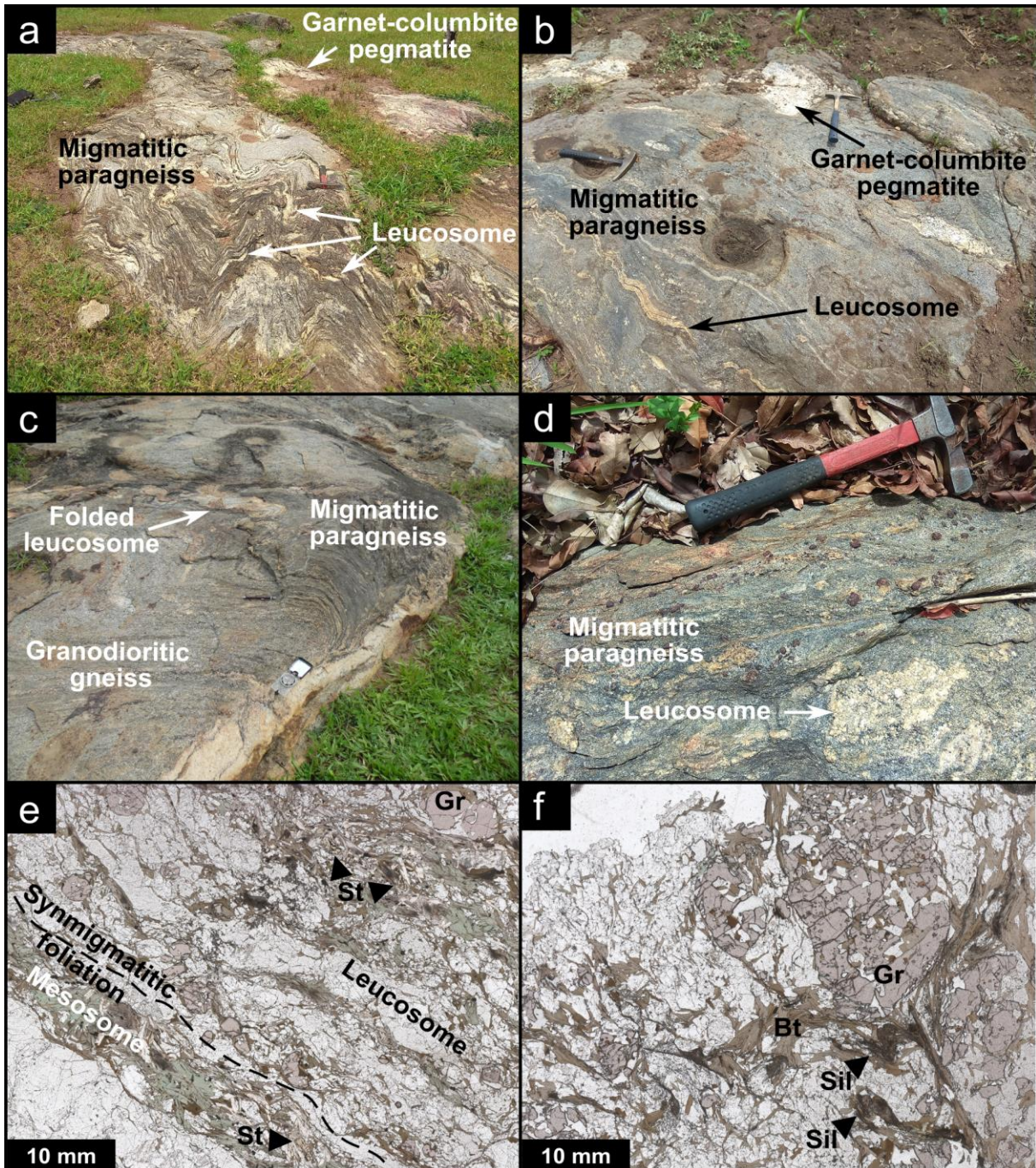
1863

1864



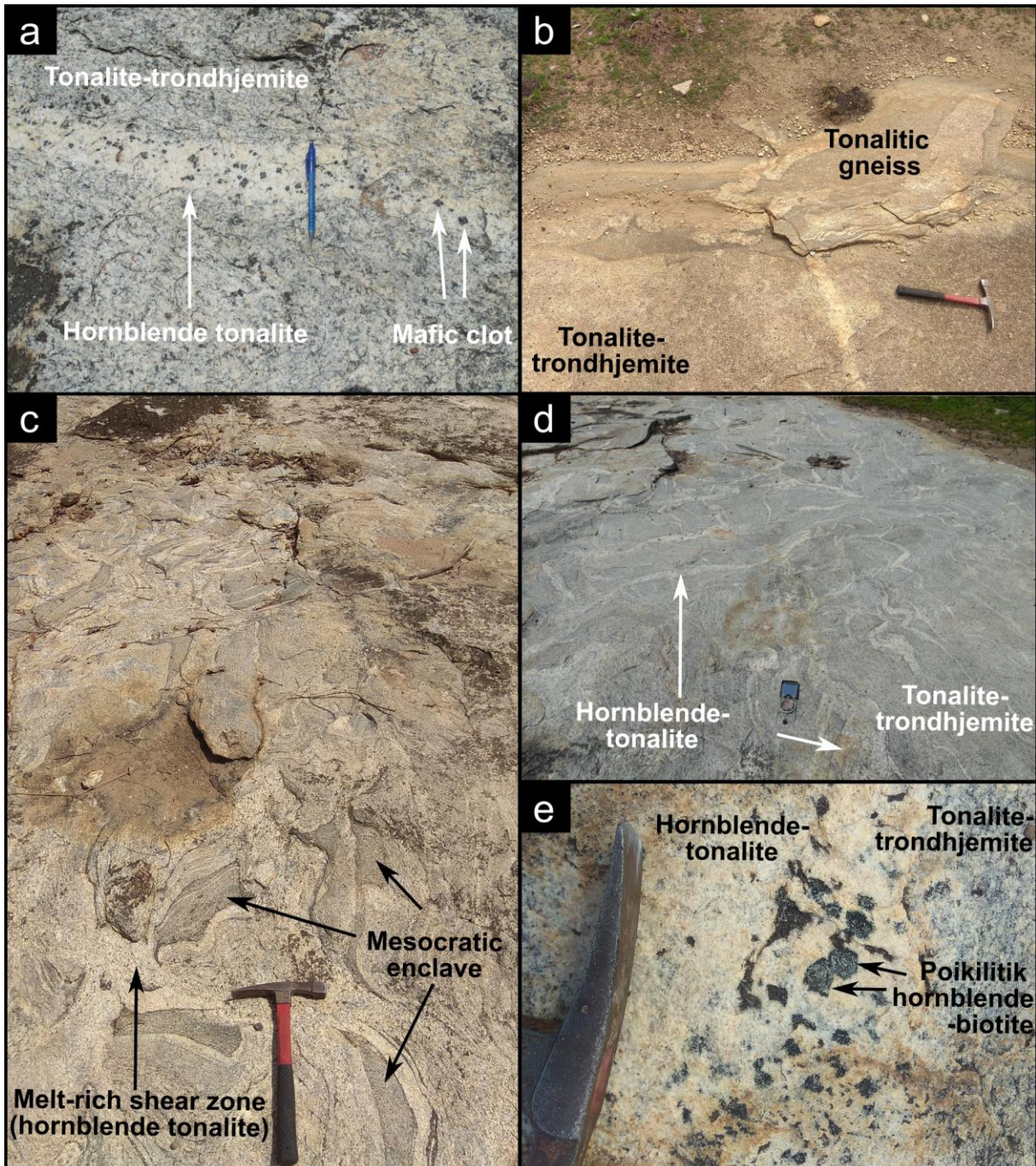
1865

1866



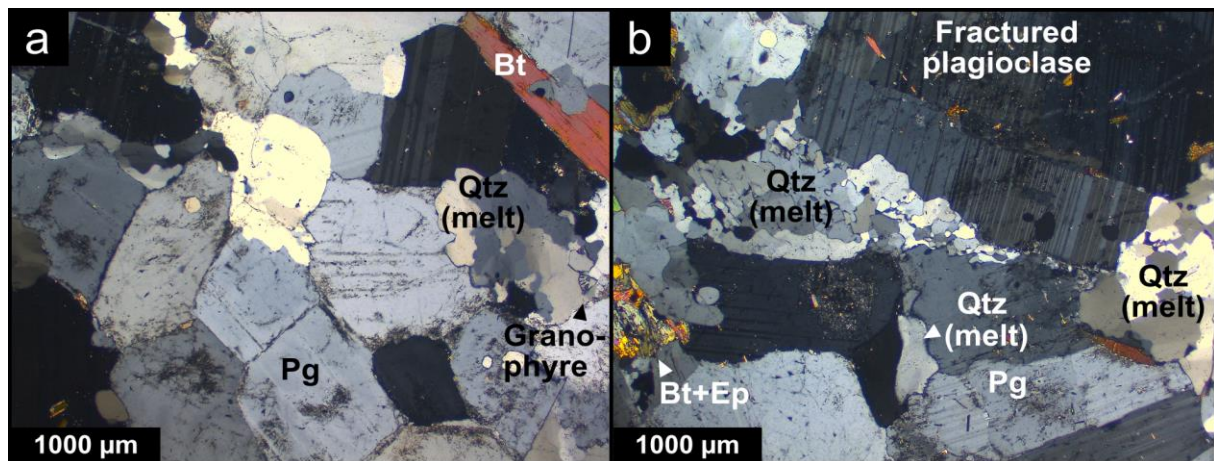
1867

1868

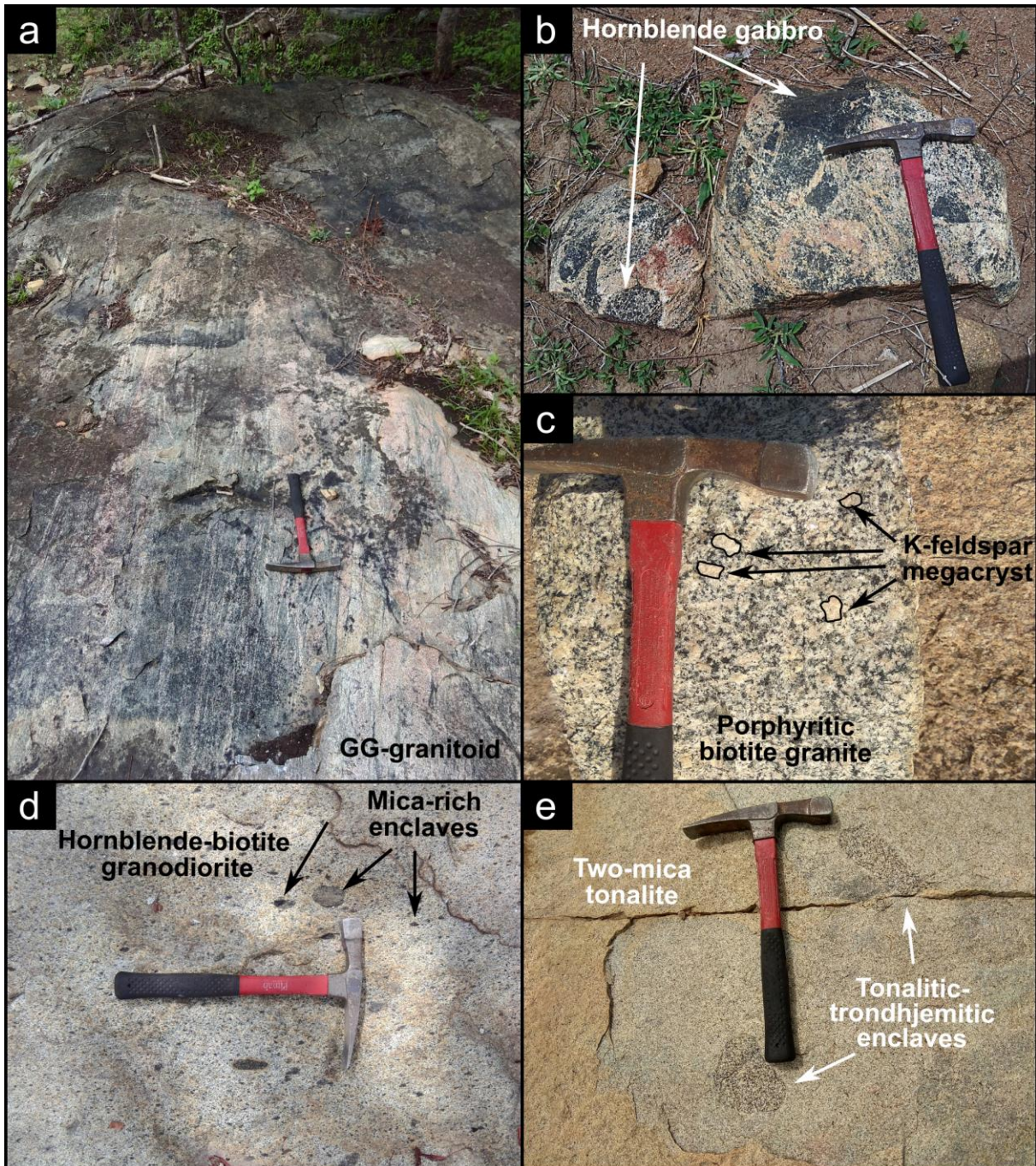


1869

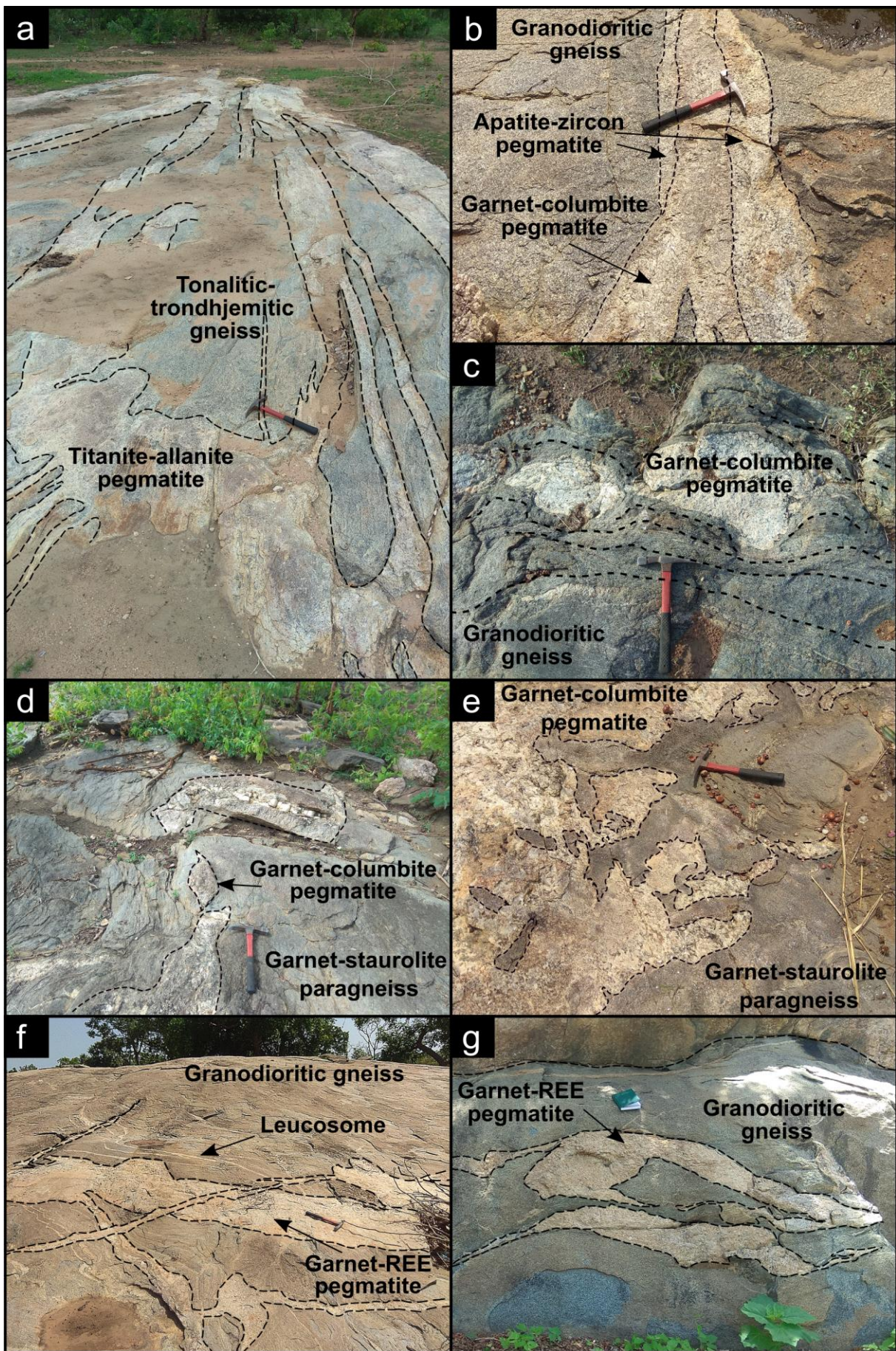
1870

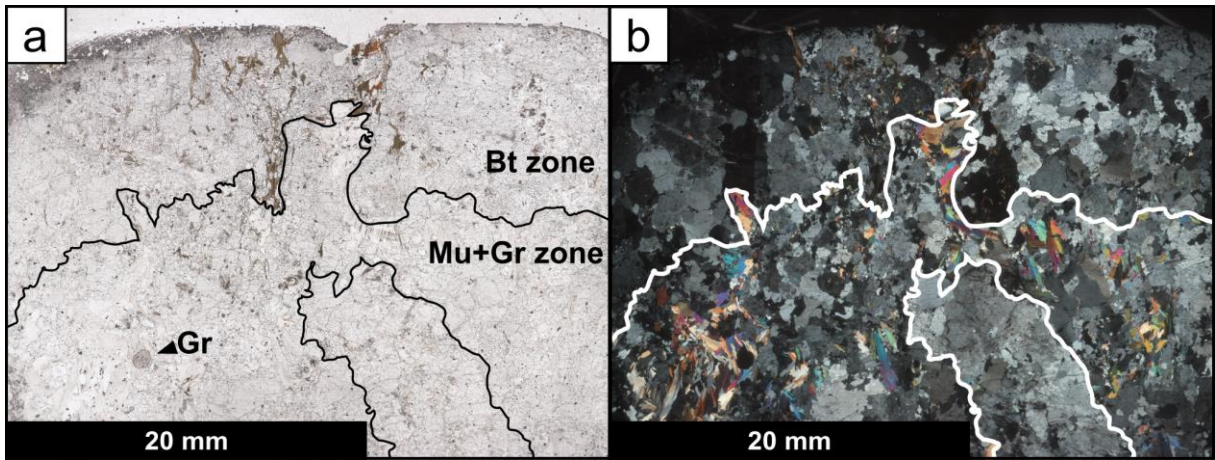


1872

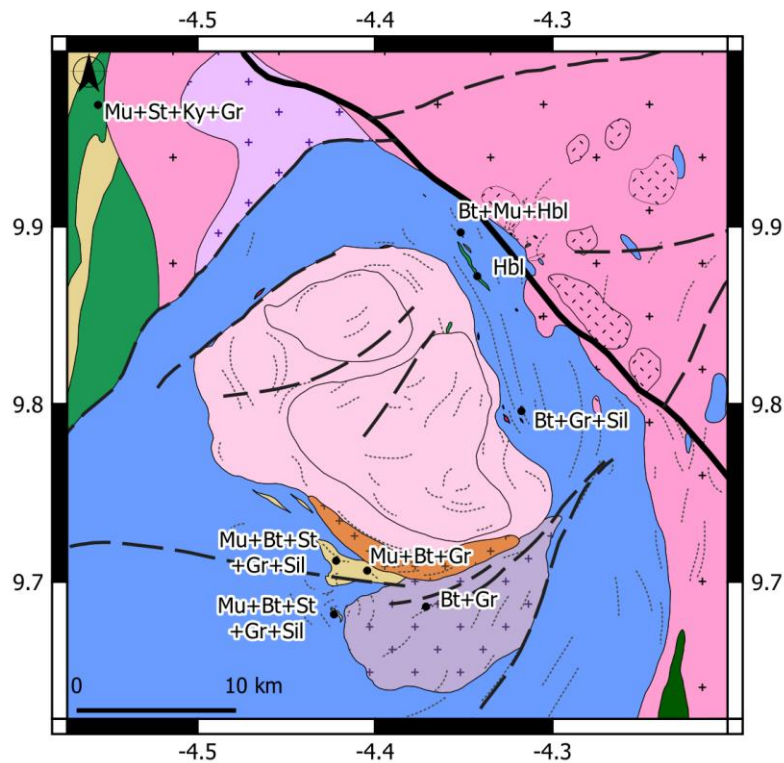


1873



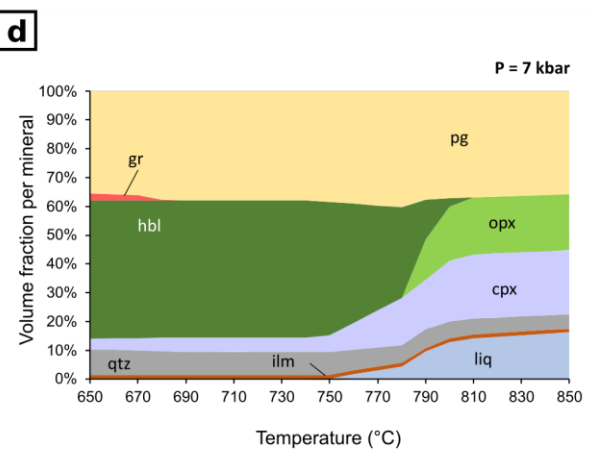
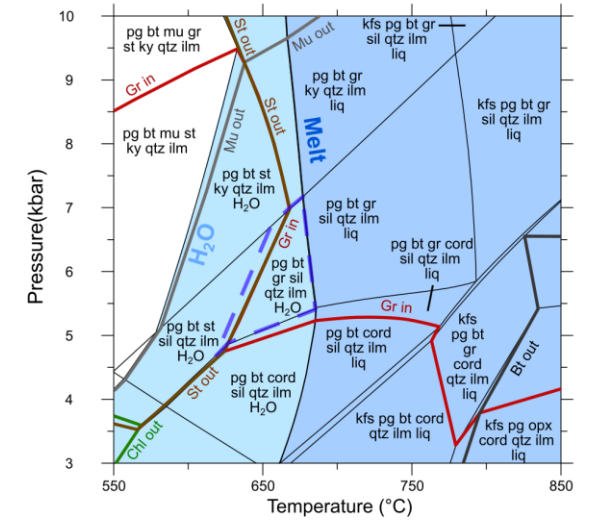
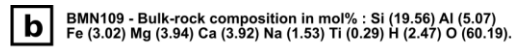
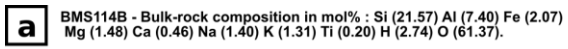


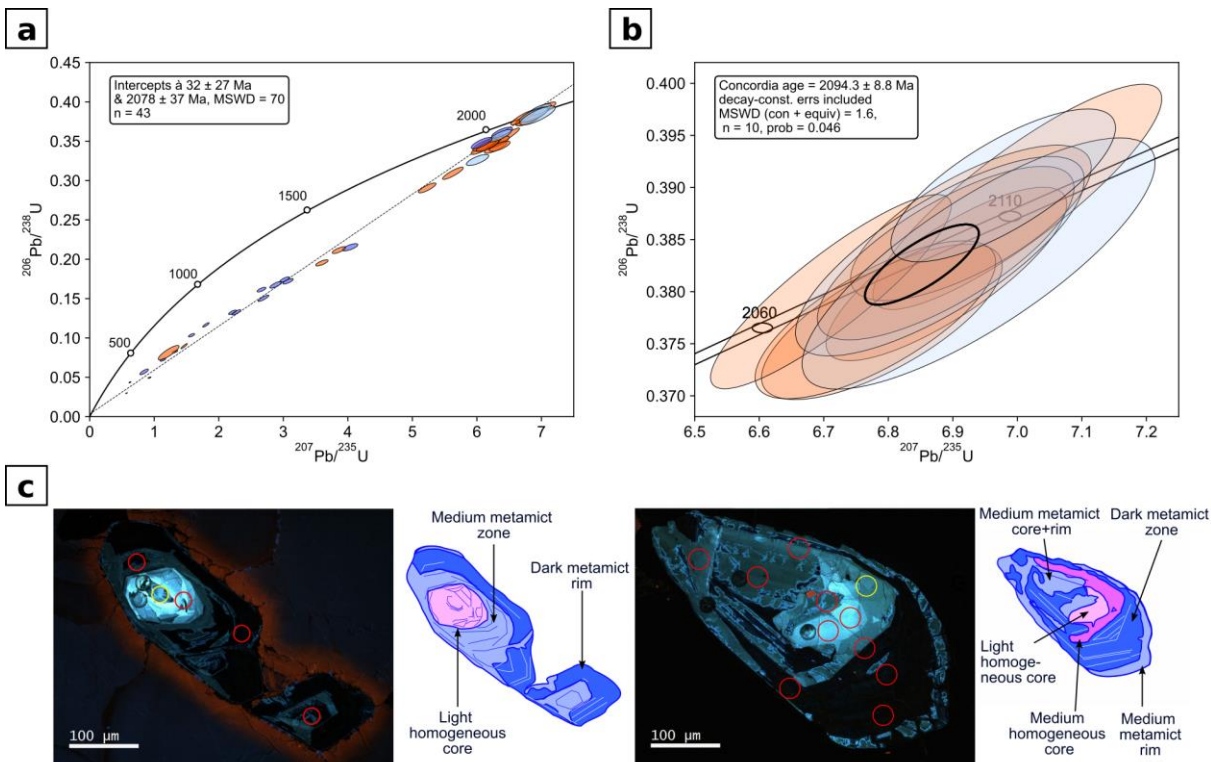
1876



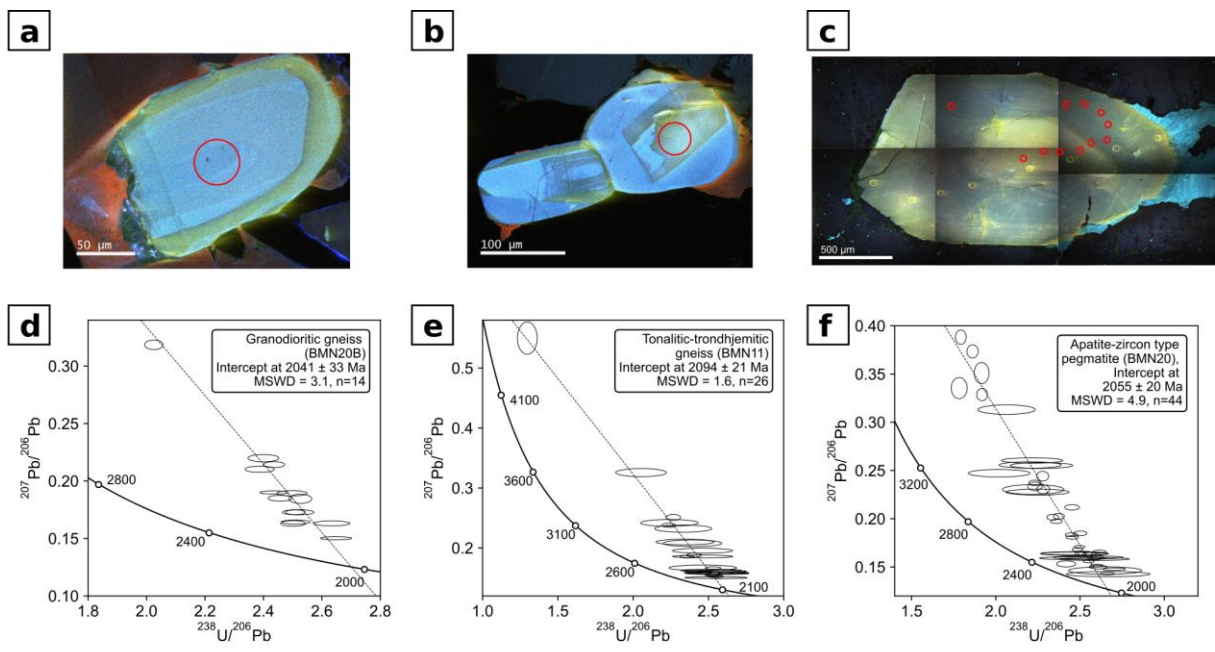
1877

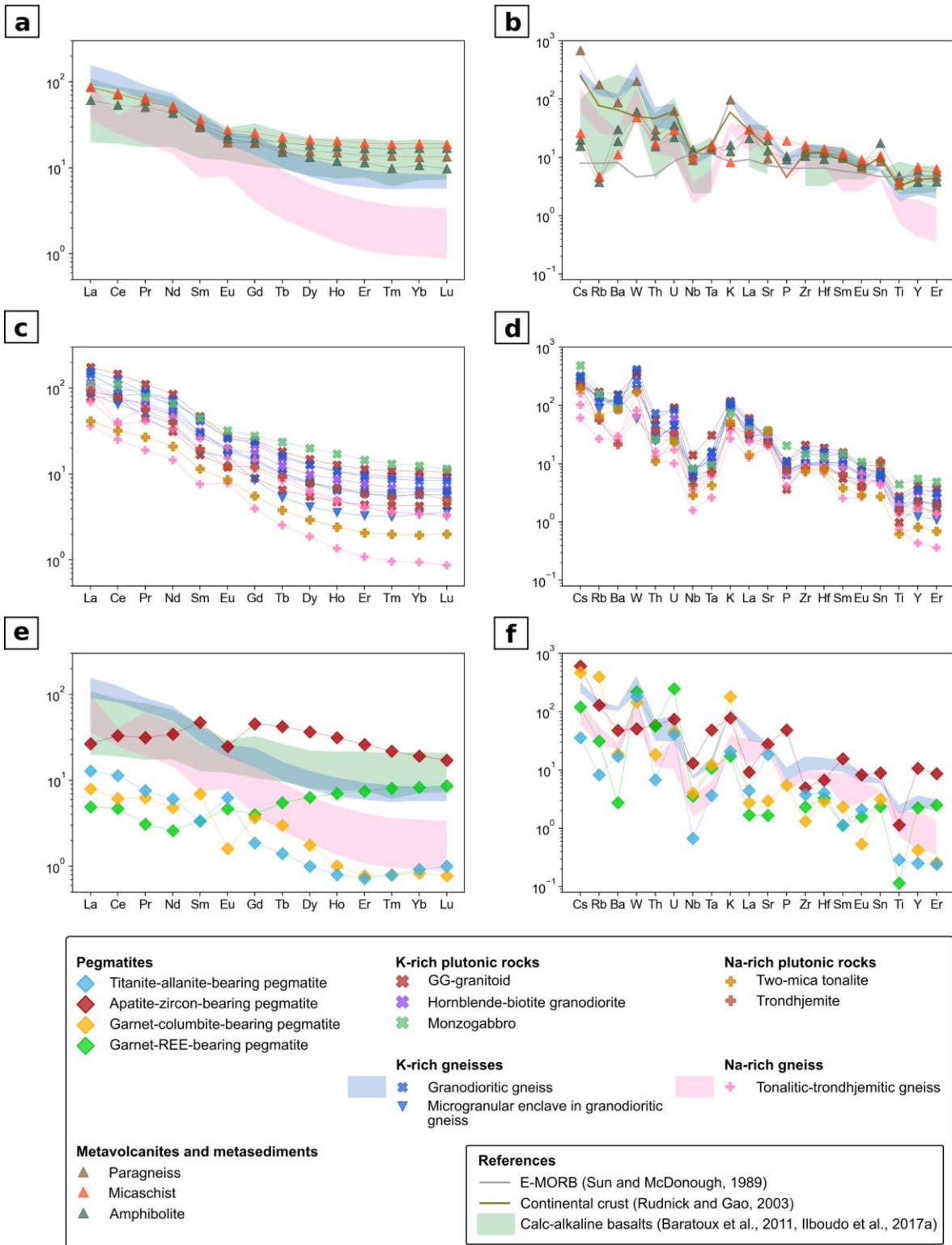
1878

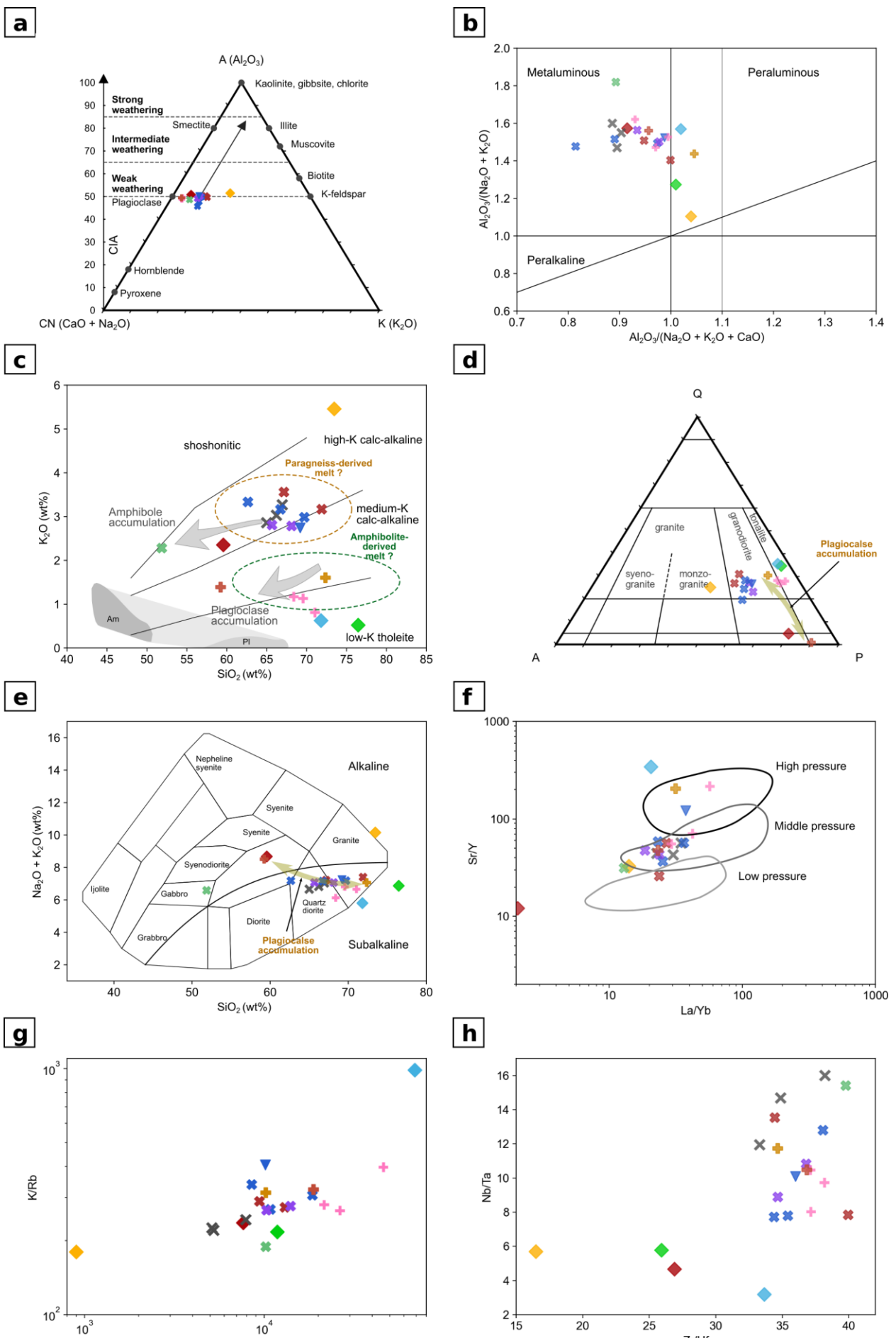


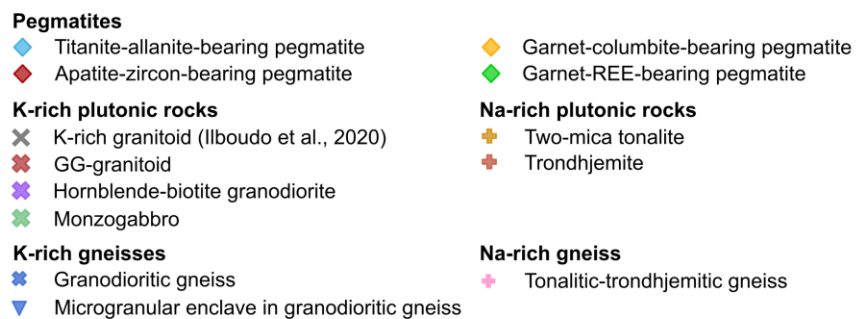


1880

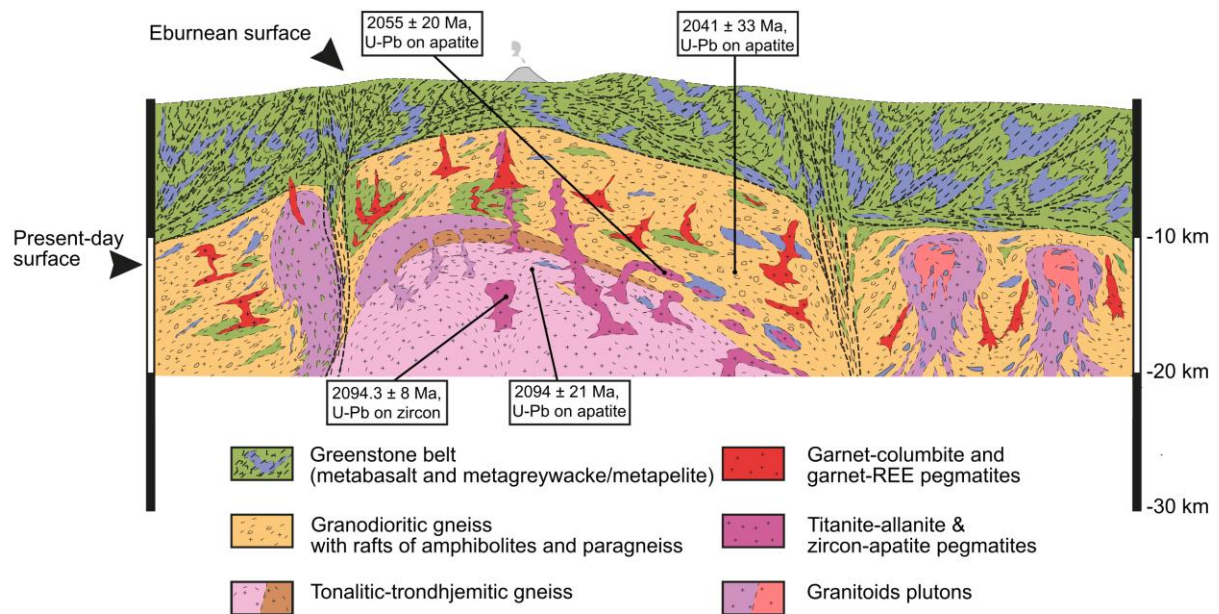


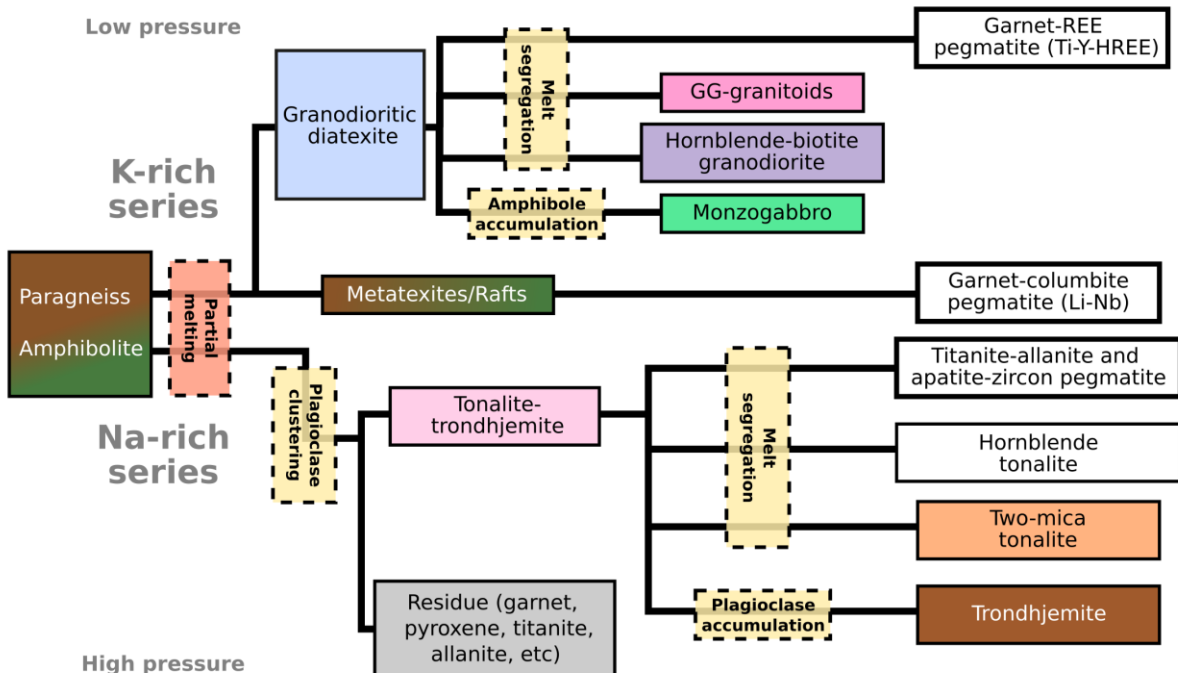






1884





1887 **Tables**

1888 Table 1. Isotopic data for in-situ LA-ICP-MS zircon dating of the titanite-allanite-type pegmatite

N°	U (ppm)	Th (ppm)	Pb (ppm)	Position	Texture	Th/U	$^{207}\text{Pb}/^{235}\text{U}$	$\overline{2\sigma}$		$^{206}\text{Pb}/^{238}\text{U}$	$\overline{2\sigma}$		Rho	$^{207}\text{Pb}/^{206}\text{Pb}$	$\overline{2\sigma}$		Age $^{207}\text{Pb}/$	$\overline{2\sigma}$		Age $^{206}\text{Pb}/$	$\overline{2\sigma}$		Age $^{207}\text{Pb}/$	$\overline{2\sigma}$		
								^{235}U	^{238}U		^{206}Pb	^{207}Pb	^{235}U		^{238}U	^{206}Pb	^{235}U	^{238}U	^{206}Pb	^{235}U	^{238}U	^{206}Pb		^{235}U	^{238}U	
1	313	35	243	Core	Oscillatory	0.11	3.598	0.078	0.1954	0.003	0.7554	0.1328	0.002	1546.5	18	1150	17	2128	21							
2	722	1	382	Metamict rim	Oscillatory-patchy	0.00	4.035	0.097	0.2152	0.004	0.7152	0.13381	0.002	1633	20	1255	20	2144	20							
3	27	5	28	Core	Oscillatory	0.17	6.4	0.21	0.353	0.011	0.9497	0.1342	0.003	2001	29	1915	49	2110	42							
4	15	0	1	Medium zone	Oscillatory	0.00	6.88	0.18	0.3834	0.008	0.7676	0.1282	0.002	2078	24	2083	36	2047	33							
5	16	0	2	Medium zone	Oscillatory	0.00	6.94	0.22	0.3827	0.01	0.7996	0.129	0.003	2091	27	2080	45	2064	38							
6	168	0	26	Core	Oscillatory	0.00	7	0.18	0.3891	0.009	0.8695	0.1298	0.002	2108	27	2112	42	2091	21							
7	1528	0	288	Metamict rim	Oscillatory-patchy	0.00	1.801	0.041	0.1166	0.002	0.8665	0.1155	0.001	1046	18	710	13	1881	23							
8	109	32	196	Core	Oscillatory	0.29	6.89	0.15	0.3817	0.007	0.8063	0.1305	0.002	2090	20	2081	31	2094	23							
9	680	6	160	Metamict rim	Patchy	0.01	3.02	0.062	0.1742	0.003	0.7829	0.1217	0.001	1411.9	16	1034	15	1977	21							
10	83	25	168	Core	Oscillatory	0.30	6.29	0.14	0.3422	0.006	0.8009	0.1355	0.002	2009	19	1894	29	2166	24							
11	52	10	59	Medium zone	Oscillatory	0.19	6.36	0.14	0.3569	0.006	0.8019	0.1315	0.002	2020	20	1961	30	2103	26							
12	143	43	261	Core	Oscillatory	0.30	5.628	0.13	0.3092	0.006	0.8821	0.1323	0.002	1918	21	1733	31	2117	27							
13	107	45	283	Core	Oscillatory	0.42	6.79	0.15	0.3771	0.006	0.7202	0.1328	0.002	2080	19	2059	28	2131	22							
14	1567	1	410	Metamict rim	Oscillatory	0.00	1.323	0.033	0.0827	0.001	0.6785	0.11304	0.001	853.7	16	512.1	8.6	1843	24							
15	1815	6	455	Metamict rim	Oscillatory	0.00	1.135	0.035	0.0723	0.002	0.7176	0.1168	0.001	768.9	15	450	9.5	1903	21							
16	843	1	262	Metamict rim	Oscillatory	0.00	3.073	0.066	0.172	0.003	0.7580	0.1279	0.002	1423	17	1022	16	2063	23							
17	127	53	287	Core	Oscillatory	0.42	6.329	0.14	0.3491	0.006	0.7640	0.1316	0.002	2017.6	19	1927	28	2114	22							

18	81	40	212	Core	Oscillatory	0.49	6.928	0.15	0.3866	0.006	0.7168	0.1308	0.002	2098.4	19	2106	28	2100	22
19	1621	2	332	Metamict rim	Oscillatory-patchy	0.00	1.578	0.039	0.1034	0.002	0.7044	0.11127	0.001	958.2	15	633.7	10	1812	22
20	997	3	191	Metamict rim	Oscillatory-patchy	0.00	2.662	0.055	0.1614	0.002	0.7197	0.12063	0.001	1316.3	15	964.3	13	1960	20
21	129	26	168	Core	Oscillatory	0.20	3.862	0.084	0.2116	0.004	0.7605	0.1338	0.002	1602.8	18	1235	18	2142	23
22	1533	4	354	Core	Oscillatory-patchy	0.00	1.463	0.041	0.0896	0.003	0.9300	0.1259	0.002	916	18	555	16	2030	26
23	79	38	206	Core	Oscillatory	0.48	6.78	0.15	0.3773	0.006	0.7308	0.1319	0.002	2082	19	2060	29	2115	23
24	56	2	31	Medium zone	Oscillatory	0.04	6.01	0.14	0.3261	0.006	0.7504	0.1346	0.002	1972	20	1816	27	2144	25
25	2615	4	510	Metamict rim	Oscillatory-patchy	0.00	0.843	0.054	0.0569	0.003	0.7961	0.10376	0.001	618.9	23	356.5	17	1688	23
26	2029	0	374	Metamict rim	Oscillatory-patchy	0.00	2.883	0.074	0.1675	0.003	0.7908	0.11968	0.001	1375.9	25	998	19	1948	23
27	1096	1	351	Metamict rim	Oscillatory-patchy	0.00	2.271	0.056	0.1325	0.003	0.8264	0.1257	0.002	1200	21	801	16	2036	24
28	544	2	71	Metamict core	Oscillatory-patchy	0.00	6.166	0.14	0.3444	0.006	0.7801	0.1304	0.002	1997	20	1905	30	2097	21
29	112	0	39	Core	Homogeneous	0.00	6.353	0.13	0.3435	0.005	0.7540	0.132	0.002	2023	19	1903	25	2117	22
30	304	0	32	Core	Patchy	0.00	5.23	0.11	0.2906	0.005	0.8344	0.1322	0.002	1853	19	1642	26	2122	20
31	219	0	9	Metamict core	Oscillatory-patchy	0.00	6.711	0.15	0.38	0.008	0.8830	0.12996	0.002	2069	23	2072	36	2091	20
32	728	0	202	Transition core-rim	Oscillatory-patchy	0.00	2.212	0.049	0.1326	0.002	0.7830	0.12273	0.002	1181.9	16	802.3	13	1990	22
33	3558	9	1257	Metamict rim	Oscillatory-patchy	0.00	0.9263	0.02	0.0495	0.0008	0.7386	0.13913	0.002	665.3	10	311.6	4.8	2212	21
34	4931	3	1344	Metamict rim	Oscillatory-patchy	0.00	0.5711	0.012	0.0298	0.0005	0.8134	0.14287	0.002	458.1	7.9	189.5	3.2	2258	21

35	3527	3	635	Metamict rim	Oscillatory-patchy	0.00	0.6233	0.013	0.0436	0.0007	0.7473	0.10623	0.001	491.8	8	275.2	4.2	1727	25
36	699	1	26	Metamict core	Oscillatory-patchy	0.00	6.391	0.13	0.3611	0.005	0.7352	0.1296	0.001	2029.2	18	1985	26	2088	19
37	855	0	223	Metamict rim	Oscillatory-patchy	0.00	2.693	0.068	0.1504	0.003	0.8689	0.1323	0.002	1324	18	902	18	2123	21
38	509	0	51	Transition core-rim	Patchy	0.00	6.074	0.13	0.3476	0.006	0.7796	0.13033	0.002	1983.5	20	1920	28	2098	20
39	73	29	164	Core	Oscillatory	0.40	6.889	0.16	0.3837	0.007	0.7518	0.1318	0.002	2093	20	2090	31	2115	23
40	25	0	4	Core	Homogeneous	0.01	6.16	0.2	0.3456	0.01	0.8912	0.1333	0.002	1970	31	1896	51	2110	32
41	185	2	43	Core	Oscillatory	0.01	6.122	0.15	0.3455	0.007	0.7678	0.1337	0.002	1988	21	1915	31	2142	25
42	2002	9	405	Metamict core	Oscillatory-patchy	0.00	1.223	0.13	0.0813	0.007	0.8563	0.1075	0.002	810.6	36	503.9	40	1749	24
43	5281	1	5027	Core	Oscillatory-patchy	0.00	6.978	0.14	0.3902	0.006	0.7536	0.13026	0.001	2106.3	18	2121	27	2099.5	19

1889

1890 Table 2. Isotopic data for in-situ LA-ICP-MS apatite dating of granodioritic gneiss, tonalitic-trondhjemite gneiss and apatite-zircon pegmatite

N°	U (ppm)	Th (ppm)	Pb (ppm)	Position	Texture	Equivalent diameter	238U/206Pb	2σ	207Pb/206Pb	2σ
BMN20B – Granodioritic gneiss										
1	37.0	3.1	4.3	Core	Oscillatory	200	2.51	1.4	0.1728	1.2
2	79.7	4.8	4.5	Core	Oscillatory	200	2.65	2.0	0.1502	0.9
3	44.8	1.4	3.4	Core	Oscillatory	200	2.63	2.4	0.1631	1.3
4	28.4	0.8	3.8	Core	Homogeneous	200	2.50	2.1	0.1893	1.2
5	33.9	0.6	3.3	Core	Homogeneous	200	2.52	2.1	0.1728	1.3
6	16.1	0.1	3.2	Core	Homogeneous	100	2.40	2.2	0.2199	1.5

83

7	19.7	0.6	3.6	Transition core-rim	Oscillatory	150	2.39	2.1	0.2102	1.3
8	28.0	3.1	4.4	Core	Homogeneous	200	2.44	2.0	0.1900	0.7
9	49.8	9.5	5.7	Core	Oscillatory	250	2.51	2.0	0.1643	1.1
10	43.8	7.6	5.1	Core	Oscillatory	100	2.50	1.7	0.1631	1.5
11	11.5	0.4	1.3	Core	Homogeneous	100	2.53	1.5	0.1845	2.2
12	6.6	0.2	3.3	Core	Homogeneous	150	2.03	1.6	0.3185	1.3
13	19.3	0.4	3.7	Core	Homogeneous	200	2.44	1.5	0.2142	1.2
14	29.2	4.5	4.5	Core	Homogeneous	200	2.46	1.7	0.1850	1.4

BMN11 – Tonalitic-trondhjemitic gneiss

1	2.2	1.2	4.3	Core	Homogeneous	200	1.30	5.1	0.5500	4.9
2	21.9	5.4	3.0	Zone 1	Homogeneous	800	2.53	2.1	0.1664	1.3
3	11.5	2.9	2.2	Core	Homogeneous	250	2.36	2.0	0.1854	1.1
4	19.8	3.4	2.2	Rim	Homogeneous	200	2.48	2.0	0.1606	0.9
5	20.5	2.5	1.9	Core	Oscillatory	200	2.47	2.0	0.1587	1.1
6	32.9	4.2	2.6	Zone 1	Homogeneous	200	2.53	2.0	0.1539	0.9
7	6.2	0.6	1.7	Core	Homogeneous	200	2.24	2.1	0.2378	1.4
8	25.6	4.3	2.3	Zone 1	Homogeneous	400	2.55	2.0	0.1522	1.1
9	8.5	1.2	1.6	Core	Homogeneous	400	2.41	2.1	0.1881	1.8
10	34.0	5.2	3.1	Zone 1	Homogeneous	100	2.54	2.0	0.1546	0.9
11	6.3	0.7	1.9	Zone 1	Homogeneous	100	2.27	2.2	0.2509	2.0
12	28.8	3.3	2.6	Transition core-zone 1	Oscillatory	100	2.61	2.0	0.1588	1.2
13	9.2	0.5	1.5	Zone 1	Homogeneous	100	2.46	8.1	0.1954	2.1
14	21.7	6.3	3.2	Core	Homogeneous	800	2.46	9.1	0.1668	2.8
15	8.5	1.4	2.3	Core	Complexe	800	2.33	8.2	0.2323	2.6

16	31.8	6.7	5.2	Transition core-zone 1	Complexe	800	2.52	8.1	0.1624	1.3
17	7.2	1.2	2.2	Zone 1	Complexe	200	2.24	8.5	0.2418	2.4
18	13.4	1.6	2.5	Transition core-zone 1	Complexe	200	2.39	8.1	0.2078	2.7
19	34.6	6.0	3.6	Zone 1	Homogeneous	200	2.55	8.1	0.1584	1.1
20	36.1	4.8	2.9	Zone 1	Homogeneous	300	2.55	8.2	0.1504	1.1
21	5.1	0.4	2.7	Transition core-zone 1	Complexe	200	2.05	8.2	0.3257	2.1
22	34.0	4.8	3.1	Core	Complexe	200	2.56	8.2	0.1575	1.0
23	10.1	0.8	2.0	Zone 1	Homogeneous	200	2.34	8.2	0.2099	2.3
24	31.5	3.8	2.9	Transition zones 1-2	Homogeneous	200	2.55	8.1	0.1612	1.2
25	33.6	5.0	3.2	Zone 2	Homogeneous	200	2.56	8.2	0.1585	1.2
26	16.3	2.5	2.5	Transition core-zone 1	Oscillatory	200	2.46	8.1	0.1858	1.3

BMN20 – Titanite-allanite type pegmatite

1	54.3	5.1	3.7	Core	Homogeneous	600	2.60	1.4	0.1516	0.9
2	85.3	13.7	5.8	Core	Homogeneous	600	2.66	1.6	0.1431	1.0
3	55.7	3.6	3.2	Core	Mottled	500	2.61	2.1	0.1499	1.3
4	14.8	3.1	3.3	Core	Homogeneous	600	2.45	1.8	0.2118	1.3
5	24.1	3.6	3.6	Core	Homogeneous	600	2.50	1.6	0.1849	1.3
6	33.4	2.1	3.1	Core	Homogeneous	600	2.62	1.5	0.1659	1.0
7	55.8	3.2	3.1	Core	Homogeneous	600	2.70	2.5	0.1477	0.9
8	39.0	2.7	3.1	Core	Homogeneous	600	2.60	1.5	0.1603	1.2
9	34.3	2.4	3.0	Core	Homogeneous	600	2.53	1.8	0.1641	1.3
10	41.2	4.0	5.7	Core	Homogeneous	500	2.45	1.5	0.1807	1.0
11	58.1	4.6	5.4	Core	Homogeneous	500	2.56	1.6	0.1635	0.9

12	18.8	7.9	7.5	Core	Homogeneous	1500	2.22	8.2	0.2604	1.1
13	19.1	9.0	7.3	Core	Homogeneous	1500	2.27	8.2	0.2552	1.2
14	17.6	7.6	7.1	Core	Homogeneous	1500	2.20	8.4	0.2557	1.3
15	15.7	6.7	6.3	Core	Homogeneous	1500	2.02	9.1	0.2472	1.6
16	24.7	6.1	7.6	Transition core-zone 1	Oscillatory	1500	2.25	8.3	0.2276	1.4
17	82.0	7.4	7.8	Rim	Oscillatory	1500	2.46	8.1	0.1592	0.9
18	75.4	6.1	6.7	Rim	Oscillatory	1500	2.55	8.2	0.1599	1.0
19	63.2	5.2	6.5	Rim	Oscillatory	1500	2.46	8.1	0.1639	0.9
20	67.4	5.5	6.9	Rim	Oscillatory	1500	2.47	8.1	0.1639	1.2
21	70.0	5.6	5.7	Rim	Oscillatory	1500	2.59	8.0	0.1583	0.9
22	106.3	10.6	5.3	Core	Homogeneous	1000	2.65	8.2	0.1463	2.7
23	80.8	8.9	4.5	Core	Mottled	1000	2.67	9.3	0.1426	1.9
24	9.9	1.3	2.7	Core	Homogeneous	1000	2.22	8.2	0.2303	2.2
25	5.8	0.1	2.9	Core	Homogeneous	600	2.06	8.3	0.3131	1.6
26	3.0	0.1	2.3	Core	Homogeneous	1000	1.79	1.8	0.3882	1.9
27	5.3	0.1	3.3	Core	Mottled	1000	1.92	2.3	0.351	3.1
28	5.0	0.1	2.9	Core	Mottled	1000	1.92	1.7	0.3287	1.9
29	4.1	0.1	2.9	Core	Mottled	1000	1.86	1.8	0.3734	1.8
30	15.7	1.7	4.5	Core	Homogeneous	1000	2.23	1.5	0.2371	1.2
31	31.7	3.1	5.6	Core	Homogeneous	1000	2.36	1.5	0.1973	1.1
32	41.4	3.7	5.8	Core	Homogeneous	1000	2.45	1.5	0.1834	1.0
33	16.7	1.5	3.1	Core	Homogeneous	1000	2.34	1.5	0.2015	1.5
34	48.0	3.9	3.2	Core	Homogeneous	500	2.42	2.3	0.1532	2.1
35	79.0	9.8	7.2	Core	Homogeneous	600	2.59	1.3	0.1587	0.9
36	12.6	1.8	3.6	Rim	Homogeneous	350	2.23	1.9	0.2335	1.9

37	13.3	1.9	4.0	Core	Homogeneous	350	2.28	1.6	0.2441	2.1
38	18.0	2.4	3.6	Rim	Homogeneous	350	2.37	1.4	0.2026	1.5
39	6.5	0.5	4.4	Core	Homogeneous	600	1.78	2.7	0.3354	3.3
40	11.1	1.0	2.9	Core	Mottled	600	2.28	1.7	0.2305	2.0
41	89.9	8.1	7.0	Core	Homogeneous	600	2.55	1.3	0.1558	0.9
42	56.7	4.9	6.3	Core	Homogeneous	600	2.50	1.3	0.1708	0.9
43	58.9	5.4	6.4	Core	Homogeneous	600	2.48	1.3	0.1682	1.1
44	70.3	5.9	6.6	Rim	Oscillatory	1500	2.50	1.4	0.1637	1.1

1891

1892 Table 3. EMPA composition of amphibole in granodioritic gneiss. hornblende-biotite granodiorite with mica-rich enclaves. and hornblende tonalite veins;
 1893 Calculated pressures of crystallization are given in the last rows with a reference to the corresponding calculation method.

Lithology	Granodioritic gneiss						Hornblende-biotite granodiorite with mica-rich enclaves						Hornblende tonalite						
Sample	BMN24						BMS46						BMN164H						
SiO ₂	41.90	41.99	40.90	42.54	41.95	41.63	41.79	41.38	41.88	41.20	41.51	41.03	41.49	42.09	41.70	41.98	42.15	41.48	
TiO ₂	0.66	0.55	0.68	0.72	0.72	0.68	0.48	0.48	0.61	0.68	0.50	0.65	0.51	0.51	0.54	1.28	1.25	1.31	1.28
Al ₂ O ₃	10.70	10.72	10.93	10.75	10.94	11.16	10.96	10.77	10.71	10.77	11.54	11.18	10.93	11.02	10.51	10.37	10.43	10.92	
FeO	19.79	19.90	20.26	19.16	19.73	19.54	19.35	19.13	19.54	19.14	19.54	19.64	19.33	19.32	18.57	18.56	18.82	19.10	
MnO	0.54	0.44	0.45	0.51	0.54	0.48	0.56	0.53	0.50	0.49	0.44	0.52	0.46	0.52	0.52	0.45	0.47	0.44	
MgO	8.55	9.02	8.47	8.73	8.89	8.46	9.29	9.09	9.01	8.74	8.96	8.93	8.92	8.82	9.32	9.19	9.23	8.79	
CaO	11.36	11.46	11.68	11.63	11.49	11.27	11.60	11.52	11.56	11.85	11.42	11.38	11.54	11.37	11.33	11.46	11.31	11.14	
Na ₂ O	1.38	1.41	1.26	1.09	1.47	1.46	1.81	1.38	1.52	1.36	1.52	1.73	1.49	1.47	1.59	1.56	1.53	1.53	
K ₂ O	1.25	1.38	1.36	1.16	1.34	1.39	1.37	1.38	1.29	1.32	1.38	1.48	1.38	1.37	1.20	1.17	1.20	1.28	
F	bdl	bdl	bdl	bdl	bdl	bdl	bdl	bdl	bdl	bdl	bdl	bdl	bdl	bdl	bdl	bdl	bdl	0.55	
Total	96.4	96.89	96.37	96.33	97.5	96.43	97.22	95.99	96.77	95.85	97.15	96.97	96.43	96.93	96.25	96.06	96.56	96.51	
Si	6.427	6.386	6.311	6.49	6.373	6.393	6.351	6.38	6.395	6.388	6.308	6.285	6.375	6.421	6.385	6.441	6.423	6.363	
Al IV	1.573	1.614	1.689	1.51	1.627	1.607	1.649	1.62	1.605	1.612	1.692	1.715	1.625	1.579	1.615	1.559	1.577	1.637	

87

Sum T	8	8	8	8	8	8	8	8	8	8	8	8	8	8	8	8	8	8	8
Al VI	0.362	0.308	0.299	0.423	0.332	0.414	0.313	0.336	0.323	0.355	0.374	0.304	0.354	0.402	0.282	0.316	0.296	0.339	
Ti	0.076	0.062	0.079	0.083	0.082	0.078	0.055	0.056	0.07	0.079	0.057	0.075	0.059	0.062	0.148	0.144	0.15	0.148	
Fe3	0.67	0.759	0.728	0.571	0.693	0.62	0.646	0.65	0.652	0.492	0.769	0.718	0.637	0.633	0.607	0.489	0.595	0.628	
Mg	1.954	2.046	1.948	1.984	2.012	1.936	2.105	2.088	2.05	2.02	2.029	2.039	2.043	2.006	2.127	2.102	2.097	2.01	
Fe2	1.868	1.772	1.887	1.874	1.813	1.89	1.812	1.817	1.844	1.989	1.714	1.799	1.847	1.832	1.771	1.892	1.803	1.822	
Mn	0.07	0.053	0.059	0.065	0.067	0.062	0.069	0.053	0.061	0.064	0.056	0.066	0.06	0.065	0.065	0.056	0.058	0.054	
Sum C	5	5	5	5	5	5	5	5	5	5	5	5	5	5	5	5	5	5	5
Mn	0	0.003	0	0.001	0.003	0	0.003	0.016	0.003	0	0.001	0.002	0	0.001	0.002	0.003	0.003	0.003	
Fe2	0	0	0	0	0	0	0	0	0	0	0	0	0	0	0	0	0	0	
Ca	1.867	1.867	1.93	1.901	1.87	1.855	1.889	1.903	1.891	1.968	1.858	1.867	1.9	1.858	1.859	1.884	1.847	1.832	
Na	0.133	0.13	0.07	0.098	0.127	0.145	0.109	0.081	0.106	0.032	0.141	0.13	0.1	0.141	0.139	0.113	0.151	0.165	
Sum B	2	2	2	2	2	2	2	2	2	2	2	2	2	2	2	2	2	2	
Ca	0	0	0	0	0	0	0	0	0	0	0	0	0	0	0	0	0	0	
Na	0.278	0.285	0.306	0.223	0.306	0.289	0.423	0.333	0.344	0.378	0.308	0.384	0.345	0.294	0.334	0.35	0.302	0.29	
K	0.245	0.267	0.268	0.225	0.259	0.273	0.266	0.271	0.251	0.261	0.268	0.289	0.271	0.267	0.234	0.229	0.234	0.25	
Sum A	0.523	0.552	0.574	0.448	0.565	0.561	0.689	0.604	0.596	0.639	0.576	0.673	0.615	0.561	0.569	0.579	0.536	0.54	
F																		0.27	
Hollister et al.. (1987) +-1 kbar	6.3	6.3	6.6	6.3	6.5	6.8	6.5	6.4	6.3	6.5	7.1	6.8	6.6	6.6	6.1	5.9	5.9	6.4	
Johnson and Rutherford (1989) +-0.5 kbar	4.8	4.8	5.1	4.8	5	5.2	5	4.9	4.8	5	5.4	5.2	5	5	4.7	4.6	4.6	4.9	
Schmidt (1992) +-0.6 kbar	6.3	6.3	6.6	6.3	6.5	6.7	6.5	6.4	6.3	6.5	7	6.8	6.5	6.5	6.1	6	6	6.4	
Thomas and Ernst (1990) +-1 kbar	4.3	4.2	4.6	4.2	4.4	4.7	4.4	4.4	4.2	4.4	5	4.7	4.5	4.5	4	3.9	3.9	4.3	
Mutch et al.. (2016) +- 0.6 kbar	5	4.9	5.2	5	5.1	5.4	5.1	5.1	5	5.1	5.6	5.4	5.2	5.2	4.8	4.7	4.7	5.1	

1894

1895

Table 4. Major and trace elements composition of amphibolites, micaschist, paragneiss, gneisses, plutonic rocks and pegmatites.

	Amphibolite	Amphibolite	Micaschist	Paragneiss	Granodioritic gneiss		Microgranular enclave in granodioritic gneiss	Monzogabbro	Hornblende-biotite granodiorite	GG-granitoid	GG-granitoid		
Sample	BMN109	BMN150	1684-sd	BMS114B	BMN7	BMN24	BB15	BMN94	BMN47bis	BMS134C	BMS23	BB7	BMN1
SiO ₂	54.05	52.3	61.68	61.66	66.72	69.71	62.65	69.2	51.86	65.67	68.13	71.89	67.16
Al ₂ O ₃	11.89	16.87	14.39	17.95	15.14	15.14	14.68	15.81	17.38	15.73	15.11	14.59	14.89
Fe ₂ O ₃	11.11	9.15	8.11	7.85	4.55	3.08	5.39	3.08	10.13	4.47	3.5	2.12	4.22
CaO	10.15	9.63	6.92	1.24	3.86	2.98	4.44	3.1	5.45	3.72	2.97	2.31	3.21
MgO	7.31	5.6	2.41	2.84	2.01	1.21	2.97	0.92	4.93	1.75	1.35	0.76	1.41
Na ₂ O	2.18	3.83	2.99	2.08	3.99	4.2	3.85	4.51	4.3	4.27	4.28	4.23	3.66
K ₂ O	0.49	0.38	0.25	2.94	3.17	2.98	3.33	2.74	2.28	2.81	2.79	3.17	3.56
TiO ₂	1.04	0.87	0.83	0.73	0.43	0.38	0.54	0.32	0.97	0.49	0.37	0.21	0.6
MnO	0.11	0.15	0.19	0.09	0.07	0.05	0.08	0.04	0.13	0.07	0.06	0.04	0.06
P ₂ O ₅	0.23	0.2	0.42	bdl	0.17	0.14	0.24	0.17	0.45	0.22	0.16	0.08	0.24
LOI	0.47	1.37	0.87	1.87	0.76	0.65	1.4	0.57	1.48	0.68	0.85	0.53	0.82
Total	99.19	100.33	99.06	99.25	100.86	100.5	99.57	100.45	99.36	99.87	99.56	99.93	99.82
100 *Mg#	56.58	54.78	37.09	41.75	46.71	43.67	52.19	37.28	49.1	43.76	43.31	41.49	39.84
Be	0.93	1.21	1	1.19	1.42	1.29	1.69	1.45	1.60	1.53	1.58	1.46	1.43
Sc	34.44	25.01	12.17	21.47	9.56	5.52	13.52	2.07	27.68	10.73	8.62	3.86	10.18
V	207	161	54	139	80	46	99	46	182.89	73	59	28	58
Cr	1129	87	26	217	227	134	156	51	86.73	32	106	183	177
Co	43.91	27.09	22.4	25.53	10.92	6.48	16.63	5.11	28	10.26	7.37	3.89	7.62
Ni	313.65	24.11	9.45	71.19	15.8	9.26	25.03	13.44	29	8.35	9.41	7.84	9.12
Cu	56.6	11.69	bdl	2.65	14.21	6.96	40.53	15.27	8.02	53.13	20.1	2.56	2.37
Zn	86	90	128	110	58	52	68	48	128	74	58	39	64
Ga	na	18.99	18.01	23.60	18.06	17.66	18.84	17.32	22.83	20.04	18.55	16.88	18.67
Ge	na	1.24	1.41	1.98	1.19	1.2	1.31	0.95	1.62	1.38	1.22	1.03	1.23
Cs	0.16	0.12	0.21	5.4	2.54	2.49	1.71	2.18	3.82	1.9	2.06	1.76	1.76
Rb	2.92	2.40	2.99	114.17	98.15	73.31	90.57	55.91	100.11	84.44	87.05	91.12	108.32
Sr	412	276	510	199	598	606	610	689	788	769	655	473	499
Ba	213	132	79	608	711	854	791	1018	618.94	753	606	653	1071
Y	17.30	26.97	31.58	21.40	10.54	10.36	16.70	5.68	25.15	16.22	15.16	8.39	19.31

Zr	119	151	182	139	117	107	191	111	162	164	111	103	233
Hf	2.9	3.69	4.33	3.87	3.3	3.11	5.02	3.08	4.06	4.47	3.21	2.99	5.84
Nb	9.74	8.38	7.43	6.42	5.05	5.1	5.77	3.36	6.00	5.47	4.65	4.34	9.99
Ta	0.56	0.63	0.68	0.57	0.65	0.66	0.45	0.33	0.39	0.51	0.52	0.32	1.27
Mo	9.08	1.6	1.59	3.95	10.88	7.01	5.41	3.41	0.57	1.22	5.11	9.9	9.41
Cd	na	0.17	0.16	0.05	0.07	0.05	0.07	0.04	0.1	0.07	0.06	0.04	0.07
In	na	0.05	0.05	0.06	bdl	bdl	0.03	bdl	0.07	0.04	bdl	bdl	bdl
Sn	2.99	1.72	1.83	1.44	1.07	1	1.17	0.84	1.76	1.08	1.18	0.95	1.54
Sb	na	0.13	bdl	bdl	0.09	bdl							
W	na	1.22	0.98	4.08	8.27	5.35	3.92	1.19	bdl	bdl	3.85	7.55	7.13
Pb	3.5	4.6	6.4	7.5	11	10.3	11.4	11	5.2	10.2	10.4	10.8	11.8
Bi	na	0.29	0.13	0.07	0.11	0.15	0.08	0.12	0.07	0.08	0.14	bdl	0.06
Th	1.86	2.82	2.06	3.62	8.78	3.77	5.49	3	3.12	3.19	4.59	3.5	6.75
U	0.47	0.74	0.61	1.31	1.76	0.79	0.65	0.95	0.52	0.93	1.24	0.63	1.94
K/Rb	1393	1312	696	213	268	338	306	407	1.62	276	266	289	273
Ca/Cs	459131	561164	237708	1641	10835	8531	18566	10143	0.1	14031	10313	9415	13052
Nb/Ta	17.3	13.2	10.9	11.35	7.79	7.72	12.8	10.09	12.94	10.83	8.89	13.53	7.84
Zr/Hf	40.97	40.91	41.95	35.77	35.42	34.38	38.06	35.98	0.79	36.79	34.66	34.43	39.95
La	20.6	14.5	20.6	20.8	37.1	21.6	34.2	20.5	26.1	27.3	25.4	18.5	41.2
Ce	44.2	32.8	45.3	43.3	77.1	49.7	60	39.9	67.6	49.7	45.8	47.5	89.7
Pr	5.6	4.74	6.1	5.58	8.13	5.81	8.45	4.71	7.36	7.93	6.15	4.13	10.35
Nd	23	19.8	24.2	22.4	28.4	22.5	33.4	17.4	30.3	32.4	24.2	14.3	38.9
Sm	4.38	4.76	5.36	4.54	4.42	4.11	6.38	2.68	6.68	6.14	4.58	2.5	6.97
Eu	1.22	1.35	1.54	1.11	1.1	1.05	1.47	0.89	1.81	1.51	1.1	0.68	1.56
Gd	3.87	4.42	5.08	3.92	2.99	2.84	4.73	1.71	5.54	4.39	3.48	1.8	4.96
Tb	0.55	0.7	0.82	0.6	0.37	0.36	0.59	0.19	0.85	0.56	0.45	0.24	0.66
Dy	3.27	4.54	5.23	3.82	1.99	1.93	3.16	1.03	4.92	3.12	2.43	1.35	3.64
Ho	0.65	0.97	1.13	0.82	0.37	0.35	0.59	0.2	0.94	0.59	0.48	0.26	0.7
Er	1.85	2.7	3.09	2.23	1.02	0.95	1.5	0.53	2.33	1.57	1.24	0.7	1.82
Tm	0.24	0.41	0.47	0.34	0.15	0.14	0.22	0.08	0.33	0.23	0.17	0.11	0.27
Yb	1.72	2.73	3.07	2.15	1.02	0.93	1.35	0.55	2.02	1.47	1.07	0.69	1.74
Lu	0.24	0.42	0.47	0.33	0.16	0.14	0.21	0.09	0.28	0.22	0.16	0.11	0.26
SumREE	111.3	94.8	122.5	111.9	164.3	112.4	156.2	90.5	157.1	137.1	116.7	92.9	202.8
LaN/YbN*	8.1	3.6	4.6	6.6	24.7	15.8	17.2	25.5	8.8	12.6	16.2	18.3	16.1
La/Yb	12	5	7	10	36	23	25	38	13	19	24	27	24
Sr/Y	24	10	16	9	57	59	37	121	1.1	47	43	56	26
Ce/Sr	0.11	0.12	0.09	0.22	0.13	0.08	0.10	0.06	0.09	0.06	0.07	0.10	0.18

Na-rich series		Pegmatites								
		Tonalitic-trondhjemite gneiss		Trondhjemite	Two-mica granite	Titanite-allanite-bearing pegmatite	Apatite-zircon-bearing pegmatite	Garnet-columbite-bearing pegmatite	Garnet-REE-bearing pegmatite	
Sample		BMS34C	BMN42	BMN11	BMN33	BMS9	BMN28	BMN82B	BMN86	BB15P
SiO ₂		69.56	68.39	71.05	59.23	72.36	71.81	59.57	73.46	76.46
Al ₂ O ₃		15.54	15.27	16.02	20.63	15.41	14.42	20.37	15.05	14.02
Fe ₂ O ₃		2.52	3.6	1.53	3.87	1.33	4.03	2.725	0.21	0.59
CaO		3	3.85	3.09	4.59	2.21	2.73	5.124	0.47	1.58
MgO		0.89	1.56	0.49	1.72	0.33	0.00	1.01	0.00	0.00
Na ₂ O		5.67	4.96	5.85	7.12	5.46	5.17	6.32	4.69	6.35
K ₂ O		1.13	1.17	0.81	1.39	1.61	0.63	2.35	5.46	0.52
TiO ₂		0.3	0.43	0.16	0.34	0.14	0.063	0.248	bdl	0.025
MnO		0.04	0.05	0.02	0.09	0.02	0.020	0.0546	0.020	0.021
P ₂ O ₅		0.09	0.14	bdl	0.17	bdl	bdl	1.06	0.12	bdl
LOI		0.68	0.56	0.89	0.44	0.35	0.48	0.74	0.55	0.28
Total		99.41	99.95	99.89	99.59	99.22	99.35	99.58	100.02	99.84
100 *Mg#		41.09	46.16	38.7	46.82	32.75				
Be		1.05	0.87	0.97	3.54	1.5	1.28	3.27	1.11	2.56
Sc		6.93	7.16	2.44	24.16	2.04	0.78	6.39	0.96	1.53
V		32	56	18	48	11	62	36	1	3
Cr		40	86	76	47	74	83	43	61	96
Co		5.41	9.84	3.44	9.02	1.54	2.61	5.63	0.17	0.27
Ni		7.98	39.53	5.38	30	2.09	3.09	11.97	bdl	bdl
Cu		61.31	24.11	53.32	5.69	3.34	62.02	5.50	bdl	bdl
Zn		61	57	33	54	39	46	46	33	12
Ga		21.88	19.08	19.83	na	18.03	17.91	27.48	25.60	23.61
Ge		0.72	0.84	0.69	na	0.77	0.67	1.45	1.57	1.38
Cs		0.81	1.27	0.48	1.75	1.55	0.28	4.78	3.71	0.96
Rb		35.47	34.79	16.91	35.70	42.48	5.26	82.61	251.39	19.94
Sr		609	429	424	483	770	391	587	63	35
Ba		158	205	177	151	598	120	336	130	19
Y		8.64	7.75	1.97	10.18	3.75	1.14	48.59	1.92	10.35
Zr		107	105	78	92	83	43	56	15	26
Hf		2.88	2.75	2.1	2.51	2.4	1.26	2.08	0.91	1.01

Nb		2.05	2.55	1.13	3.1	2.07	0.48	9.36	2.87	2.54
Ta		0.26	0.26	0.11	0.3	0.18	0.15	2.01	0.50	0.44
Mo		1.79	4.52	4.23	1.39	4.3	4.77	1.58	3.63	5.79
Cd		0.04	0.06	0.04	na	0.03	0.04	0.07	0.03	0.03
In	bdl		bdl	bdl	na	bdl	bdl	bld	bdl	bdl
Sn		0.73	0.77	bdl	1.87	0.47	bdl	1.52	0.53	0.40
Sb	bdl		bdl	bdl	na	bdl	bdl	0.06	bdl	bdl
W		1.31	1.64	3.24	na	3.48	3.63	1.02	2.93	4.43
Pb		5.2	4.2	4.6	7.1	8.1	5.7	21.0	25.5	27.5
Bi	bdl		0.05	0.09	na	bdl	0.29	0.07	0.05	0.08
Th		1.93	1.6	1.39	4.56	1.33	0.82	6.95	2.21	6.74
U		0.69	0.36	0.21	0.7	0.51	0.87	1.56	0.96	5.22
K/Rb		265	279	398	323	314	989	236	180	217
Ca/Cs	26437	21579	46094	18799	10173	68843	7654	899	11810	
Nb/Ta		8.02	9.72	10.46	10.49	11.74	3.19	4.67	5.69	5.78
Zr/Hf		37.15	38.17	37.12	36.83	34.63	33.63	26.89	16.48	25.91
La		23.4	16.4	8.6	22.1	9.9	3.06	6.34	1.89	1.17
Ce		24.9	23.2	15.3	47.9	19.6	6.96	20.24	3.79	2.90
Pr		5.65	3.86	1.77	5.25	2.49	0.71	2.93	0.58	0.29
Nd		21.2	15.4	6.7	18.1	9.6	2.77	15.74	2.19	1.19
Sm		3.88	2.89	1.13	2.9	1.7	0.50	6.98	1.03	0.50
Eu		1.15	0.86	0.45	0.7	0.49	0.35	1.40	0.09	0.26
Gd		2.89	2.3	0.79	2.41	1.11	0.37	9.04	0.73	0.80
Tb		0.34	0.3	0.09	0.34	0.14	0.05	1.53	0.11	0.20
Dy		1.6	1.51	0.46	1.93	0.72	0.25	9.01	0.44	1.56
Ho		0.28	0.27	0.07	0.38	0.13	0.04	1.72	0.06	0.38
Er		0.66	0.65	0.17	0.95	0.33	0.12	4.17	0.12	1.20
Tm		0.09	0.09	0.02	0.13	0.05	0.02	0.54	0.02	0.20
Yb		0.56	0.56	0.15	0.96	0.31	0.15	3.09	0.13	1.34
Lu		0.08	0.08	0.02	0.12	0.05	0.02	0.42	0.02	0.21
SumREE		86.7	68.4	35.8	104.1	46.7	15.4	83.2	11.2	12.2
LaN/YbN*		28.7	19.9	38.8	15.7	21.4	192.2	1.4	134.9	9.2
La/Yb		42	29	57	23	31	21	2	14	1
Sr/Y		70	55	215	47	205	343	12	33	3
Ce/Sr		0.04	0.05	0.04	0.10	0.03	0.02	0.03	0.06	0.08

1897 na. not analyzed. bdl. below the detection limit. * : data normalized to chondrite. (McDonough and Sun. 1995).

1898 **Appendix**1899 *Appendix 1. Operating conditions for the LA-ICP-MS equipment for U-Pb dating on apatite*

Laboratory & Sample Preparation	
Laboratory name	GeOHeLiS Analytical Platform. OSUR. Univ Rennes 1. France
Sample type/mineral	Apatite
Sample preparation	Thin-section
Imaging	Jeol JSM 6360LV. Géoscience Environnement Toulouse. Univ Toulouse 3 Paul Sabatier. France ; TESCAN Vega 3. GeoRessources. Univ de Lorraine. Nancy. France
Laser ablation system	
Make. Model & type	ESI NWR193UC. Excimer
Ablation cell	ESI NWR TwoVol2
Laser wavelength	193 nm
Pulse width	< 5 ns
Fluence	6 J/cm ²
Repetition rate	5Hz
Spot size	40 - 50 µm
Sampling mode / pattern	Single spot
Carrier gas	100% He. Ar make-up gas and N2 (3 ml/mn) combined using in-house smoothing device
Background collection	20 seconds
Ablation duration	60 seconds
Wash-out delay	15 seconds
Cell carrier gas flow (He)	0.75 l/min
ICP-MS Instrument	
Make. Model & type	Agilent 7700x. Q-ICP-MS
Sample introduction	Via conventional tubing
RF power	1350W
Sampler. skimmer cones	Ni
Extraction lenses	X type
Make-up gas flow (Ar)	0.85 l/min
Detection system	Single collector secondary electron multiplier
Data acquisition protocol	Time-resolved analysis
Scanning mode	Peak hopping, one point per peak
Detector mode	Pulse counting. dead time correction applied. and analog mode when signal intensity > ~ 10 ⁶ cps
Masses measured	²⁰⁴ (Hg + Pb). ²⁰⁶ Pb. ²⁰⁷ Pb. ²⁰⁸ Pb. ²³² Th. ²³⁸ U + ⁴³ Ca (Ap)
Integration time per peak	10-30 ms
Sensitivity / Efficiency	23000 cps/ppm Pb (50µm. 10Hz)
Data Processing	
Gas blank	20 seconds on-peak
Calibration strategy	Madagascar apatite standard used as primary reference material. McClure and Durango standards used as secondary reference material (quality control)
Common-Pb correction. composition and uncertainty	No common-Pb correction.
Reference Material info	Madagascar (Cochrane et al. 2014) McClure (Schoene and Bowring 2006) Durango (McDowell et al. 2005)
Data processing package	Iolite (Paton et al.. 2010). VizualAge_UcomPbine (Chew et al.. 2014)

used	More information on the procedure in Pochon et al.. 2016
Quality control / Validation	McClure: Jan2019 - 516 ± 7.5 Ma (n=18. MSWD=8.2) Sept2019 – 529 ± 5.5 Ma (n=12. MSWD=1.4) Durango: Jan2019 - 31.75 ± 0.45 Ma (n=23. MSWD=2.7) Sep2019 – 33 ± 2 Ma (n=12. MSWD=1.9)

1900

1901 References :

1902 Chew DM. Petrus JA. Kamber BS (2014) U–Pb LA–ICPMS dating using accessory mineral standards with variable common Pb. Chemical
1903 Geology 363:185-199 doi:<https://doi.org/10.1016/j.chemgeo.2013.11.006>1904 Cochrane R. Spijkings RA. Chew D. Wotzlaw J-F. Chiaradia M. Tyrrell S. Schaltegger U. Van der Lelij R (2014) High temperature (>350°C)
1905 thermochronology and mechanisms of Pb loss in apatite. *Geochimica et Cosmochimica Acta* 127:39-56
1906 doi:<https://doi.org/10.1016/j.gca.2013.11.028>1907 McDowell FW. McIntosh WC. Farley KA (2005) A precise 40Ar–39Ar reference age for the Durango apatite (U–Th)/He and fission-track
1908 dating standard. *Chemical Geology* 214(3):249-263 doi:<https://doi.org/10.1016/j.chemgeo.2004.10.002>1909 Paton C. Woodhead JD. Hellstrom JC. Hergt JM. Greig A. Maas R (2010) Improved laser ablation U–Pb zircon geochronology through
1910 robust downhole fractionation correction. *Geochemistry. Geophysics. Geosystems* 11(3) doi:10.1029/2009GC0026181911 Pochon A. Poujol M. Gloaguen E. Branquet Y. Cagnard F. Gumiaux C. Gapais D (2016) U–Pb LA–ICP–MS dating of apatite in mafic rocks:
1912 Evidence for a major magmatic event at the Devonian-Carboniferous boundary in the Armorican Massif (France). *American Mineralogist*
1913 101(11):2430-2442 doi:<http://dx.doi.org/10.2138/am-2016-5736>1914 Schoene B. Bowring S (2006) U–Pb systematics of the McClure Mountain syenite: thermochronological constraints on the age of the
1915 40Ar/39Ar standard MMhb. *Contributions to Mineralogy and Petrology* 151(5):615

1916

1917 *Appendix 2 Operating conditions for the LA-ICP-MS equipment for U-Pb dating on zircon*

1918

Laboratory & Sample Preparation	
Laboratory name	GeOHeLiS Analytical Platform. OSUR. Univ Rennes 1. France
Sample type/mineral	Zircon
Sample preparation	Thin-section
Imaging	Jeol JSM 6360LV. Géoscience Environnement Toulouse. Univ Toulouse 3 Paul Sabatier. France ; TESCAN Vega 3. GeoRessources. Univ de Lorraine. Nancy. France
Laser ablation system	
Make. Model & type	ESI NWR193UC. Excimer
Ablation cell	ESI NWR TwoVol2
Laser wavelength	193 nm
Pulse width	< 5 ns
Fluence	8 J/cm ²

Repetition rate	3Hz
Spot size	30 μm
Sampling mode / pattern	Single spot
Carrier gas	100% He. Ar make-up gas and N2 (3 ml/mn) combined using in-house smoothing device
Background collection	20 seconds
Ablation duration	60 seconds
Wash-out delay	15 seconds
Cell carrier gas flow (He)	0.80 l/min
ICP-MS Instrument	
Make. Model & type	Agilent 7700x. Q-ICP-MS
Sample introduction	Via conventional tubing
RF power	1350W
Sampler. skimmer cones	Ni
Extraction lenses	X type
Make-up gas flow (Ar)	0.85 l/min
Detection system	Single collector secondary electron multiplier
Data acquisition protocol	Time-resolved analysis
Scanning mode	Peak hopping. one point per peak
Detector mode	Pulse counting. dead time correction applied. and analog mode when signal intensity $> \sim 10^6$ cps
Masses measured	$^{204}\text{Hg} + \text{Pb}$, ^{206}Pb , ^{207}Pb , ^{208}Pb , ^{232}Th , ^{238}U
Integration time per peak	10-30 ms (^{207}Pb)
Sensitivity / Efficiency	23000 cps/ppm Pb (50 μm , 10Hz)
Data Processing	
Gas blank	20 seconds on-peak
Calibration strategy	GJ1 zircon standard used as primary reference material. Plešovice used as secondary reference material (quality control)
Common-Pb correction. composition and uncertainty	No common-Pb correction.
Reference Material info	GJ1 (Jackson et al.. 2004). Plešovice (Slama et al.. 2008)
Data processing package	Iolite (Paton et al.. 2010)
Uncertainty level and propagation	Ages are quoted at 2 sigma absolute. propagation is by quadratic addition according to Horstwood et al. (2016). Reproducibility and age uncertainty of reference material are propagated.
Quality control / Validation	Plešovice: concordia age = 338.7 ± 3.3 Ma (n=6; MSWD=0.35)

1919

1920 References :

1921 Horstwood MSA. Košler J. Gehrels G. Jackson SE. McLean NM. Paton C. Pearson NJ. Sircombe K. Sylvester P. Vermeesch P. Bowring JF.

1922 Condon DJ. Schoene B (2016) Community-Derived Standards for LA-ICP-MS U-(Th-)Pb Geochronology – Uncertainty Propagation. Age

1923 Interpretation and Data Reporting. Geostandards and Geoanalytical Research 40(3):311-332 doi:10.1111/j.1751-908X.2016.0379.x

1924 Jackson SE. Pearson NJ. Griffin WL. Belousova EA (2004) The application of laser ablation-inductively coupled plasma-mass spectrometry
1925 to in situ U–Pb zircon geochronology. Chemical Geology 211:47-691926 Paton C. Woodhead JD. Hellstrom JC. Hergt JM. Greig A. Maas R (2010) Improved laser ablation U-Pb zircon geochronology through
1927 robust downhole fractionation correction. Geochemistry. Geophysics. Geosystems 11(3) doi:10.1029/2009GC002618

1928 Sláma J. Kosler J. Condon DJ. Crowley JL. Gerdes A. Hanchar JM. Horstwood MSA. Morris GA. Nasdala L. Norberg N. Schaltegger U.
1929 Schoene B. Tubrett MN. Whitehouse MJ (2008) Plesovice zircon -- A new natural reference material for U-Pb and Hf isotopic
1930 microanalysis. *Chemical Geology* 249(1-2):1-35

1931